# APPLICATIONS OF TIME SERIES ANALYSIS

to

# GEOPHYSICAL DATA

by

ALAN DANA CHAVE

B. S., Harvey Mudd College
(1975)

SUBMITTED IN PARTIAL FULFILLMENT
OF THE REQUIREMENTS FOR THE
DEGREE OF

DOCTOR OF PHILOSOPHY

at the

MASSACHUSETTS INSTITUTE OF TECHNOLOGY
and the
WOODS HOLE OCEANOGRAPHIC INSTITUTION

June, 1980

Signature of Author_____

Joint Program in Oceanography, Massachusetts Institute of Technology-Woods Hole Oceanographic Institution, and the Department of Earth and Planetary Sciences, Massachusetts Institute of Technology, May, 1980

Certified by_____

Thesis Co-supervisor

Certified by_____

Thesis Co-supervisor

Accepted by_____

Chairman, Joint Oceanography Committee in the Earth Sciences, Massachusetts Institute of Technology-Woods Hole Oceanographic Institution

TABLE OF CONTENTS

# LIST OF FIGURES

CHAPTER 4

# LIST OF TABLES

# BIOGRAPHICAL SKETCH

I was born in Whittier, California on 12 May 1953. I attended Harvey Mudd College, Claremont, California from 1971 to 1975 and was graduated in June, 1975 with a Bachelor of Science degree in physics, awarded with distinction and departmental honors. My introduction to oceanography came during the summers of 1972-1974, when I worked for the late Dr. Wilton Hardy at the University of Hawaii. In June, 1975, I enrolled in the Woods Hole Oceanographic Institution-Massachusetts Institute of Technology Joint Program in Oceanography. My work has covered portions of the fields of earthquake seismology, magnetotellurics, and paleomagnetism with an emphasis on quantitative analysis of geophysical data. After participating in Leg 74 of the Deep Sea Drilling Project, I will be a postdoctoral investigator in the Geological Research Division of the Scripps Institution of Oceanography.

My publications include:

1. Chave, A.D., R.P. Von Herzen, K.A. Poehls, T.H. Daniel, and C.S. Cox, 1978. Deep ocean magnetotelluric sounding in the northeast Pacific, EOS 59, 269 (abstract).
2. Chave, A.D., 1978.Lithospheric structure of the Walvis Ridge from Rayleigh wave dispersion, EOS 59, 1199 (abstract).
3. Chave, A.D., J.D. Phillips, and D.W. McCowan, 1978. Lithospheric structure of the Walvis Ridge from Rayleigh wave dispersion, Semi-annual Technical Summary, Lincoln Laboratories Report 78-259, pp. 49-50.
4. Chave, A.D. and C.R. Denham, 1979. Climatic change, magnetic intensity variations,and fluctuations of the eccentricity of the earth's orbit during the past 2,000,000 years and a mechanism which may be responsible for the relationship--a discussion, Earth Pl. Sci. Lett. 44, 150-152.
5. Chave, A.D. and R.P. Von Herzen, 1979. Electrical conductivity structure at a deep ocean site northeast of Hawaii, EOS 60, 243 (abstract).
6. Chave, A.D., R.P. Von Herzen, K.A. Poehls, and C.S. Cox, 1979.

Electrical conductivity structure at a deep ocean site northeast of Hawaii, in Proceedings of Workshop on Ocean Floor Electromagnetics, Naval Postgraduate School, Monterey Ca., 20-22 August 1979 (abstract)

7. Chave, A.D., 1979. Lithospheric structure of the Walvis Ridge from Rayleigh wave dispersion, J. geophys. Res. 84, 6840-6848.
8. Chave, A.D., G.P. Lohmann, and C.R. Denham, 1979. Quantitative evaluation of biostratigraphic correlation, EOS 60, 854 (abstract).
9. Denham, C.R. and A.D. Chave, 1979. Late Pleistocene paleosecular variation in marine sediments from the Gardar Drift, NE Atlantic Ocean, EOS 60, 818 (abstract).
10. Chave, A.D., R.P. Von Herzen, K.A. Poehls, and C.S. Cox, 1980. Electromagnetic induction fields in the deep ocean northeast of Hawaii and implications for mantle conductivity, submitted to Geophys. J. Roy. astr. Soc.
11. Chave, A.D. and C.R. Denham, 1980. Geomagnetic secular variation recorded in sediments from the northeast Atlantic Ocean, submitted to J. geophys. Res.

## ACKNOWLEDGEMENTS

The three papers that comprise this thesis represent the products of interaction with many people. I would particularly like to acknowledge the support and encouragement of Dick Von Herzen, whose example as a scientist will always mean a great deal to me. Among the other people at Woods Hole, Chuck Denham and Pat Lohmann provided many useful discussions on data analysis and other topics.

The Walvis Ridge study was originally suggested by Tom Crough while he was a postdoctoral scholar at WHOI. Joe Phillips and Doug McCowan of the Applied Seismology Group at MIT's Lincoln Laboratory gave me access to their computer facilities and programs for surface wave inversion.

The magnetotellurics study is the result of a multi-institutional program with Scripps and the University of Hawaii. Tom Daniel (U. of Hawaii), Jean Filloux (Scripps), and Ken Poehls (UCLA) were present on the instrument deployment cruise. Chip Cox (Scripps) provided the electric field data for this study. Jack Hermance (Brown University) and Jim Larsen (PMEL, Seattle) improved my understanding of induction processes immensely.

The paleomagnetic study is the result of a great deal of work with Chuck Denham and Pat Lohmann. Bill Ruddiman (Lamont) gave me a great deal of useful information on North Atlantic stratigraphy.

Most of the results of this thesis would not be possible without the breakthrough in computing power represented by the VAX line made by the Digital Computer Corporation. Finally, I would like to thank the breweries of the world whose product contributed materially to many discussions.

I was supported for the early parts of this work by a NSF Graduate Fellowship. The Walvis Ridge study was supported by the WHOI Education Office and the Defense Advanced Research Projects Agency. The induction study was funded by the NSF under grants OCE74-12730 and OCE77-8633, and by the WHOI Ocean Industries Program. The paleomagnetic study was supported by NSF contracts OCE77-82255 and OCE79-19258.

# THE APPLICATION OF TIME SERIES ANALYSIS to GEOPHYSICAL DATA

by

Alan Dana Chave

Submitted to the Woods Hole Oceanographic Institution-Massachusetts Institute of Technology Joint Program in Oceanography on May 2, 1980 in partial fulfillment of the requirements for the degree of Doctor of Philosophy.

## ABSTRACT

This thesis consists of three papers applying the techniques of time series analysis to geophysical data. Surface wave dispersion along the Walvis Ridge, South Atlantic Ocean, is obtained by bandpass filtering the recorded seismogram in the frequency domain. The group velocity is anomalously low in the period range of 15-50 s, and formal inversion of the data indicates both crustal thickening to 12.5 km and low shear velocity (4.25-4.35 km/s) to depths of 40-50 km. The electromagnetic induction fields at a deep ocean site northeast of Hawaii were used to determine the electrical conductivity of the earth to 400 km depth. Singular value decomposition of the data matrix indicates three degrees of freedom, suggesting source field complications and a two dimensional conductive structure. Inversion of one of the principal terms in the response function shows an abrupt rise in electrical conductivity to 0.05 mho/m near 160 km with no resolvable decrease below this. A model study suggests that moving source fields influence the induction appreciably in the other principal response function. A set of piston cores from the northeast Atlantic Ocean are used to construct paleomagnetic time series covering the interval 25-127 kybp. Stratigraphic control is provided by counts of planktonic foraminifera, and empirical orthogonal function analysis shows a significant decrease in sedimentation rate at the interglacial/glacial transition. The sediments are magnetically stable and reliable relative paleointensity measurements could be obtained. Spectral analysis of the directions reveals a predominant 10 ky periodicity and no dominant looping direction.

Thesis Co-supervisor: Charles R. Denham
Title: Associate Scientist
Thesis Co-supervisor: Richard P. Von Herzen
Title: Senior Scientist

# CHAPTER ONE

# INTRODUCTION

The quantitative treatment of sequences of data constitutes the field of time series analysis. A single data variable or a field of variables, measured as a function of a well determined dependent quantity like time, is a time series or sequence. The techniques of time series analysis are commonly used in disciplines from economics and engineering to oceanography and geophysics as a means of extracting information from long, complex data sets. Applications include the detection of hidden periodicities, the analysis of variance or power, and the quantitative estimation of statistical correlation.

Time series analysis has been an important tool of the geophysicist since the advent of the physical study of the earth. Early seismologists were limited by the lack of computing machines and developed manual techniques to analyze time series. The first applications to seismograms were limited to the picking of arrival times and amplitudes. The analysis of periodic data, especially earth tides, was also accomplished by hand fitting. Much of this early work is described by Jeffreys (1959) and Bullen (1963).

The introduction of inexpensive and efficient digital computers has resulted in increasingly more elegant and complex analyses of time series. Extensive use is made of the Fourier transform, especially since the rediscovery of the fast Fourier transform algorithm. The equivalence of the time-space and frequency-wavenumber domains is well established. Theoretical expressions in geophysics are often more easily derived in the frequency domain, and it is not uncommon to examine only the frequency domain behavior of a data set. Other geophysical techniques, notably interpolation, least squares fitting, and inverse problems, have been applied to data as computer technology has improved. Bath (1974), Kanasewich (1975), and Claerbout (1976) discuss many uses of these methods,, with an emphasis on seismology. The techniques are also employed in the modelling of marine magnetic anomalies (Schouten and McCamy, 1972) and in the analysis of gravity lines (McKenzie and Bowin, 1976; Detrick, 1978).

Theoretical advances in time series analysis have followed a parallel course to its applications. Much of the early work in the field is based on classical statistics, especially the auto and cross correlation functions. Wiener (1949) defined the power spectrum

as the Fourier transform of the autocorrelation function. Many computational problems exist with this approach due to inherent and incorrect assumptions about long term time series behavior. Additional treatment of the correlation function is necessary to minimise bias and leakage (Blackman and Tukey, 1958; Jenkins and Watts, 1968). The increasing use of the discrete Fourier transform minimized some of these problems and introduced some new ones. The techniques and pitfalls of this approach are discussed in Bendat and Piersol (1966) and Otnes and Enochson (1972). More recently, advances in time series modelling and control systems engineering have led to radically new, nonlinear approaches to spectral analysis. This field is reviewed in Haykin (1979). The choice of spectral technique is data dependent and requires both insight and experimentation by the user. What is appropriate for a short and nonstationary data section is probably not applicable to a long and stationary time series.

This thesis is a collection of three papers applying time series analysis to geophysical data. The emphasis is on applications and no claim for advances in the theory of time series is made. The three studies cover the fields of earthquake seismology, magnetotellurics, and paleomagnetism, and the approaches to time series analysis are nearly as diverse. Other data handling techniques are applied as needed, especially the formalism for geophysical inverse problems (Backus and Gilbert, 1967, 1968, 1970).

In Chapter 2, I have investigated the shear velocity structure of the Walvis Ridge using Rayleigh wave dispersion from natural earthquake sources. The Walvis Ridge is an aseismic feature of large bathymetric relief in the South Atlantic Ocean. Previous work suggests anomalously thick crust for aseismic ridges, but the nature of their deep structure remained largely unknown. Group velocity is easily determined by passing the Fourier transformed seismogram through a bandpass filter and determining the arrival time of the different frequency components. A Gaussian shaped filter was used since it optimizes the trade-off between resolution of arrival time and frequency. The filtering procedure yields a group velocity-period relation, or dispersion curve. A shear velocity-depth relation is

obtained by inverting the dispersion curve. The results show a well-resolved low velocity (4.25-4.35 km/s) region in the top 40-50 km under the ridge. Crustal thickening to 12.5 km is also observed.

In Chapter 3, more sophisticated techniques have been applied to a 36 day long record of the electromagnetic induction fields in the deep ocean. Measurements of the electric and magnetic fields are related by a frequency-wavenumber dependent tensor response function derived from the data. Noise is a serious problem in transfer function analysis, and several methods including a new approach called singular value decomposition, are applied and examined critically. This procedure reveals some possible complications in the source fields which are shown to influence the induction fields. Finally, the electrical conductivity structure to a depth of 400 km is derived by inverting the response functions. A sharp increase in conductivity at 160 km depth is seen, with no resolvable decrease below this.

In Chapter 4, a study of the paleomagnetic field directions and relative paleointensities in a replicate set of piston cores are used to construct a set of time series covering the interval 25-127 kybp. These data are extremely noisy,and the directions are usable only over short (20 ky) sections due to sampling and coring problems. Conventional Fourier techniques were not usable for these short, noisy data sets, and the directional data were mapped onto the complex plane and the power spectrum was computed using the maximum entropy method of Burg (1975). This approach offers the advantage of inherent smoothing and greatly improved resolution. A dominant period for the directional motion near 10 ky was found with no predominance of a single drift direction for the geomagnetic features.

REFERENCES

Backus, G. and F. Gilbert, 1967. Numerical applications of a formalism for geophysical inverse problems, Geophys. J. Roy. astr. Soc. 13, 247-276.

Backus, G. and F. Gilbert, 1968. The resolving power of gross earth data, Geophys. J. Roy. astr. Soc. 16, 169-205.

Backus, G. and F. Gilbert, 1970. Uniqueness in the inversion of inacc inaccurate gross earth data, Phil. Trans. Roy. Soc., Lon. A266, 123-192.

Bath, M., 1974. Spectral Analysis in Geophysics, New York: Elsevier.

Bendat, J.S. and A.G. Piersol, 1966. Measurement and Analysis of Random Data, New York: John Wiley.

Blackman, R.B. and J.W. Tukey, 1959. The Measurement of Power Spectra, New York: Dover, 190 pp.

Bullen, K., 1963. An Introduction to the Theory of Seismology, 3rd ed., Cambridge: Cambridge University Press.

Burg, J.P., 1975. Maximum entropy spectral analysis, Ph.D. thesis, Stanford University, 123 pp.

Claerbout, J.F., 1976. Fundamentals of Geophysical Data Processing, New York: McGraw Hill.

Detrick, R.S., Jr., 1978. The crustal structure and subsidence history of aseismic ridges and mid-plate island chains, Ph.D. thesis, Woods Hole Oceanogr. Inst. and Mass. Inst. of Tech., 182 pp.

Haykin, S. (ed.), 1979. Nonlinear Methods of Spectral Analysis, New York: Springer Verlag.

Jeffreys, Sir H., 1959. The Earth, 4th ed., Cambridge: Cambridge Univ University Press.

Jenkins, G.M. and D.G. Watts, 1968. Spectral Analysis and its Applications, San Francisco: Holden-Day.

Kanasewich, E.R., 1975. Time Sequence Analysis in Geophysics, 2nd ed., Alberta: University of Alberta Press.

McKenzie, D. and C. Bowin, 1976. The relationship between bathymetry and gravity in the Atlantic Ocean, J. geophys. Res. 81, 1903-1915.

Otnes, R.K. and L. Enochson, 1972. Digital Time Series Analysis, New York: John Wiley.

Schouten, H. and K. McCamy, 1972. Filtering marine magnetic anomalies, J. geophys. Res. 77, 7089-7099.

Wiener, N., 1949. Extrapolation, Interpolation, and Smoothing of Stationary Time Series, Cambridge: MIT Press.

# CHAPTER TWO

# LITHOSPHERIC STRUCTURE OF THE WALVIS RIDGE FROM RAYLEIGH WAVE DISPERSION

# LITHOSPHERIC STRUCTURE OF THE WALVIS RIDGE FROM RAYLEIGH WAVE DISPERSION*

Alan D. Chave

Department of Geology and Geophysics
Woods Hole Oceanographic Institution
Woods Hole, MA 02543
and
Department of Earth and Planetary Sciences
Massachusetts Institute of Technology
Cambridge, MA 02139

* published in J. geophys. Res. 84, 6840-6848 (1979)

ABSTRACT

Rayleigh wave group velocity dispersion has been used to study the lithospheric structure along the Walvis Ridge and for a nearby South Atlantic path. Group velocity is anomalously low in the period range of 15-50 s for both surface wave paths. Results of a formal inversion for the ridge suggest crustal thickening to 12.5 km and anomalously low mantle shear velocity of 4.25-4.35 km/s to depths of 45 km. Lowering the density in this region during inversion does not raise the shear velocity to the oceanic norm. A nearby off-ridge path that covers the Cape Basin and part of the western Walvis Ridge shows no sign of thickened crust. No significant differences from normal oceanic lithosphere exist below 50 km, and no signs of thinning of the lithosphere under the Walvis Ridge are apparent. Other geophysical data rule out a thermal cause for the low mantle shear velocity, and it is likely that unusual mantle composition is responsible.

# 1. INTRODUCTION

The Walvis Ridge is a long linear feature of high bathymetric relief stretching from the Mid-Atlantic Ridge to the African continental margin in the South Atlantic Ocean (Figure 1). Morphologically, it is divided into two provinces, the continuous blocky ridge section east of $2^{o}$E and the irregular seamount-guyot section at the younger western end. Structures like the Walvis Ridge are found throughout the world oceans and are called aseismic ridges since they do not exhibit the narrow band of seismic activity that characterizes mid-ocean spreading centers. Deep sea drilling evidence indicates that aseismic ridges have undergone subsidence since formation at rates similar to that of normal oceanic lithosphere and were formed contemporaneously with the surrounding ocean basins (Detrick et al., 1977). Many models for the formation of aseismic ridges have been proposed (Dingle and Simpson, 1976), but the 'hot spot' plume hypothesis has received increasing support (Wilson, 1963; Morgan, 1971, 1972; Goslin and Sibuet, 1975; Detrick and Watts, 1979). While this mode of creation fits well into the kinematic framework of plate tectonics, the impact on the deep structure is less clear.

Detrick and Watts (1979) summarized the available seismic refraction data for aseismic ridges. At least nine lines have been shot, but only one reversed line reaching mantle-like velocities exists, indicating a 16 km thick oceanic crust overlying a low velocity ($V_p$ = 7.93 km/s) mantle on the Nazca Ridge (Cutler, 1977). Crustal thickness of at least 25 km has been inferred for the Iceland-Faeroes Ridge (Bott et al., 1971). Low velocity mantle under a thickened oceanic crust also exists on the Concepcion Bank near the Canary Islands (Weigel et al., 1978). The refraction lines shot on the Walvis Ridge display layer 2 like velocities of 5.45 km/s at depths of 10 km (Goslin and Sibuet, 1975).

The free air gravity anomaly across aseismic ridges is typically less than 75 mGal, indicating some degree of isostatic compensation. Most investigators have inferred Airy-type compensation by crustal thickening. Goslin and Sibuet (1975) modeled the eastern Walvis Ridge with an Airy crustal thickness of 25 km, but Kogan (1976) preferred a flexural model with a 10 to 15 km crust. Detrick and Watts (1979) used

Fourier techniques to show that the ridge could be fit with an Airy model at the blocky eastern end, but that a flexural model was best for the western seamount province with a much thinner crust. While gravity data can be used to infer shallow structure, the result depends on initial assumptions and is nonunique. In particular, mantle density changes as large as 0.2 $g/cm^3$ will result in Airy crustal thickness changes of only a few kilometers.

Owing to the paucity of information on the deep structure of aseismic ridges, the present work was undertaken to determine their lithospheric structure from surface wave dispersion. Surface waves are sensitive to averages of the velocity structure in the vertical direction, with the longer period waves sampling the deeper layers. By measuring the phase or group velocity of Rayleigh waves as a function of period an estimate of the average mantle velocity structure can be made. It will be shown that for the Walvis Ridge a combination of crustal thickening and anomalously low velocity upper mantle material, extending to depths of at least 30-40 km, is required to fit the dispersion data. Crustal thickening is consistent with both seismic refraction and gravity data, while low velocity mantle is suggested for several other supposed hot spot regions (Cutler, 1977; Weigel et al., 1978; Stewart and Keen, 1978).

## 2. DATA

Because of the narrow, linear shape of aseismic ridges, only limited combinations of source and observation points will produce great circle surface wave paths along the strike of the structure. The geographic distribution of World-Wide Standard Seismographic Network (WWSSN) stations severely limits the number of aseismic ridges that can be studied in this way. In the 15 year period since the advent of WWSSN stations only two suitable events were found. Figure 1 shows their great circle paths to the instruments at Sa da Bandeira, Angola (SDB) and Windhoek, Southwest Africa (WIN). Table I summarizes the epicenter information from the International Seismological Center (ISC) Bulletin. Both events are well located owing to the large number of travel time observations with residuals of less than 2 s.

Ideally, one would like to measure both group and phase velocity

FIGURE 1

Bathymetric map showing the great circle paths to stations SDB and WIN. Depths are in thousands of meters, and the stippled area is shallower than 3000 m. Contours are from E. Uchupi and H.Hays (unpublished data, 1978).

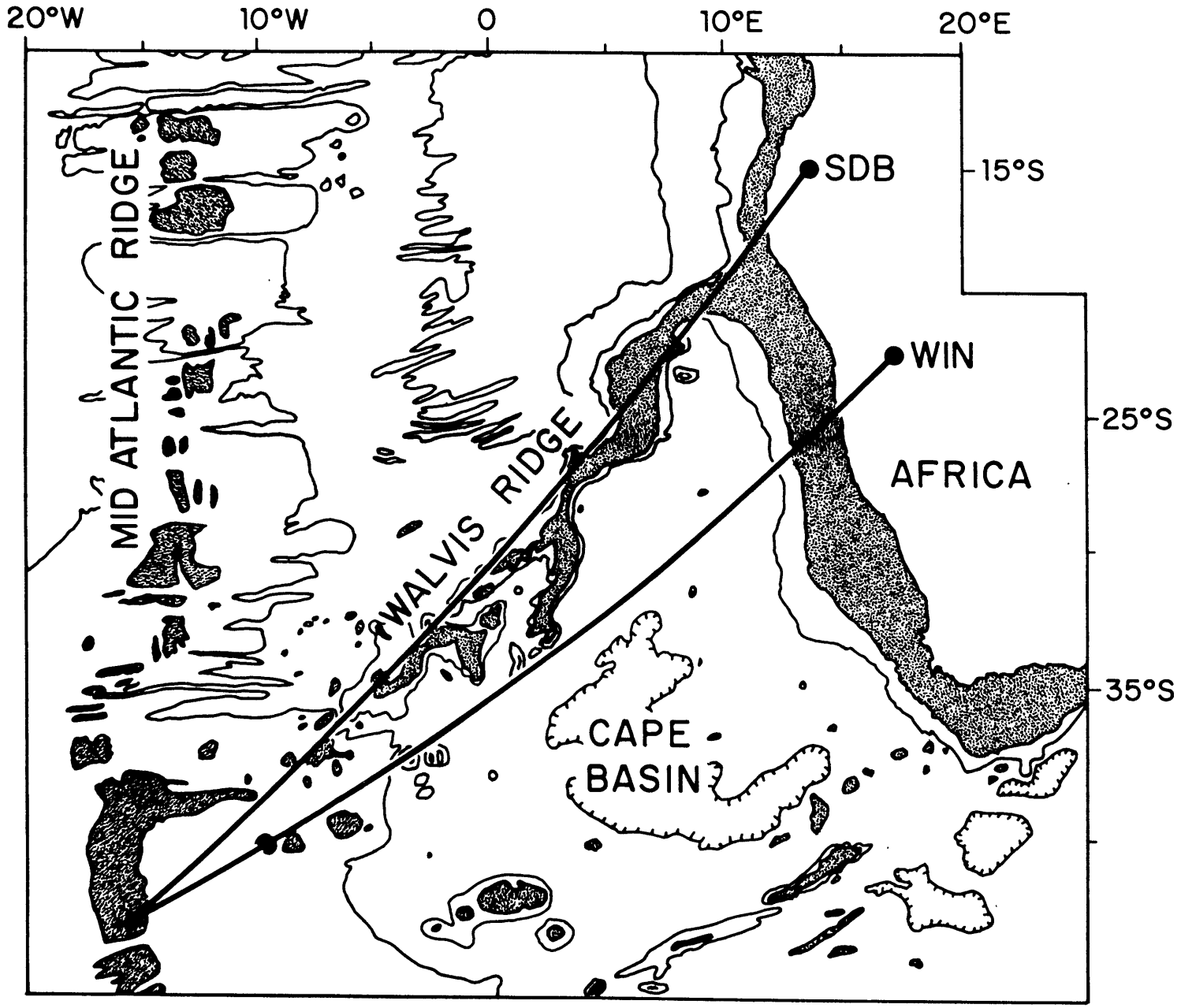
20°W
10°W
0
10°E
20°E
15°S
25°S
35°S
SDB
WIN
MID ATLANTIC RIDGE
WALVIS RIDGE
AFRICA
CAPE
BASIN

TABLE 1

EARTHQUAKE EPICENTERS FROM ISC BULLETIN

| Date | April 19, 1968 | April 19, 1968 |
|---|---|---|
| Origin Time, UT | 0808:21.0 ± 0.23 | 0904:28.2 ± 0.27 |
| Latitude, $^{o}$S | 42.70 ± 0.054 | 42.69 ± 0.061 |
| Longitude, $^{o}$W | 16.06 ± 0.056 | 16.05 ± 0.070 |
| Depth, km | 19 ± 0.7 | 33 |
| Standard Deviation, s | 1.12 | 1.56 |
| $M_b$ | 5.0 | 5.5 |
| Observations | 30 | 50 |

for these surface wave paths. Group velocity is more sensitive to structural details, particularly above the low velocity zone (Der et al., 1970), but phase velocity produces a more linear forward problem. It is possible to match group velocity dispersion data to widely disparate velocity models, and phase velocity information serves to discriminate between these. There is a trade-off between shallow and deep structure with group velocity due to a zero crossing in the partial derivatives with respect to velocity and density. Computation of group velocity is easy for a single observing station, while computation of phase velocity requires either two stations or assumptions about the source initial phase and one station. A fault plane solution is required to estimate the initial phase using standard earthquake models. The station azimuthal distribution in the South Atlantic is very poor, and no fault plane solutions could be obtained for these events. This study will use only group velocity measurements.

The long period vertical seismograms for each event and station were obtained, digitized at closely spaced (about 0.5 s) intervals, and linearly interpolated to 2 s samples. Figure 2 shows the Airy phases for each event. The wave trains are remarkably clean and free from the beating that would indicate extensive multiple path interference.

Group velocity was determined by the multiple filter technique of Dziewonski et.al. (1969). The group delay time is measured by multiplying the Fourier transformed data by a Gaussian filter centered on the period of interest and searching for the energy peak. The group velocity is the path length, assumed to be least distance or great circle, divided by the group delay time. The great circle distances were calculated using first order corrections for the ellipticity of the earth (Thomas, 1965). In all cases the instrument response was removed using the equations of Hagiwara (1958) as corrected by Brune (1962), and the instrument resonance and damping parameters from Mitchell and Landisman (1969). The choice of filter bandwidths is important, since too narrow a filter will ring and produce false peaks while too wide a filter yields data which are statistically dependent owing to overlap between adjacent filters. The filters were spaced on equal logarithmic period increments, and

FIGURE 2

Airy phases for, from top to bottom, event 1 at SDB and WIN and event 2 at SDB and WIN. The different appearance of the records at the two stations is due to the different speeds of the recording drum.

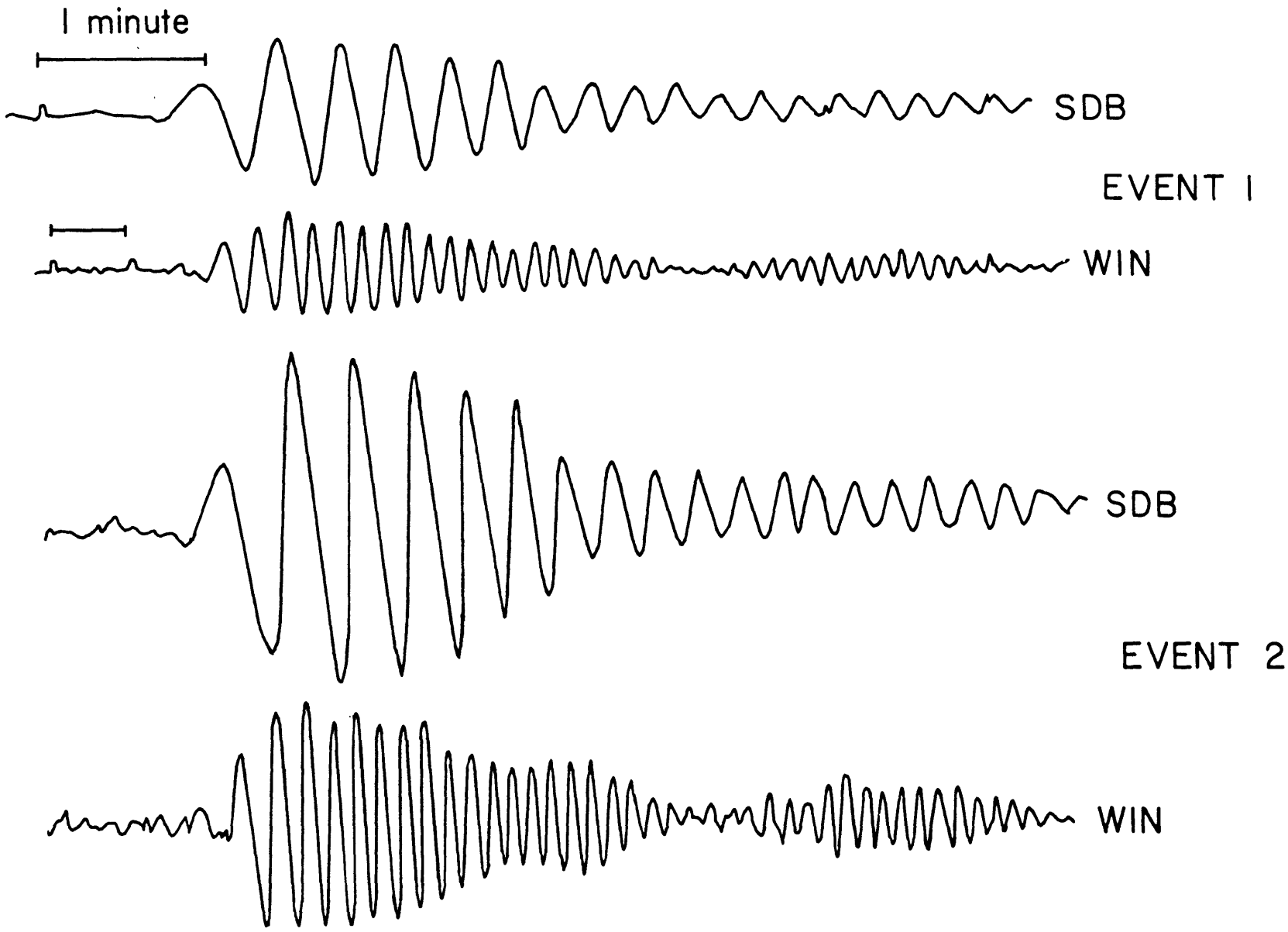
1 minute
SDB
EVENT 1
WIN
SDB
EVENT 2
WIN

the bandwidths were selected by requiring that the uncertainty principal of Der et al. (1970) be met or exceeded. The computed group velocity for each event was averaged for each path, and the result appears in Table 2 and Figure 3. The high precision of the measurements is reflected in the repeatability to within 0.01 km/s of the two independent determinations for each path.

## 3. ERROR ANALYSIS

An estimate of the probable errors and sources of error was made to see if the difference between the SDB and WIN dispersion was real. Errors in data and analysis techniques can be classified as random or systematic. For digital seismic data, random error includes digitization inaccuaracy, quantization noise, and uncertainty in the computation of spectral peaks due to the short data sections that must be used. Digitization errors were checked by multiple analyses on the seismograms and proved to be insignificant. The normal branch of the computed dispersion curves compares favorably to peak and trough measurements for the SDB seismograms. Quantization noise is minimized by using high-amplitude seismic data and a fine digitization increment. The effect of short data sections can be minimized by using wide enough bandpass filters to provide some smoothing. An uncertainty was assigned to each velocity on the basis of the width of the spectral peak and is believed to represent the random error adequately.

Systematic errors will affect only the absolute level of the dispersion curve and cannot explain the shape difference between the South Atlantic and Pacific results in Figure 3. Sources of systematic error include epicenter mislocation and origin time computation, source rise time and finiteness, lithospheric anisotropy, path error, and station timing error. Each of these will be discussed in turn to yield an estimate of the actual uncertainty in the data.

Epicenter mislocation is probably the largest source of systematic error. For these events the path length is near 4200 km, and a radial error of 10 km at this range results in a group velocity error of 0.01 km/s. An error of 40-50 km is required to explain the difference between the dispersion seen at SDB and WIN, and mislocation

TABLE 2

GROUP VELOCITY DATA

| Period | SDB Group Velocity | Uncertainty | WIN Group Velocity | Uncertainty |
|---|---|---|---|---|
| 13.6 | 3.220 | 0.060 | 3.195 | 0.080 |
| 15.9 | 3.535 | 0.030 | 3.470 | 0.020 |
| 18.5 | 3.610 | 0.025 | 3.635 | 0.020 |
| 21.6 | 3.710 | 0.015 | 3.795 | 0.025 |
| 25.2 | 3.785 | 0.025 | 3.875 | 0.025 |
| 29.4 | 3.845 | 0.025 | 3.935 | 0.025 |
| 34.2 | 3.885 | 0.025 | 3.970 | 0.020 |
| 39.9 | 3.905 | 0.025 | 4.000 | 0.030 |
| 46.5 | 3.920 | 0.030 | 4.005 | 0.025 |
| 54.3 | 3.925 | 0.020 | 4.000 | 0.020 |
| 63.3 | 3.895 | 0.040 | 3.970 | 0.030 |
| 73.8 | 3.865 | 0.040 | 3.950 | 0.035 |
| 86.0 | 3.850 | 0.030 | 3.860 | 0.020 |

FIGURE 3

Group velocity dispersion curves for the two events at SDB (squares) and WIN (triangles) and for the 20 to 50 m.y. pure path result of Forsyth (1973) (circles). Errors are discussed in the text.

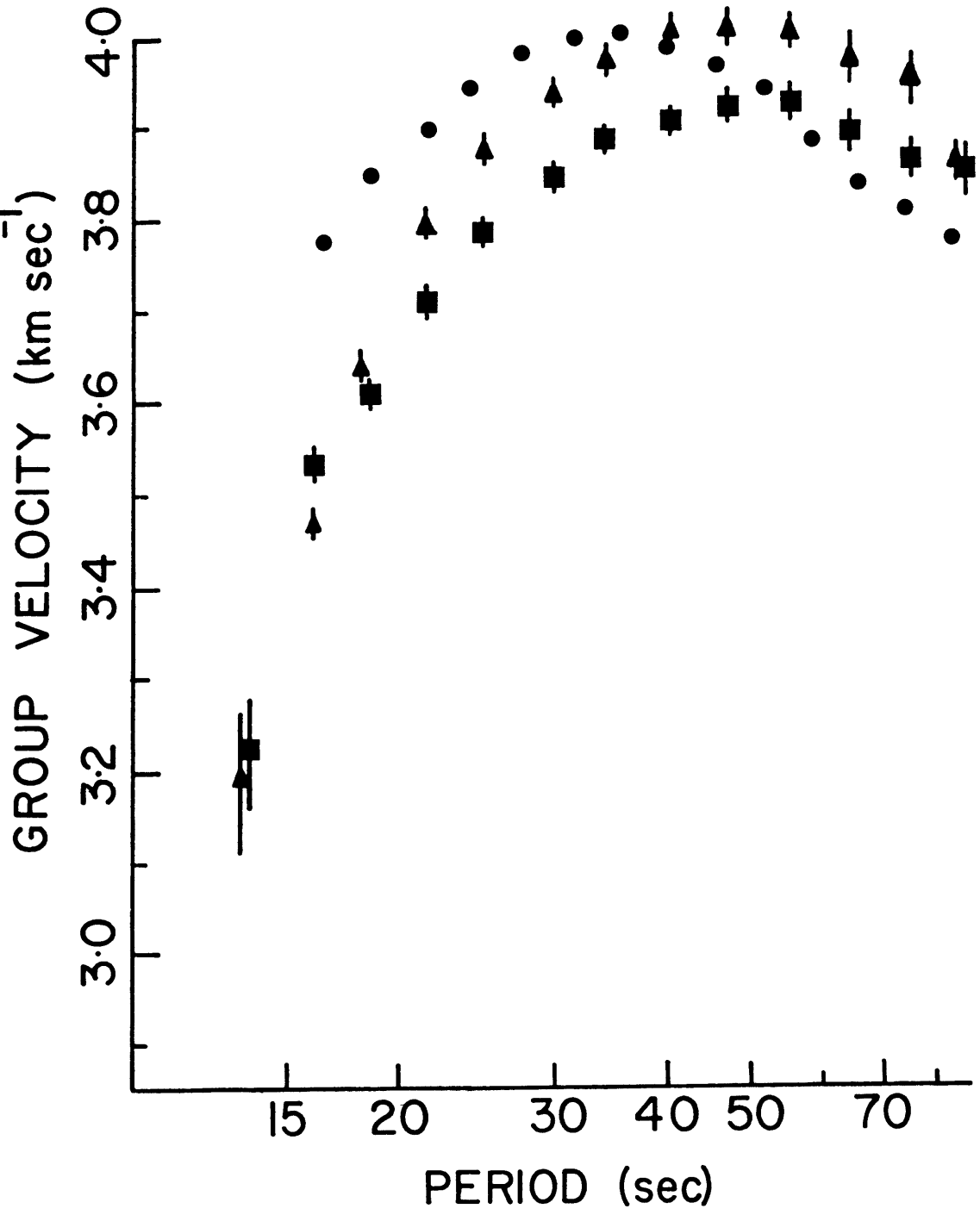
GROUP VELOCITY (km sec$^{-1}$)
4·0
3·8
3·6
3·4
3·2
3·0
15
20
30
40
50
70
PERIOD (sec)

by this amount must be considered unlikely.

Origin time computation errors can occur owing to inhomogeneity in the velocity structure of the earth. The large lateral velocity changes associated with the thermal structure of mid-ocean ridges can lead to origin time errors as large as 1 s (Forsyth and Press, 1971).

Rise time and source finiteness errors arise because no real earthquake is a point source in either time or space. Data on source rise time for small earthquakes are lacking, and it is assumed to be smaller than 1 s. Source finiteness error is of the order of L/V, where L is the fault length and V is the rupture velocity. For small earthquakes ($M_b$ = 5-6) L is near 10 km (Hanks and Thatcher, 1972) and V is in the range of 2-4 km/s (Kanamori, 1970), leading to an uncertainty of about 3 seconds.

Azimuthal anisotropy that is depth and therefore frequency dependent exists in the the oceanic lithosphere. Forsyth (1975) reports a maximum anisotropy of 2% in the east Pacific, while Yu and Mitchell (1979) found no more than 0.8% in the central Pacific. No anisotropy determinations have been made for the Atlantic Ocean basins. The azimuthal difference between the two paths in Figure 1 is only $20^{\circ}$, and an anisotropy of at least 8% is required to explain the interstation variation.

Surface waves travel a least time rather than a least distance path, and in the presence of lateral velocity changes the true path may deviate from a great circle. The clean appearance of the seismograms in Figure 2, especially at SDB, argues against significant multipath transmission. Station timing errors were checked by measuring the P arrival times on the short period vertical seismograms. Residuals are smaller than 1 s using the travel time tables of Herrin (1968).

The uncertainties given in Table 2 are the root-mean-square sum of the standard errors from the group velocity measurement, the epicenter mislocation error, the origin time error, and the source finiteness error. This is the best estimate available and probably overestimates the true uncertainty.

The differences observed between the on-ridge and off-ridge dispersion are real and cannot be eliminated even by consideration of

cumulative small errors. This implies that there is unusual velocity structure associated with the Walvis Ridge rather than an anomaly of more regional extent.

## 4. INVERSION

In Figure 3 the group velocities for both South Atlantic paths are compared to the 20 to 50 m.y. curve from Forsyth (1973) for the Pacific. For both measurements the group velocity at periods out to 30-40 s is significantly lower, indicating a deficiency of high velocity material in the upper layers. Marked differences between the shapes of the two South Atlantic curves and between them and the Pacific curve are seen and cannot be eliminated by the errors discussed in the last section. Since dispersion curve shape reflects the velocity distribution with depth more than its acual magnitude, some variation on the usual monotonic decrease in shear velocity with depth down to the low velocity zone is expected along both paths. The difference is more marked for the on-ridge (SDB) path. Long period discrepancies are apparent but involve only a few data points at periods where spectral resolution is not high and should not be emphasized.

Most velocity models derived from surface wave dipsersion are fit to the data without indicating which features of the model are actually required by the data. Modern inverse theory gives a way to determine both the necessary model parameters and the resolution of the individual layers. The details of this technique can be found in the literature (Jackson, 1972; Wiggins, 1972) and will only be outlined here. A starting model is proposed, used to compute the partial derivatives of the data with respect to the unknowns, and compared to the data. First order corrections to the model are derived and applied to it, and the process is repeated iteratively until changes to the model are small. The layer structure remains unchanged during the inversion so that the result is influenced by the choice of a starting model. Owing to nonlinearity, the trade-off between shallow and deep structural changes, and the lack of other data to constrain the inversion, the smallest difference from a standard earth model, used as a starting model, was searched for by trial and

error modification of the layer thicknesses. The partial derivatives are recomputed for each iteration, significantly increasing the parameter range for convergence with a given starting model.

Rayleigh waves are sensitive to a combination of shear and compressional velocity, and density. Most inversions have focussed on shear velocity since its effect is large at all depths, but compressional velocity and density may exert a significant influence near the surface. Figure 4 shows the partial derivatives of group velocity with respect to all three parameters for the final on-ridge model. It is clear that compressional velocity is not a major factor except in the water and upper crustal layers to depths of 5 km and can safely be neglected unless details of the crustal structure are desired and can be resolved. Density can affect the results into the upper mantle and in the low velocity zone. Since no good independent way to estimate mantle density exists, the data were inverted for shear velocity alone. The effect of density changes in the final model were then evaluated by perturbing the layer densities at different depths. It should be noted that the shear velocity and density partial derivatives have different signs near the surface at all periods; hence a decrease in near surface density implies an increase in shear velocity, and vice versa.

The starting model was similar to that of Forsyth (1973, 1975) and to simple oceanic models from Knopoff (1972). It consists of a water layer, a single crustal layer, a high-velocity upper mantle lid, a low-velocity channel, a subchannel, and a half space. The water depth was measured on the bathymetric charts of E. Uchupi and H. Hays (unpublished data, 1978), and an average for the great circle path was taken. Sediment cover on the Walvis Ridge is patchy, reaching 1 km only in isolated places (Dingle and Simpson, 1976) and is no more than 400 m thick in the Cape Basin (Ewing et al., 1966), so no sediment layer was included. The crustal velocity was an average for layer 3 from Christensen and Salisbury (1975). The upper mantle velocities and densities are from Forsyth (1973). The compressional velocity was fixed at 8.0 km/s except in the low velocity zone, where 7.8 km/s was used. Mantle density was set at 3.4 and crustal density at 3.0 $g/cm^3$. Typically, three or four iterations sufficed for convergence of the

FIGURE 4

Partial derivatives of group velocity at 16, 40, and 63 s periods with respect to compressional velocity (dotted line), shear velocity (solid line), and density (dashed line) for the final ridge model.

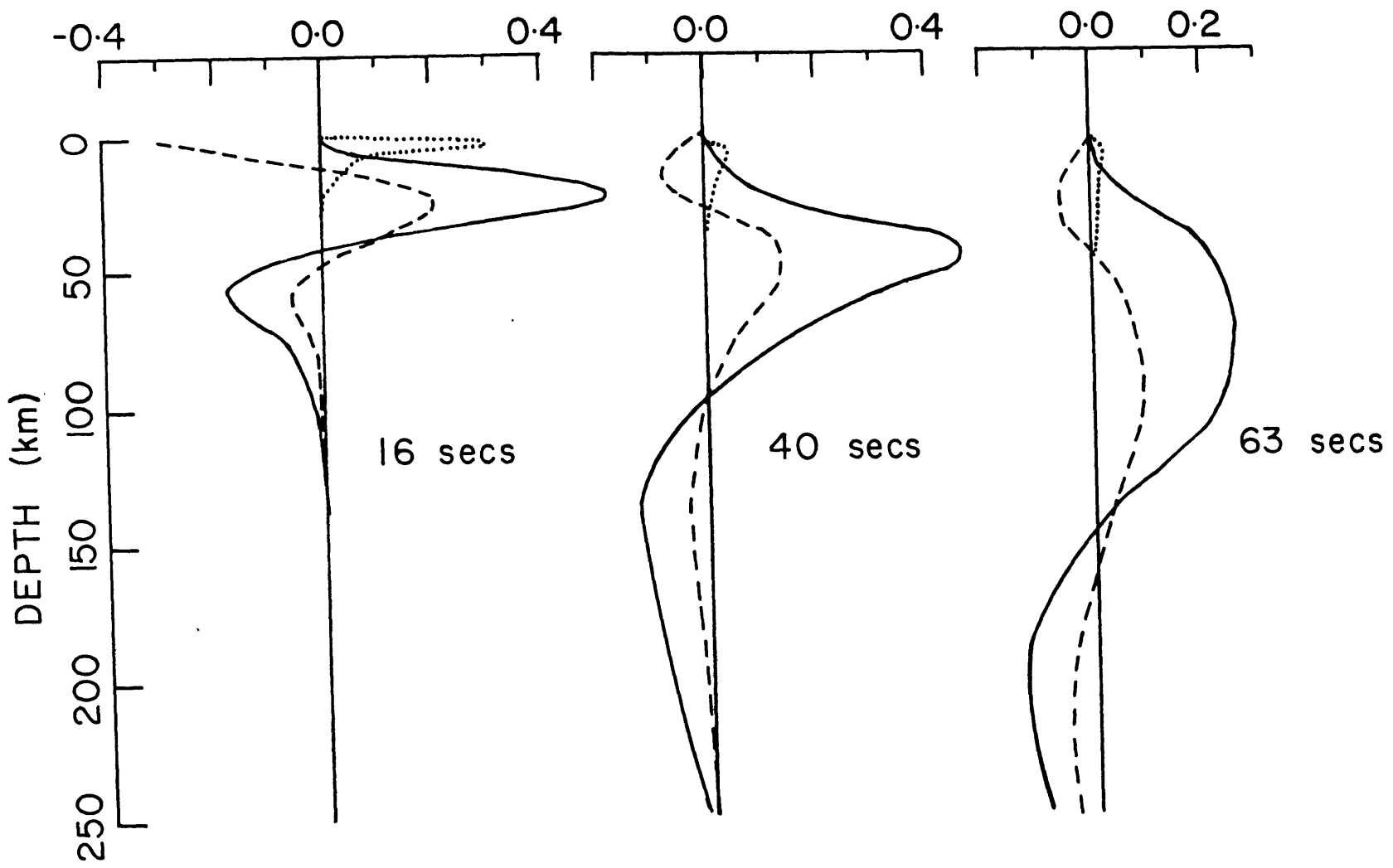
-0·4
0·0
0·4
0·0
0·4
0·0
0·2
0
50
100
150
200
250
DEPTH (km)
16 secs
40 secs
63 secs

inversion. The final models were then checked and found to be insensitive to the starting shear velocities.

## 5. RESULTS

Figure 5 shows the best models for both the on-ridge (SDB) and off-ridge (WIN) paths compared to the velocity structure for 20 to 50 m.y. lithosphere in the east Pacific (Forsyth, 1973). Table 3 lists the final model parameters and standard deviations for the shear velocities in each layer. Since the paths in this study are orthogonal to the isochrons, the dispersion should reflect a velocity structure that is an average for lithosphere of zero age to the early opening of the South Atlantic at about 130 Ma (Ma = m.y.b.p.). The velocity structure of the oceanic upper mantle evolves rapidly for the first 50 m.y. Changes in the velocity structure for older lithosphere are small, amounting to no more than 0.1 km/s (Forsyth, 1977), and the 20 to 50 m.y. structure is a representative average for normal oceanic lithosphere. Studies in the Atlantic indicate somewhat higher upper mantle shear velocity than in the Pacific structure (Weidner, 1973). Figures 6 and 7 are the residuals and resolving kernels for the respective models. The fit to the data is good at all except the shortest periods, where water depth variations, sediment thickness and velocity variations, and crustal inhomogeneity along the path will cause significant lateral refraction and increase the scatter in the data. In the off-ridge model the longest and shortest period data seriously degraded the results and were not used in the final inversion.

The resolving kernels of Figure 7 can be thought of as windows through which the velocity structure is viewed. If the individual layers are perfectly resolved, then only the velocity of one layer will be seen for each kernel. The widths of the kernels determine the depth resolution at each layer. A trade-off between layer thickness and shear velocity is possible, and well resolved layers can mean poorly known velocities. It is clear that the good depth resolution implied by Figure 7 is matched by good resolution of the velocities within each layer. The resolving kernels are compact, with little trade-off possible between different parts of the model. Attempts to increase the number of layers resulted in solutions that were oscillatory and

FIGURE 5

Models of the shear velocity structure resulting from the inversion of the two dispersion curves compared to the 20 to 50 m.y. structure of Forsyth (1973). The solid line is for the on-ridge (SDB) path, the long-dashed line is for the off-ridge (WIN) path, and the short-dashed line is for Forsyth's result.

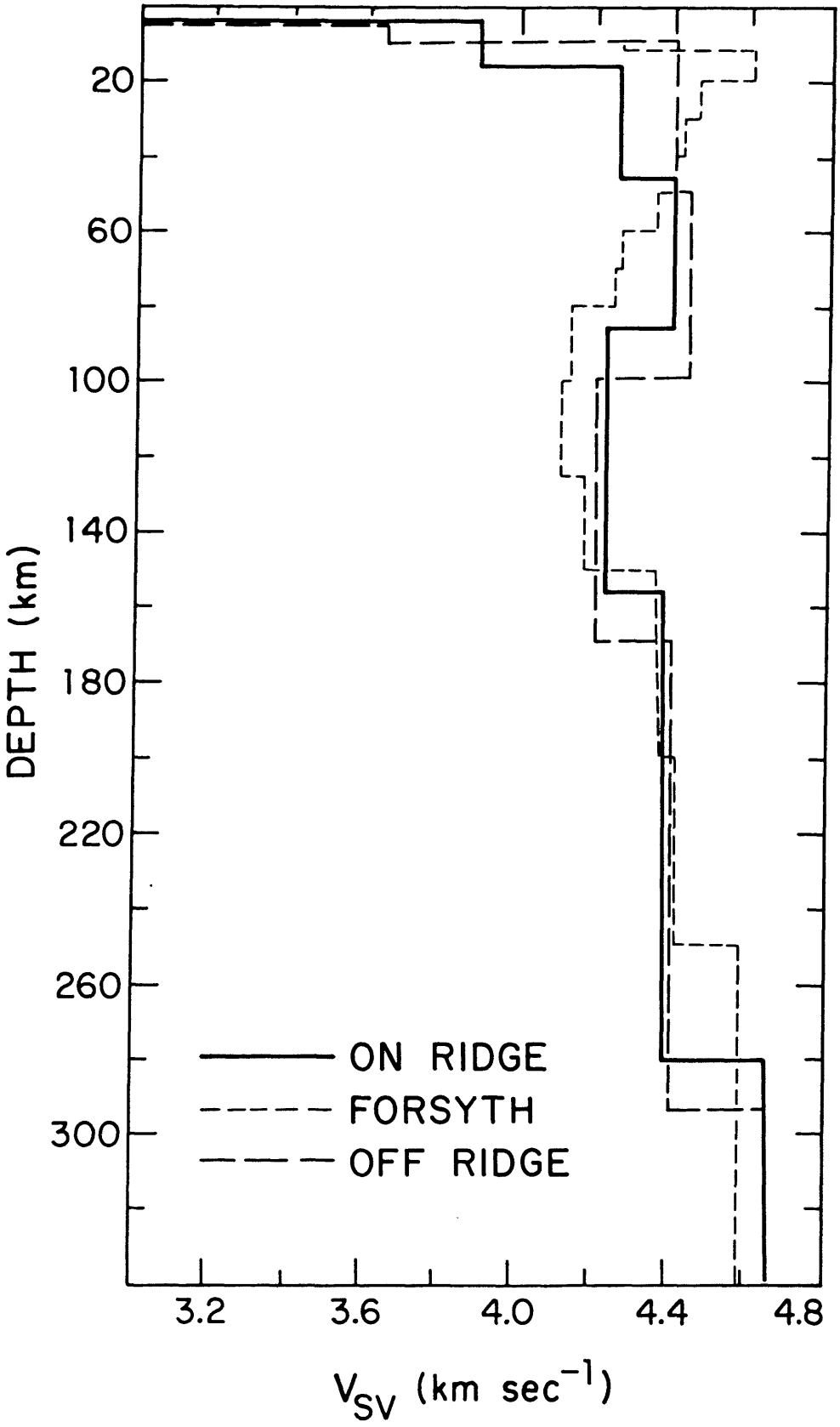
20
60
100
140
180
220
260
300
DEPTH (km)
ON RIDGE
FORSYTH
OFF RIDGE
3.2
3.6
4.0
4.4
4.8
$V_{SV}$ (km sec$^{-1}$)

TABLE 3

FINAL MODEL PARAMETERS

| Layer | Thickness | $V_p$ | $V_s$ | ± | Density |
|---|---|---|---|---|---|
| | | On-Ridge (SDB) | | | |
| 1 | 3.5 | 1.52 | 0.00 | 0.000 | 1.03 |
| 2 | 12.5 | 7.00 | 3.90 | 0.076 | 3.00 |
| 3 | 30.0 | 8.00 | 4.26 | 0.023 | 3.40 |
| 4 | 40.0 | 8.00 | 4.40 | 0.023 | 3.40 |
| 5 | 70.0 | 7.80 | 4.21 | 0.039 | 3.40 |
| 6 | 125,0 | 7.80 | 4.37 | 0.026 | 3.40 |
| 7 | Half Space | 8.00 | 4.65 | 0.000 | 3.40 |
| | | Off-Ridge (WIN) | | | |
| 1 | 4.5 | 1.52 | 0.00 | 0.000 | 1.03 |
| 2 | 5.0 | 6.70 | 3.65 | 0.000 | 2.90 |
| 3 | 40.0 | 8.00 | 4.40 | 0.010 | 3.40 |
| 4 | 50.0 | 8.00 | 4.44 | 0.017 | 3.40 |
| 5 | 70.0 | 7.80 | 4.20 | 0.048 | 3.40 |
| 6 | 125.0 | 7.80 | 4.41 | 0.012 | 3.40 |
| 7 | Half Space | 8.00 | 4.65 | 0.000 | 3.40 |

FIGURE 6

Residuals for the (top) on-ridge and (bottom) off-ridge models.

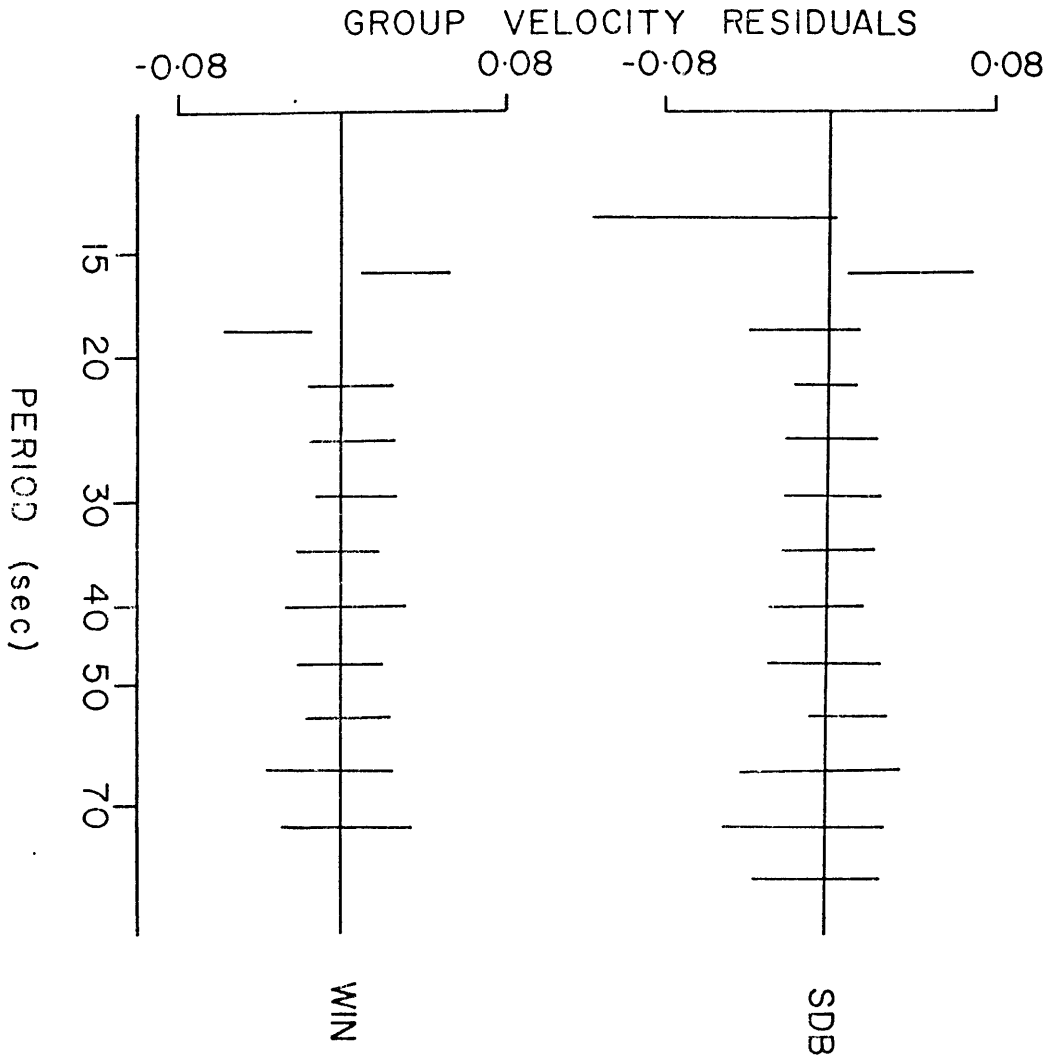
GROUP VELOCITY RESIDUALS
-0·08
0·08
-0·08
0·08
PERIOD (sec)
15
20
30
40
50
70
WIN
SDB

FIGURE 7

Resolving kernels for the (top) on-ridge and (bottom) off-ridge models for, from left to right, the second through sixth layers of Table 3. The arrows point to the layer on which the parameter us centered. See text for discussion.

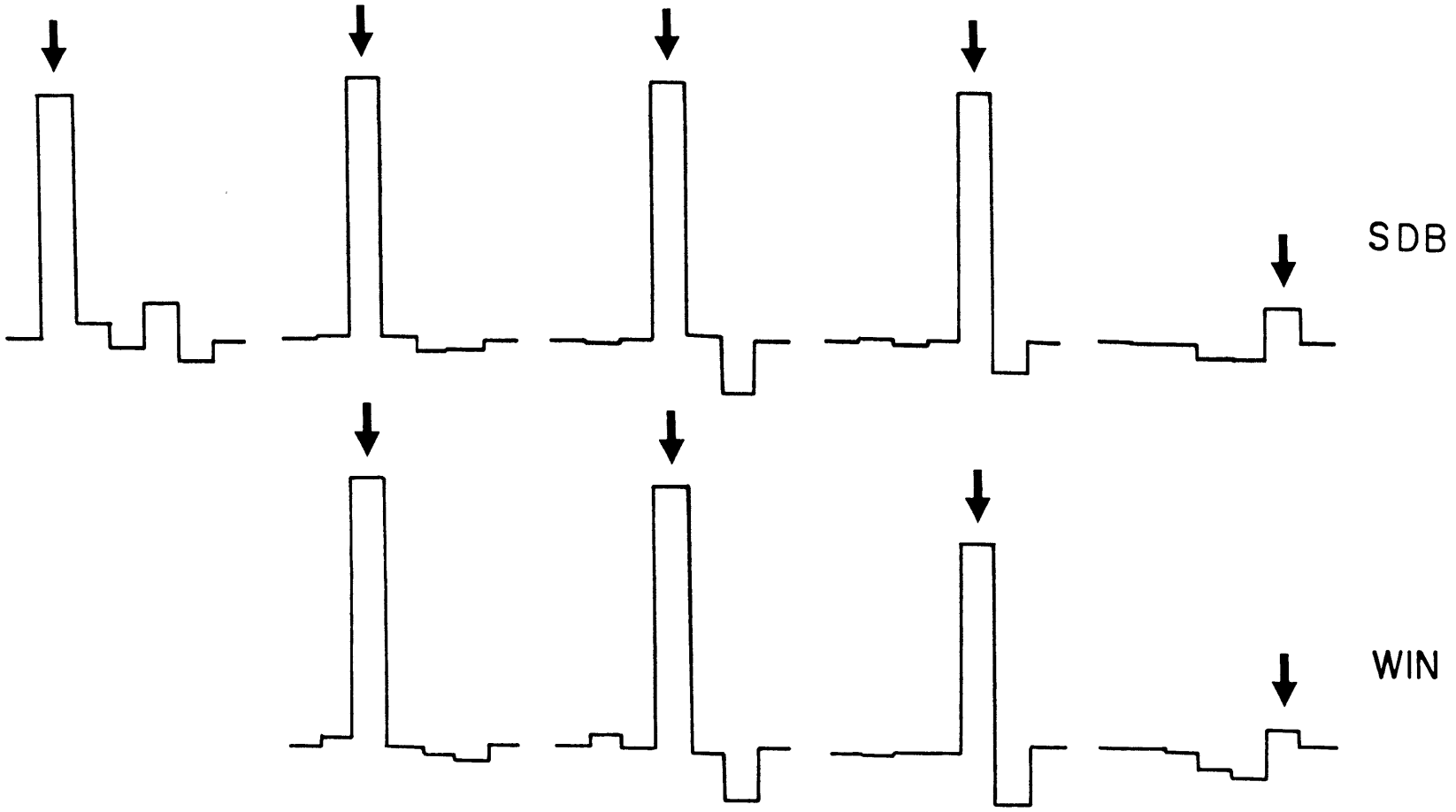
SDB
WIN

in noncompact resolving kernels, probably owing to the lack of phase velocity measurements and errors in the data. Features of both solutions include well resolved upper mantle lids and only limited interaction of near surface layers with the low velocity zone. Resolution is poor below 150 km, reflecting the lack of data beyond 90 s in period.

While surface wave dispersion data cannot locate sharp discontinuities in velocity very precisely due to inherent smoothing of the structure, some estimate of their position can be obtained by studying the effect of layer thickness on layer velocity. The choice of mantle lid thickness is bounded by the inability to resolve channel from subchannel for too thin a layer and unreasonably low subchannel velocities as the thickness increases. Sudden changes in the layer velocities indicate the approximate locations of major boundaries, especially the lid-channel transition. The resulting mantle lid is 70 km thick for the on-ridge model and 90 km thick for the off-ridge model, with uncertainties of 10-20 km. This gives a total lithospheric thickness, assuming the low velocity zone to mark the lithosphere-asthenosphere boundary, of 80-100 km for both cases. Given the possible resolution in the upper 100 km no significant thinning of the lithosphere is seen under the Walvis Ridge. No major differences from normal oceanic lithosphere existsbelow 50 km for either path.

The on-ridge structure requires both crustal thickening to 12.5 $\pm$ 3 km and low velocity ($V_s$ = 4.26 km/s) upper mantle. The uncertainty in crustal thickness was measured by varying the crustal thickness and requiring the velocity to be within the layer 3 range determined by Christensen and Salisbury (1975). Splitting the crust into layers 2 and 3 results in slight crustal thinning, but the data cannot resolve such detail. Lowereing the integrated crustal velocity raises the mantle velocity by 0.06 km/s, meaning that a finer crustal structure would increase it. Changes in mantle lid velocity do not significantly affect the crustal velocities. The low mantle lid velocity is significant when compared to an average of 4.50 km/s for the Pacific model. Since half of the path traverses lithosphere older than 50 m.y., the normal mantle shear velocity should be at least this high.

No crustal thickening is seen for the off-ridge path. Attempts to increase the thickness of the crust results in interaction with the deep layers and unreasonably high velocities. The upper mantle lid velocity is 4.40 km/s, which is intermediate between the off-ridge and normal results.

The partial derivatives of Figure 4 indicate that lowered density in the near surface layers can increase the apparent shear velocity in nearby layers. If the top 30 km of the on-ridge mantle has a density of 3.2 instead of 3.4, then the upper lid shear velocity rises to 4.30 km/s and the lower lid velocity falls to 4.33 km/s. Crustal density decreases do not appreciably influence mantle velocities but do change the crustal velocities and reduce the apparent crustal thickness. It is unlikely that the mantle density is higher than 3.4; hence the structure of Figure 5 should be regarded as a lower limit rather than an average. Rayleigh wave dispersion data alone cannot differentiate the effects of low density and low velocity.

## 6. DISCUSSION

The models presented in the last section are averages for the great circle paths of Figure 1. Lateral differences can be resolved only if many different size samples of the different regions can be measured over multiple paths. Such a procedure has been used in 'pure path' studies (Dziewonski, 1971; Forsyth, 1973, 1975), but is not applicable to the limited data of this work. Gravity data suggest different crustal thicknesses and isostatic compensation mechanisms for the eastern and western parts of the Walvis Ridge. The former is not incompatible with the surface wave determined structure, since the 12.5 km crust inferred in this work is intermediate between a 5 to 8 km thickness for the seamount province and a 15 to 30 km thickness for the block ridge province given by Detrick and Watts (1979). The inability to fit a thick crust to the WIN data also suggests that differences along the strike of the ridge are present.

The off-ridge path samples the western seamount-guyot region as well as a section of the Cape Basin (Figure 1). If the dispersion curve for the on-ridge path is taken to represent the western Walvis Ridge, then the off-ridge path can be separated into two regions by

subtraction of the group slownesses for the two paths after choosing appropriate regional boundaries. The result for the Cape Basin is not significantly different from the 100 to 135 m.y. curve of Forsyth (1977) except at short periods where crustal differences control the dipsersion. Such a crude calculation is heavily influenced by the assumed regionalization and is not statistically rigorous. Nevertheless, it suggests that the anomalous mantle region may not extend beyond a few hundred kilometers from the ridge axis.

Poisson's ratio ($\sigma$) is an elastic parameter that can be calculated if both compressional and shear velocity are known. Most peridotitic mantle materials are characterized by $\sigma$ values of 0.27-0.28 (Ringwood, 1975). If the mantle shear velocity is in the range of 4.25-4.35 km/s and $\sigma$ is 0.28 the compressional velocity must be 7.7-7.9 km/s. This is slightly lower than that reported from seismic refraction on the Nazca Ridge (Cutler, 1977). It must be emphasized that seismic refraction measures the velocity below an interface, while surface wave dispersion yields an average over a depth interval. Direct comparisons of them are difficult.

Low shear velocity in mantle rock can be caused by elevated temperature and partial melting. The temperature partial derivatives for many mantle materials have been measured in the laboratory. Using a value given by Chung (1976) for an artificial peridotite, a normal mantle velocity of 4.60 km/s, and a decrease of 0.30 km/s for the Walvis Ridge yields a temperature anomaly of 800° C. Superimposed on a normal sub-Moho temperature of 300°C, this gives an upper mantle at temperatures of at least 1100°C at a depth near 15 km. The solidus temperature of a pyrolite mantle, while strongly influenced by water content, is not over 1200°C (Ringwood, 1975), and incipient partial melting at shallow depths will result. A very small partial melt fraction, no more than a few percent, can easily produce the velocity anomaly that is seen (Anderson and Sammis, 1970).

Neither high temperature nor partial melting is consistent with other geophysical evidence. Hot material at shallow depths must produce surface heat flow effects. If the upper mantle temperature is 1000°C at a depth of 15 km and the thermal conductivity is 0.006 $cal\,^{o}C^{-1}cm^{-1}s^{-1}$, the surface heat flow is at least 4 HFU (1 HFU =

1 cal $cm^{-2}s^{-1}$). The observed heat flow is only 2 HFU, or 0.7 HFU above that in the surrounding ocean basins, probably a result of a larger reservoir of radioactive material (Lee and Von Herzen, 1977). High temperature in the mantle will lead to thermal expansion and density changes which will produce large regional elevation anomalies. Uplift of several kilometers must result from the effective lithospheric thinning due to the high temperature, as may occur under mid-ocean island swells (Detrick and Crough, 1978; Crough, 1978). No noticeable long wavelength bathymetric features are apparent on either bathymetric charts or profiles crossing the Walvis Ridge. For these reasons an alternate hypothesis must be sought.

Compositional zoning in the mantle, especially that associated with supposed mantle plumes, has received increasing geochemical support (Schilling, 1973, 1975). Trace element data, particularly strontium and lead isotopic data, indicate marked differences of the mantle sources for Walvis Ridge volcanics from those in other oceanic provinces (Gast et al., 1964; Oversby and Gast, 1970). It is likely that the low mantle velocity under the Walvis Ridge is due to unusual mantle composition associated with the surface geochemical anomalies. Quantitative correlation of the geophysical and geochemical evidence requires more complete petrological and laboratory data.

## 7. CONCLUSIONS

From the Rayleigh wave dispersion study of the Walvis Ridge the following conclusions can be drawn:

1. The Walvis Ridge exhibits an average crustal thickness that is 1.5-2 times the oceanic norm. This is consistent with the limited seismic refraction data for aseismic ridges and a gravity study on the Walvis Ridge by Detrick and Watts (1979).

2. The top 30 km of upper mantle under the Walvis Ridge is composed of low shear velocity material ($V_s$ = 4.25-4.35 km/s). Even if the mantle density is as low as 3.2 $g/cm^3$ to depths of 40-50 km, the shear velocity in the mantle is far below the normal value for oceanic lithosphere of moderate age.

3. The low velocity cannot be explained by partial melting or high temperature at the base of the crust, since the observed heat flow and

regional elevation is not radically different from that in the surrounding ocean basins. The low shear velocity may be due to compositional zoning of the mantle.

# REFERENCES

Anderson, D., and C. Sammis, 1970. Partial melting in the upper mantle, Phys. E. Pl. Int. 3, 41-50.

Bott, M.H.P., C.W.A. Browitt, and A.P. Stacey, 1971. The deep,structure of the Iceland-Faeroes Ridge, Mar. Geophys. Res. 1, 328-357.

Brune, J.N., 1962. Correction of initial phase measurements for the southeast Alaska earthquake of July 10, 1958, and for certain nuclear explosions, J. geophys. Res. 67, 3643-3644.

Christensen, N.I., and M.H. Salisbury, 1975. Structure and constitution of the lower oceanic crust, Rev. Geophys. 13, 57-86.

Chung, D.H., 1976. On the composition of the oceanic lithosphere, J. geophys. Res. 81, 4129-4134.

Crough, S.T., 1978. Thermal origin of mid-plate hot-spot swells, Geophys. J. Roy. astr. Soc. 55, 451-469.

Cutler, S.T., 1977. Geophysical investigation of the Nazca Ridge, M.S. Thesis, Univ. of Hawaii, Honolulu.

Der, Z., R. Masse, and M. Landisman, 1970. Effects of observational errors on the resolution of surface waves at intermediate distances, J. geophys. Res. 75, 3399-3409.

Detrick, R.S. and S.T. Crough, 1978. Island,subsidence, hot spots, and lithospheric thinning, J. geophys. Res. 83, 1236-1244.

Detrick, R.S., and A.B. Watts, 1979. An analysis of isostasy in the world's oceans: Part 3- aseismic ridges, J. geophys. Res. 84, 3637-3653.

Detrick, R.S., J.G. Sclater, and J. Thiede, 1977. The subsidence of a aseismic ridges, E. Pl. Sci. Lett. 34, 185-196.

Dingle, R.V., and E.S.W. Simpson, 1976. The Walvis Ridge: a review, in C.L. Drake (ed.), Geodynamics: Progress and Prospects, Washington D.C.: AGU, pp. 160-176.

Dziewonski, A., 1971. Upper mantle models from 'pure path' dispersion data, J. geophys. Res. 76, 2587-2601.

Dziewonski, A., S. Block, and M. Landisman, 1969. A technique for the analysis of transient seismic signals, Bull. Seism. Soc. Am. 59, 427-444.

Ewing, M., X. Le Pichon, and J. Ewing, 1966. Crustal structure of the mid-ocean ridges, 4. sediment distribution in the South Atlantic Ocean and the Cenozoic history of the Mid-Atlantic Ridge, J. geophys. Res. 71, 1611-1636.

Forsyth, D.W., 1973. Anisotropy and the early structural evolution of the oceanic upper mantle, Ph.D. thesis, Mass. Inst. of Tech. and Woods Hole Oceanogr. Inst., 255 pp.

Forsyth, D.W., 1975. Anisotropy and the early structural evolution of the oceanic upper mantle, Geophys. J. Roy. astr. Soc. 43, 103-162.

Forsyth, D.W., 1977. The evolution of the upper mantle beneath mid-ocean ridges, Tectonophysics 38, 89-118.

Forsyth, D.W., and F. Press, 1971. Geophysical tests of petrological models of the spreading lithosphere, J. geophys. Res. 76, 7963-7979.

Gast, P.W., G.R. Tilton, and C. Hedge, 1964. Isotopic composition of lead and strontium from Ascension and Gough Islands, Science 145, 1181-1185.

Goslin, J., and J.-C. Sibuet, 1975. Geophysical study of the easternmost Walvis Ridge, South Atlantic: deep structure, Geol. Soc. Am. Bull. 86, 1713-1724.

Hagiwara, T., 1958. A note on the theory of the electromagnetic seismograph, Bull Earth. Res. Inst., Tokyo 36, 139-164.

Hanks, T.C.,aand W. Thatcher, 1972. A graphical representation of seismic source parameters, J. geophys. Res. 77, 4393-4405.

Herrin, E. (chairman), 1968. 1968 seismological tables for P phases, Bull. Seism. Soc. Am. 58, 1193.

Jackson, D.D., 1972. Interpretation of inaccurate, insufficient, and inconsistent data, Geophys. J. Roy. astr. Soc. 28, 97-109.

Kanamori, H., 1970. The Alaska earthquake of 1964: radiation of long-period surface waves and source mechanism, J. geophys. Res. 75, 5029-5040.

Knopoff, L., 1972. Observation and inversion of surface wave dispersion, Tectonophysics 13, 497-519.

Kogan, M.G., 1976. The gravity field of oceanic block ridges, Izv. Acad. Sci. USSR. Phys. Solid Earth 12, 710-717.

Lee, T.-C., and R.P. Von Herzen, A composite trans-Atlantic heat flow profile between 20°S and 35°S, E. Pl. Sci. Lett. 35, 123-133.

Mitchell, B.J., and M. Landisman, 1969. Electromagnetic seismograph constants by least squares inversion, Bull. Seism. Soc. Am. 59, 1335-1348.

Morgan, J., 1971. Convection plumes in the lower mantle, Nature 230, 42.

Morgan, J., 1972. Plate motions and deep mantle convection, Geol. Soc. Am. Mem. 132, 7.

Oversby, V., and P.M. Gast, 1970. Isotopic composition of lead from oceanic islands, J. geophys. Res..75, 2097-2114.

Ringwood, A.E., 1975. Composition and Petrology of the Earth's Mantle, New York: McGraw Hill, 618 pp.

Schilling, J.-G., 1973. Iceland mantle plume, Nature 246, 104.

Schilling, J.-G., 1975. Azores mantle blob: rare earth evidence, E. Pl. Sci. Lett. 25, 103-115.

Stewart, I.C.F., and C.E. Keen, 1978. Anomalous upper mantle structure beneath the Cretaceous Fogo seamounts indicated by P-wave reflection delays, Nature 274, 788-791.

Thomas, P.D., 1973. Geodesic arc length on the reference ellipsoid to second order terms in the flattening, J. geophys. Res. 70, 3331-3340.

Weidner, D.J., 1973. Rayleigh wave phase velocities in the Atlantic Ocean, Geophys. J. Roy. astr. Soc. 36, 105-139.

Weigel, W., P. Goldflam, and K. Hinz, 1978. The crustal structure of Concepcion Bank, Mar. Geophys. Res. 3, 381-392.

Wiggins, R., 1972. The general linear inverse problem: implications of surface waves and free oscillations for earth structure, Rev. Geophys. 10, 251-285.

Wilson, J.T., 1963. Evidence from islands on the spreading of ocean floors, Nature 197, 536-538.

Yu, G.-K., and B.J. Mitchell, 1979. Regionalized shear velocity models of the Pacific upper mantle from observed Love and Rayleigh wave dispersion, Geophys. J. Roy. astr. Soc. 57, 311-341.

# CHAPTER THREE

# ELECTROMAGNETIC INDUCTION FIELDS IN THE DEEP OCEAN NORTHEAST OF HAWAII AND IMPLICATIONS FOR MANTLE CONDUCTIVITY

# ELECTROMAGNETIC INDUCTION FIELDS IN THE DEEP OCEAN NORTHEAST OF HAWAII AND IMPLICATIONS FOR MANTLE CONDUCTIVITY*

Alan D. Chave[1]

Woods Hole Oceanographic Institution
Woods Hole, MA 02543
and
Department of Earth and Planetary Sciences
Massachusetts Institute of Technology
Cambridge, MA 02139

R. P. Von Herzen

Woods Hole Oceanographic Institution
Woods Hole, MA 02543

K. A. Poehls[2]

Department of Earth and Space Science
University of California
Los Angeles, CA 90024

C. S. Cox

Scripps Institution of Oceanography
La Jolla, CA 92093

* submitted to Geophys. J. Roy. astr. Soc.

1 present address:
Geological Research Division A-015
Scripps Institution of Oceanography
La Jolla, CA 92093

2 present address:
Dynamics Technology, Inc.
Torrance, CA 90505

ABSTRACT

We have analyzed a thirty-six day recording of the natural electric and magnetic field variations obtained on the deep ocean floor northeast of Hawaii. The electomagnetic fields are dominated by tides which have an appreciable oceanic component, especially in the east electric and north magnetic components. The techniques of data analysis included singular value decomposition (SVD) to remove uncorrelated noise. There are three degrees of freedom in the data set for periods longer than five hours, indicating a correlation of the vertical magnetic field and the horizontal components, suggesting source field inhomogeneity. Tensor response functions were calculated using spectral band averaging with both SVD and least squares techniques and rotated to the principal direction. One diagonal component, determined mainly by the north electric and east magnetic fields, is not interpretable as a one dimensional induction phenomenon. The other diagonal term of the response function indicates a rapid rise in conductivity to 0.05 mho/m near 160 km. No decrease in conductivity below this depth is resolvable. Polarization analysis of the magnetic field indicates moving source fields with a wavelength near 5000 km. Model studies suggest that the two dimensionality in the response function may be caused by motion in the ionospheric current system.

# 1. INTRODUCTION

Natural electromagnetic fields in the deep ocean are induced by both ionospheric current systems and dynamo action in the moving sea water. Since the sediments, crust, and mantle are electrical conductors, the electromagnetic signals are coupled to the underlying layers by mutual induction. Observations of electric and magnetic fields in the ocean will contain information on both the electrical conductivity structure of the earth and oceanic circulation patterns.

We report here on a magnetotelluric sounding performed using simultaneous recordings of the electric and magnetic fields at two deep ocean sites northeast of Hawaii. The response functions calculated from the data and neglecting oceanic terms are used to find a conductivity-depth function for the top 400 km of the earth. We also critically examine the data for departures from ideality in the source fields and the consequences of this for the response functions themselves.

## 1.1 PREVIOUS INVESTIGATIONS

The electrical conductivity structure of the earth has been estimated by performing spherical harmonic analyses on global geomagnetic observatory data over periods of days to months (Banks, 1969; Parker, 1970). An explicit separation of the fields into internal and external parts is made and the resulting transfer function is converted to a radially symmetric, global model of the electrical conductivity. While problems exist due to large scale inhomogeneities in the earth, especially the highly conductive oceans, the deep sounding studies do indicate rapidly rising conductivity below 400 km with poor resolution of near surface structure.

In contrast, surveys on a smaller, regional scale have been carried out on continents and used to estimate near surface electrical conductivity. Experiments using arrays of magnetometers have been performed throughout North America and other continental regions (Gough, 1973). Similar techniques have been applied to understanding the coast-continent transition zone and associated anomalies (Schmucker, 1970a).

The magnetotelluric method, long used in exploration geophysics,

has recently been applied in the oceans. Starting with the early work reported in Cox et al. (1970), a handful of oceanic magnetotelluric soundings have been made (Poehls and Von Herzen, 1976; Filloux, 1977; Cox et al., 1980). The available data indicate some clear differences between the conductivity structures under oceans and continents. More highly conductive material is present at shallower depths under the oceans. A sharp increase in conductivity at depths of 100-200 km is commonly observed, and a correlation between the distance to this layer and the lithospheric age has been noted.

## 2. DATA

In August-September 1976 electric and magnetic field instrumentation was deployed at three sites about 900 km northeast of Hawaii (Figure 1). The experimental area was chosen to avoid complex tectonic regions like spreading ridges or fracture zones that may produce induction anomalies. The nearest such feature is the Murray Fracture Zone located 250 km north of the sites. The lithospheric age varies from 50 Ma at station 1 to 70 Ma at station 3 with magnetic anomaly 26 passing through station 2. The instruments were located in the red hemipelagic clay sedimentary province with thin sediment cover and frequent basement outcrops.

Filloux (1977) has reported on a magnetotelluric sounding conducted at station 3 using a three week long data set. Our measurements consist of a 36 day long, three component magnetic field record from station 2 and a simultaneous, two component horizontal electric field measurement at station 1.

Daniel (1978) made a simultaneous measurement of the east-west electric field at station 2 using a 1.5 km long wire instrument on the ocean bottom. His results indicate a squared multiple coherence of at least 0.98 with the station 1 electric field in the period range 2-96 hours. This gives us confidence that the 150 km separation between our two measurements presents no serious interpretational difficulties.

### 2.1 INSTRUMENTATION

The three component vector magnetometer utilized thin film devices whose magnetic permeability is a function of the applied

FIGURE 1

Bathymetric location map showing the locations of the electromagnetic instrumentation used in this work. The solid line is the 5200 m contour.

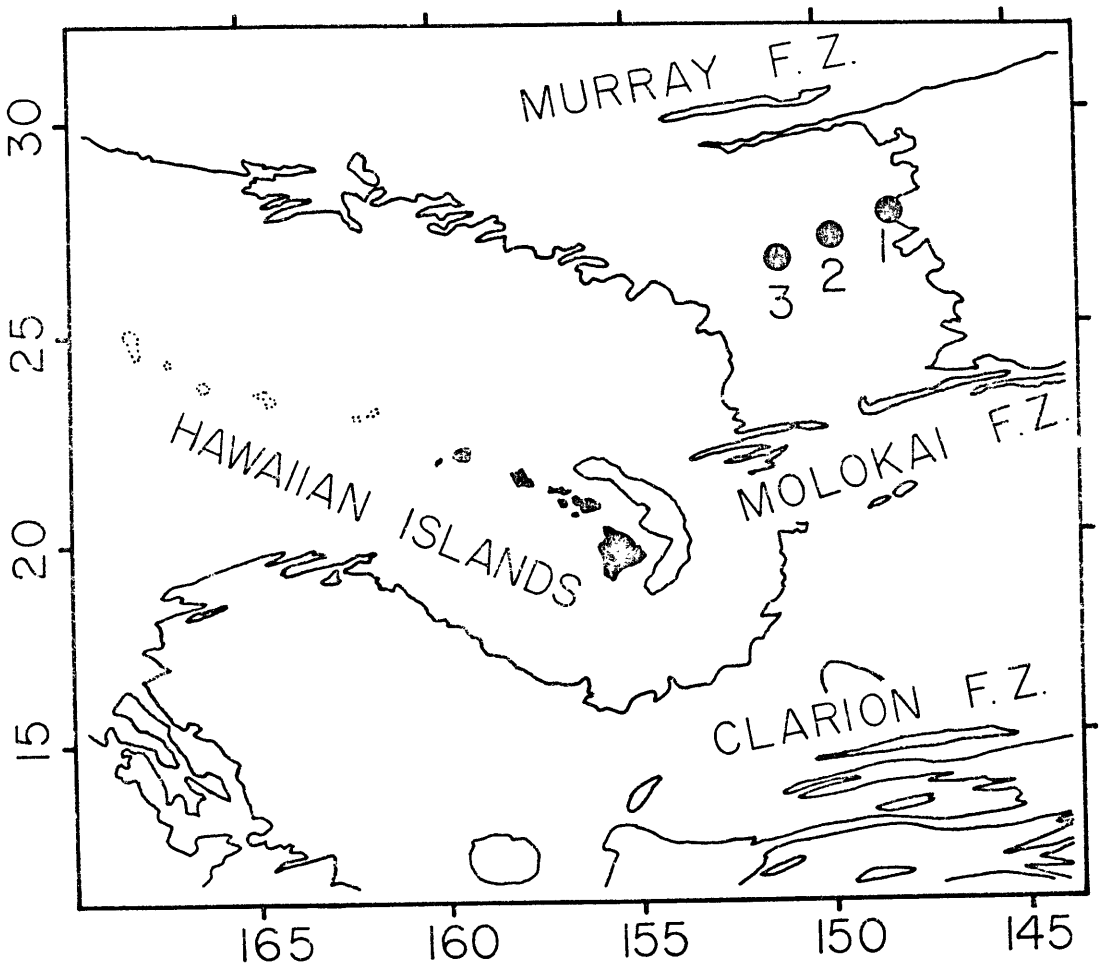
MURRAY F.Z.
MOLOKAI F.Z.
CLARION F.Z.
HAWAIIAN ISLANDS
1
2
3
30
25
20
15
165
160
155
150
145

external magnetic field. Variations in the magnetic induction are recorded as changes in the frequency of a free running oscillator. Back-to-back sensors are combined to increase the signal-to-noise ratio and to decrease ambient temperature effects. The resulting data have a precision of ±0.1 nT (1 nT = 1 gamma = $10^{-9}$T), although instrument noise limits the useful accuracy to about ±0.5 nT at short periods. Data values were recorded every 64 seconds on magnetic cassettes with timing controlled by a temperature compensated quartz crystal oscillator of negligible drift. Details of the calibration procedure and performance are reported in Poehls (1975).

The electric field data were recorded with a short span instrument identical to that used in the MODE experiment (Cox et al., 1980). This device utilizes a water chopper to reverse the electrode polarity every 16 seconds and minimize contamination of the signal by electrode drift (Filloux, 1973, 1974). Data values were recorded nominally every 32 seconds on magnetic tape.

## 2.2 THE TIME SERIES

The raw data were scaled to give electomagnetic field values and rotated to geomagnetic coordinates with $E_x$ and H to the magnetic north, $E_y$ and D to the magnetic east, and Z pointing down. The rotation direction was determined using a film recording compass-inclinometer with a precision of ±5°. The data were plotted and wild points were corrected by removal and linear interpolation across the resulting gap. Only random, isolated bad points of unknown origin ocurred in the magnetic field data set. A few longer gaps of about fifteen minutes duration appeared in the electric field data. In either case the total interpolated sections constitute less than 0.5% of the final time series.

No long term drift was apparent in the electric field data and no treatment was applied. The magnetic field data was contaminated by a large (greater than 300 nT), long term drift of instrumental origin. Polynomials were fit to the entire data set by least squares and removed to correct for this. The Chebyshev expansion was used as it results in a better conditioned set of normal equations and more rapid convergence than ordinary polynomial forms. We found that a seventh

order polynomial sufficed to correct H while eigth order was necessary for D and Z.

Because of more accurate internal clocks for the magnetometer instrumentation it was used as a reference for the electric field measurements. The start time for the electric field was determined by maximizing the coherence and minimizing the frequency derivative of the phase of the cross spectrum at the shortest periods. The electric field data was interpolated to 64 second samples using a natural cubic spline function. The final time series appears as Figure 2.

## 3. THE ELECTROMAGNETIC FIELDS

### 3.1 THE FUNDAMENTAL EQUATIONS

The Maxwell equations constitute the fundamental basis for the study of electromagnetism in the oceans. At low frequencies below 1 Hz scale analysis can be applied to show that the quasi-static approximation is valid (Sanford, 1971):

$$\nabla \cdot \vec{D} = \rho \qquad (1)$$

$$\nabla \cdot \vec{B} = 0 \qquad (2)$$

$$\nabla \times \vec{E} = -\partial \vec{B}/\partial t \qquad (3)$$

$$\nabla \times \vec{B} = \mu \vec{J} \qquad (4)$$

where $\vec{D}$ is the electric displacement, $\rho$ is the free charge density, $\vec{B}$ is the magnetic induction, $\vec{E}$ is the electric field, $\mu$ is the magnetic permeability, and $\vec{J}$ is the electric current density. The pertinent constitutive relations that complete the fundamental equations are:

$$\vec{J} = \sigma( \vec{E} + \vec{v} \times \vec{F} ) \qquad (5)$$

$$\vec{D} = \varepsilon_o \kappa \vec{E} + \varepsilon_o (\kappa - 1) \vec{v} \times \vec{F} \qquad (6)$$

where $\sigma$ is the electrical conductivity, $\vec{v}$ is the medium velocity, $\vec{F}$ is the steady geomagnetic induction vector, $\varepsilon_o$ is the permittivity of free space, and $\kappa$ is the dielectric constant. The main approximation that has been made is the neglect of the displacement current in (4) with the consequence that the physical process is one of diffusion rather than wave propagation. This is possible because the phase speed of the electromagnetic disturbances on an ocean wide scale are much smaller than the velocity of light. The important experimental quantities in (1)-(6) are the electric field $\vec{E}$ (volts/m) and the

FIGURE 2

Final 36 day long time series used in this study. Note the dominance of the north electric ($E_x$) and east magnetic (D) fields by diurnal tides while the east electric ($E_y$) and north magnetic (H) fields are predominantly semidiurnal in form. Scales are shown in the figure.

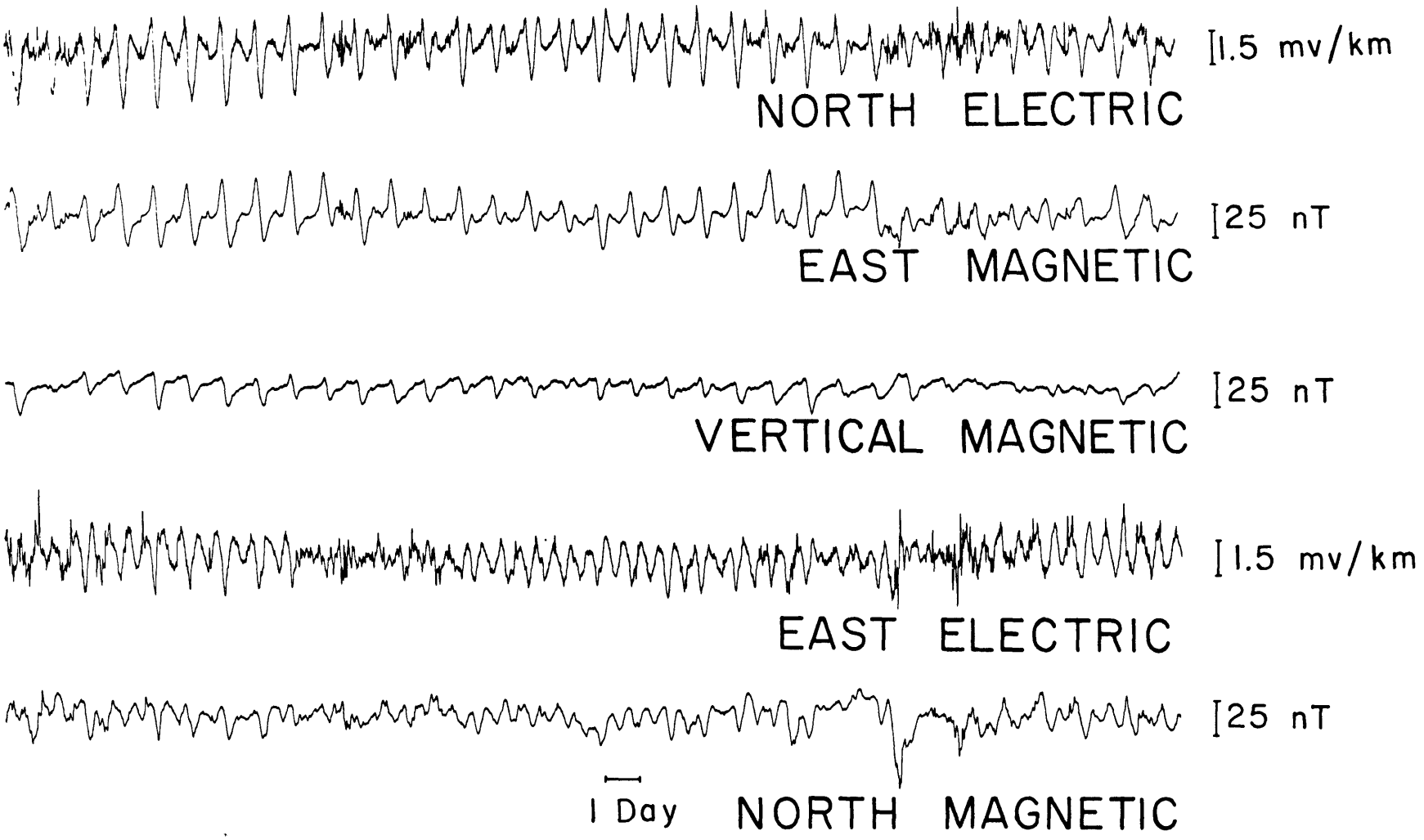
I1.5 mv/km
NORTH ELECTRIC
I25 nT
EAST MAGNETIC
I25 nT
VERTICAL MAGNETIC
I1.5 mv/km
EAST ELECTRIC
I25 nT
1 Day
NORTH MAGNETIC

magnetic induction $\vec{B}$ (Tesla).

The governing differential equation for magnetic induction is easily derived from (1)-(6):

$$\nabla^2\vec{B} - \mu\sigma\partial\vec{B}/\partial t = - \mu\nabla\sigma/\sigma \times \vec{J} - \mu\sigma( \vec{F}\cdot\nabla )\vec{v} \qquad (7)$$

If the conductivity gradient term and the source term for fluid motion on the right side of (7) are neglected this reduces to the familiar equation of magnetic induction by external sources:

$$\nabla^2\vec{B} - \mu\sigma\partial\vec{B}/\partial t = 0 \qquad (8)$$

Solutions of (8) on a flat earth can be divided into two types or modes: a B or TM mode and an E or TE mode. The TM mode has no vertical magnetic component and is characterized by electric current loops in the vertical plane. The TE mode has no vertical electric field and the currents flow in horizontal loops. For the TE mode coupling between layers can occur only by mutual induction.

## 3.2 SOURCE FIELDS

Electric currents in the earth are induced by sources external to it. In the oceans two driving forces are important: ionospheric current systems and oceanic motion fields. For the former only TE modes are considered due to the insulating atmosphere: vertical currents and electric fields are negligible. The simplest models approximate the ionospheric current systems as broad sources which are fixed in space but vary in magnitude with time, and hence the inducing fields are treated as plane waves. If the source fields are not broad then their dimensions will influence the induction and must be included in the analysis. Examples of small wavelength source fields include the equatorial and auroral electrojets. It is widely accepted that the plane wave approximation is valid over a wide frequency range at mid-latitudes. Since it greatly simplifies the analysis, we will assume that the zero wavenumber source field approximation is valid and re-examine the correctness of this treatment in a later section.

Solutions of (7) require a global knowledge of the velocity field. The velocity field must also satisfy the appropriate hydrodynamic equations. Since the water velocity field is rarely well understood various physical approximations must be made. Both TE and TM modes

can result from oceanic flows since the resulting electric currents are not constrained to flow in a horizontal plane. In general, steady two dimensional flows produce only TM modes while irrotational flows produce only TE modes. Mixed modes will result from more complex motions (Larsen, 1973). Baroclinic motions produce insignificant signals at the ocean bottom and only barotropic flows need be considered (Larsen, 1968).

Daniel (1978) has reviewed the potential sources of oceanic electromagnetic fields at the north Pacific site of this experiment. He found that the major water motion contributing to the deep ocean electromagnetic field is barotropic surface gravity waves. Tidal currents are the most important source of this signal and Daniel was able to use electric field data to estimate the deep ocean tidal velocity.

The tides can be removed from all data components via least squares fitting of sinusoids or notched out in the final frequency domain data analysis. We assume that the oceanic contributions to the electromagnetic field at periods outside the tidal line spectrum are negligible.

## 3.3 SEPARATION OF THE OCEANIC TIDES

Diurnal tides are prominent in both $E_x$ and D while semidiurnal and higher frequency variations dominate $E_y$ and H. These signals are of both ionospheric and oceanic origin. $M_2$, the lunar semidiurnal tide, is dominated by an oceanic generated part while the daily solar variation, $S_2$, is primarily ionospheric (Larsen, 1968). The ratio of $M_2$ to $S_2$ serves as a measure of the relative importance of the oceanic and ionospheric fields.

Sinusoids at the known tidal frequencies were fit to all of the time series by least squares using the technique of Larsen (1966). Table 1 lists the amplitudes and phases of the resulting Fourier series components and Figure 3 shows an example of the separation for the D magnetic component. Only those major periodicities that were resolvable within the classical limit of 1/T, where T is the length of the time series, were considered.

The $M_2/S_2$ ratio is near 1 for both H and $E_y$. This means that the semidiurnal signal in these components has a large oceanic part.

TABLE 1

TIDAL AMPLITUDES AND PHASE

| Tidal Line | | $Q_1$ | $O_1$ | $K_1$ | $M_2$ | $S_2$ | $S_3$ | $S_4$ | $S_5$ | $S_6$ |
|---|---|---|---|---|---|---|---|---|---|---|
| Period (hours) | | 26.8684 | 25.8103 | 23.9345 | 12.4206 | 12.0000 | 8.0000 | 6.0000 | 4.8000 | 4.0000 |
| $E_x$ | mv/km | .052 | .038 | .32 | .22 | .61 | .38 | .14 | .056 | .052 |
| | degrees | 62.8 | 289.7 | 45.9 | 25.1 | 348.7 | 35.4 | 93.9 | 230.7 | 301.4 |
| $E_y$ | mv/km | .021 | .030 | .075 | .41 | .43 | .13 | .058 | .017 | .028 |
| | degrees | 347.3 | 34.8 | 87.3 | 136.7 | 90.5 | 142.2 | 213.2 | 315.3 | 91.5 |
| H | nT | ----- | ----- | 1.24 | 2.94 | 4.37 | 1.00 | .31 | .11 | ----- |
| | degrees | ----- | ----- | 68.4 | 97.9 | 107.1 | 98.7 | 148.2 | 175.4 | ----- |
| D | nT | .83 | 1.63 | 7.91 | 1.11 | 7.61 | 3.71 | 1.08 | .32 | .34 |
| | degrees | 353.7 | 209.1 | 321.5 | 37.7 | 272.7 | 320.8 | 22.5 | 153.9 | 229.2 |
| Z | nT | ----- | ----- | 4.01 | .88 | 2.24 | 1.50 | .59 | ----- | ----- |
| | degrees | ----- | ----- | 22.5 | 157.5 | 331.2 | 12.4 | 76.0 | ----- | ----- |

All phases relative to 0000Z 1 January 1976

FIGURE 3

Separation of the five tidal lines from the east magnetic field component by least squares fitting of sinusoids. The data less tides is dominated by high frequency signals, especially bay disturbances with periods of several hours.

ORIGINAL DATA

20 nT

$K_1 + M_2 + S_2 + S_3 + S_4$

DATA less TIDES

The $M_2/S_2$ ratio for D and $E_x$ is much smaller, suggesting that the source for these components is largely ionospheric. Power spectra for all of the time series were computed and smoothed by band averaging with twenty degrees of freedom per estimate (Figures 4 and 5). The separated tidal signal is shown by the solid dots. According to Fisher (1929) a deterministic signal must exceed the background by a factor of 2.1 to be significant at the 95% level. By this criterion $K_1$, $S_2$, $S_3$, and $S_4$ are important in $E_x$ and D while only $M_2$, $S_2$, and $S_3$ are significant in $E_y$ and H.

## 4. RESPONSE FUNCTIONS

The solutions of (8) are usually given as the E over B response functions or impedances. The desired response functions are expressed as the members of a tensor relating E and B:

$$\begin{aligned} \tilde{E}_x &= Z_{xx}\tilde{H} + Z_{xy}\tilde{D} \\ \tilde{E}_y &= Z_{yx}\tilde{H} + Z_{yy}\tilde{D} \end{aligned} \qquad (9)$$

where each of the variables is a function of frequency $\omega$ and source field wavenumber k. The symbol $\sim$ denotes the Fourier transform. The response tensor $Z_{ij}$ contains information on the electrical conductivity of the earth, the characteristics of the source fields, and the dynamics of the ocean.

A related quantity to the response functions is the inductive scale length:

$$C(\omega,k) = iZ(\omega,k)/\omega \qquad (10)$$

It can be shown from (1)-(4) that the modulus of C is the depth to the top of a substitute horizontal perfect conductor that will produce a given response. Schmucker (1970b) has used convolution integrals to show that C is also a length scale that determines the horizontal and vertical extent of the region controlling the inductive response. This is an important concept in understanding the influence of both lateral conductivity changes and source field complications.

Since the relationship (9) is a tensor type, the response functions can be rotated to a set of principal coordinates where $Z_{xy}$ and $Z_{yx}$ are maximized using a similarity transformation. The off-diagonal components are minimized simultaneously. In this set of coordinates one of $Z_{xy}$ or $Z_{yx}$ represents the most conductive direction while the

FIGURE 4

Smoothed power spectrum for the entire electric field data sets less tides with ten estimates per frequency band for twenty degrees of freedom per band. The 95% confidence limit, calculated from the $\chi$-squared property of the autopower, is shown. The solid circles are the power levels of the deterministic tidal signals which must exceed the background by a factor of 2.1 to be significant at the 95% level (Fisher, 1929).

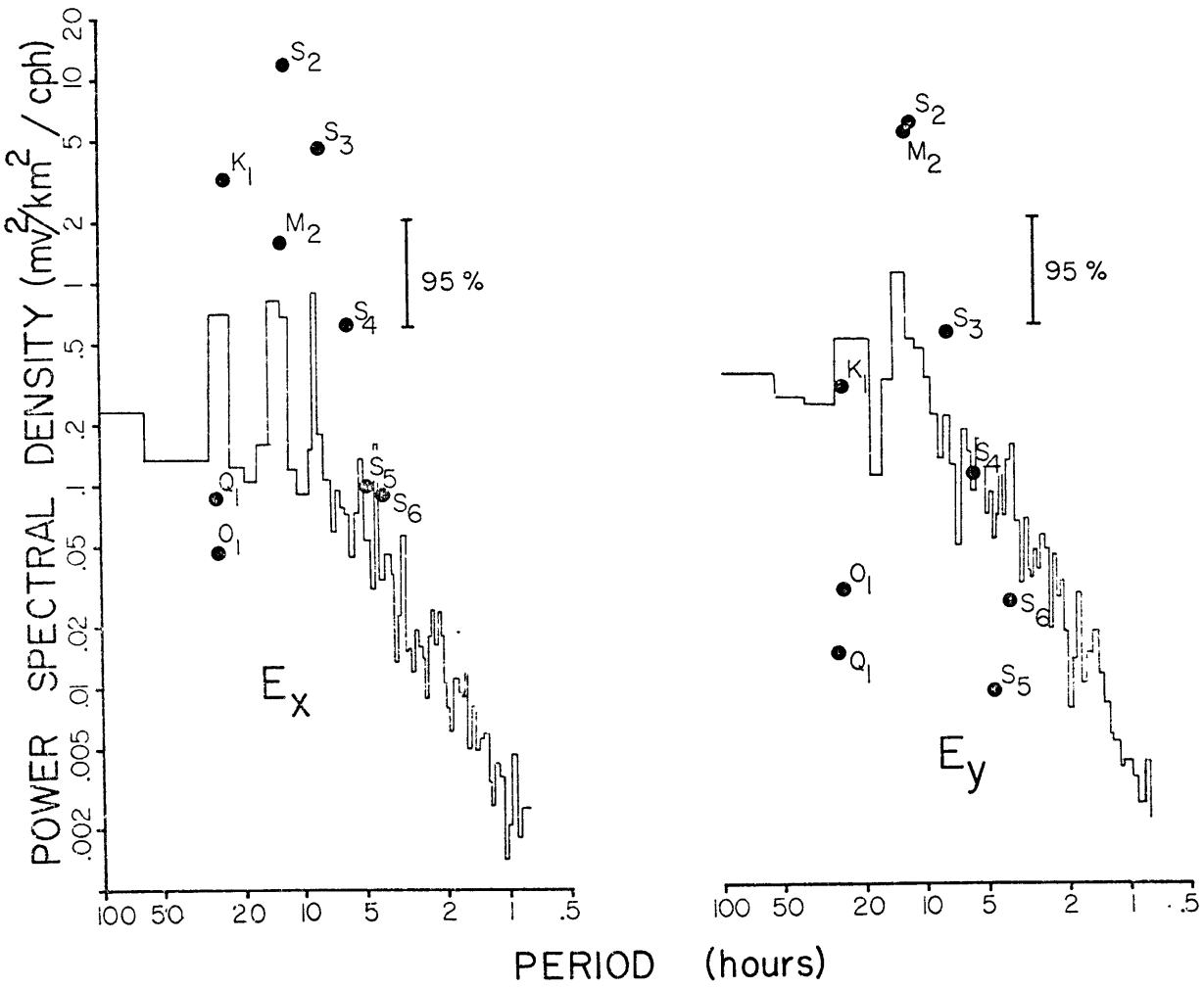
POWER SPECTRAL DENSITY (mv²/km²/cph)
.002 .005 .01 .02 .05 .1 .2 .5 1 2 5 10 20
100 50 20 10 5 2 1 .5
PERIOD (hours)
S2
S3
K1
M2
S4
95 %
Q1
O1
S5
S6
Ex
Ey

FIGURE 5

Smoothed power spectra for the magnetic field data. See Figure 4 caption for details.

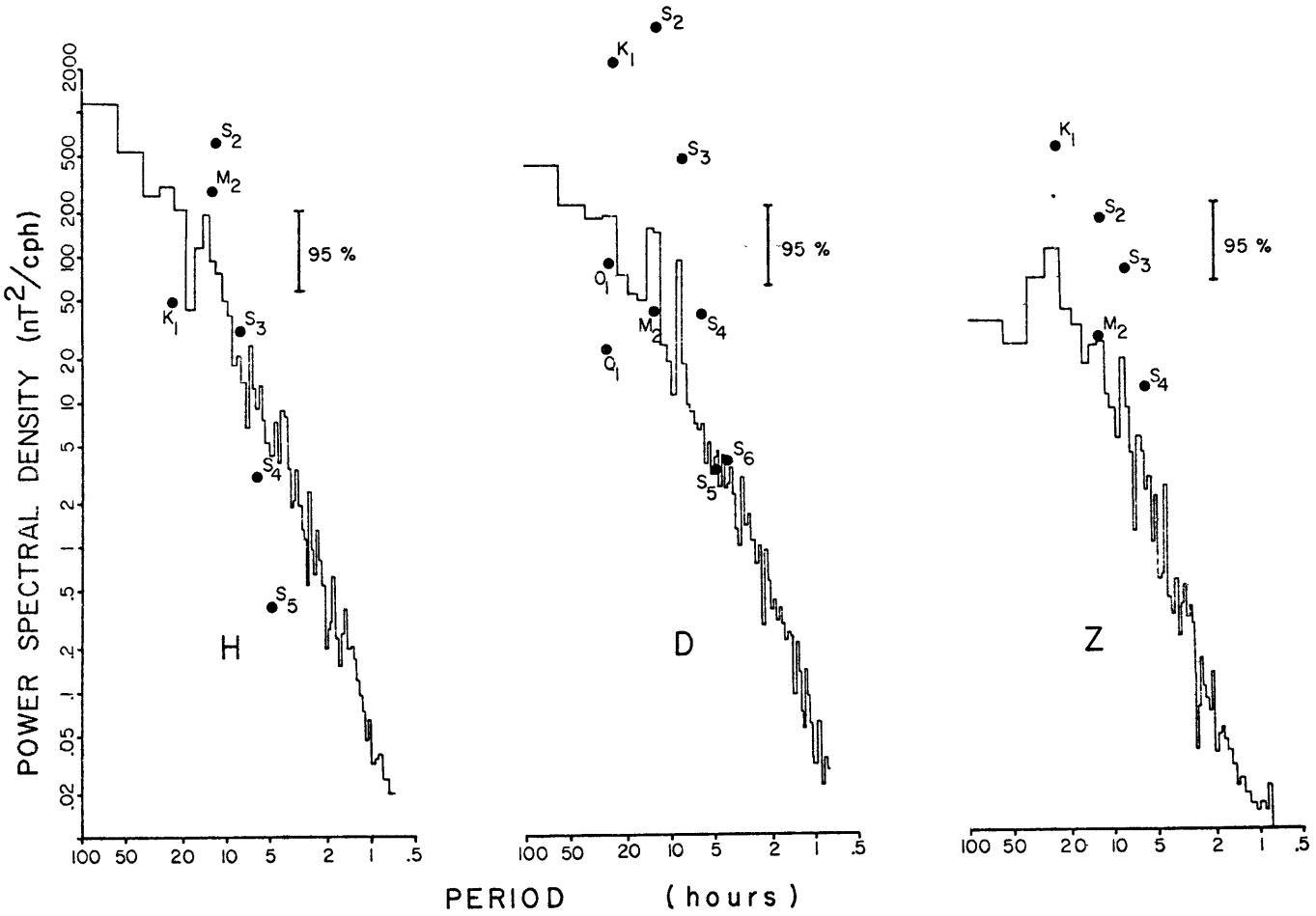
POWER SPECTRAL DENSITY (nT²/cph)
2000
500
200
100
50
20
10
5
2
1
.5
.2
.1
.05
.02
95 %
K1
S2
M2
S3
S4
S5
H
Q1
S6
D
Z
100 50 20 10 5 2 1 .5
PERIOD (hours)

other indicates the least conductive coordinate.

In order to calculate the response functions, all of the final time series were transformed in whole into the frequency domain. The leakage effect of the finite length of the data set was minimized by frequency domain convolution with a Goodman-Enochson-Otnes window (Otnes and Enochson, 1972). This spectral window reduces long distance leakage in a manner inversely proportional to frequency to the fourth power while minimizing the loss of degrees of freedom in the data.

We have applied two techniques to the calculation of response functions: the standard least squares transfer function technique and singular value decomposition (SVD) of the data matrix. The latter is a technique suggested by Jupp (1978) that minimizes some of the problems in ordinary least squares analysis, especially the ill-conditioning of the normal equations by the sometimes high inter-variable correlations that occur in electromagnetic data. It also allows a detailed analysis of the noise structure of the data to be made. Since it may be unfamiliar to some readers, we will describe the theory in some detail before applying it.

## 4.1 SINGULAR VALUE DECOMPOSITION

We define an M by N data matrix $\underline{\underline{D}}$ which we wish to separate into a signal matrix $\underline{\underline{S}}$ and a noise matrix $\underline{\underline{E}}$ such that $\underline{\underline{D}} = \underline{\underline{S}} + \underline{\underline{E}}$. For magnetotelluric data in the frequency domain with spectral smoothing by averaging over frequency bands M, the number of rows in $\underline{\underline{D}}$, corresponds to the frequencies within a given band while N, the number of columns in $\underline{\underline{D}}$, corresponds to the different data variables ($E_x$, $E_y$, H, D, and Z). The analysis is conducted separately for each band. The signal matrix $\underline{\underline{S}}$ has a rank r, less than or equal to N, that is to be determined both from the physics and from the noise structure of the data. $\underline{\underline{S}}$ will consist of the correlated or noise-free portion of the data while $\underline{\underline{E}}$ is the residual noise.

For a general M by N matrix the following holds (Lanczos, 1961):

$$\underline{\underline{D}} = \underline{\underline{U}}\ \underline{\underline{\Sigma}}\ \underline{\underline{V}}^H \qquad (11)$$

where $\underline{\underline{U}}$ is the M by M orthonormalized eigenvector matrix for $\underline{\underline{D}}\underline{\underline{D}}^H$, $\underline{\underline{V}}$ is the N by N orthonormalized eigenvector matrix for $\underline{\underline{D}}^H\underline{\underline{D}}$, and $\underline{\underline{V}}^H$ is the

Hermitian conjugate of $\underline{\underline{V}}$. $\Sigma$ is an M by N matrix with only N nonzero diagonal elements. The entries $\sigma_i$ are the positive square roots of the eigenvalues of $\underline{\underline{D}}\underline{\underline{D}}^H$ and $\underline{\underline{D}}^H\underline{\underline{D}}$. They are arranged in order of decreasing size.

Application of the SVD to physical data requires some pre-processing to equalize the error variance in each component. Ideally, this is accomplished by weighting each component by its signal-to-noise ratio. In practice, the error variance is unknown and we equalize the total variance per component. For our analysis we set the variance in each column of $\underline{\underline{D}}$ to unity for each frequency band examined. This removes the effect of inadvertent weighting caused by the different units of measurement of electric and magnetic fields.

The SVD posesses an important property: if the rank of $\underline{\underline{D}}$ is $r \leq N$ only the first r diagonal elements of $\underline{\underline{\Sigma}}$ are significant. The Eckart-Young Theorem (Jupp, 1978) states that the matrix of rank r that best minimizes the Euclidean distance (i.e., the square root of the squared differences) $||\underline{\underline{D}} - \underline{\underline{S}}||$ is the SVD of $\underline{\underline{D}}$ with only r entries in $\underline{\underline{\Sigma}}$ nonzero. This means that the signal matrix is found by zeroing the eigenvalues of $\underline{\underline{D}}$ from r + 1 to N and re-forming (11). The problem then reduces to estimating r.

The rank of the signal matrix relates directly to the physics governing the induction process. It corresponds to the number of independent modes of variation in the data. If the zero wavenumber approximation for the source field holds and the conductive structure is two dimensional we expect the two principal directions in (9) to dominate the off-diagonal terms and a rank of two for $\underline{\underline{S}}$. If the Z variations are important and correlated with the horizontal magnetic field an additional degree of freedom exists in the data set and the rank is three. This is indicative of source field complications or three dimensional conductive structure.

The rank of the signal matrix is determined by analysis of the eigenvalues in $\underline{\underline{\Sigma}}$ and the eigenvectors in $\underline{\underline{V}}$. The submatrix $\underline{\underline{S}}$ is assumed to be a least squares estimator for $\underline{\underline{D}}$ and an estimator for the signal variance or power is $\sum^{r} \sigma_i^2$. A similar estimator for the noise variance is available. If both of these quantities are weighted by the appropriate number of statistical degrees of freedom and the

variance is assumed to be normally distributed then the ratio of variance follows an F-distribution (Sokal and Rohlf, 1969).

A measure of the total signal variance to noise variance ratio is:

$$R = (N-r) \sum_{1}^{r} \sigma_i^2 / \; r \sum_{r+1}^{N} \sigma_i^2 \qquad (12)$$

where the variance ratio has been weighted by the number of degrees of freedom. A criterion is needed to either accept or reject data as R is large or small. Jupp (1978) suggests a signal-to-noise ratio of 4 : 1. We prefer the more direct approach of assessing R as an F-distributed ratio of variance at an appropriate confidence level. In either case increasing r beyond some point will result in no significant improvement in R, fixing r.

The difficulty with (12) is that no way of evaluating the separate components exists. This means that a noisy component could influence the result in a derogatory fashion. A partial signal-to-noise variance ratio estimate allows examination of the noise structure by component. This is accomplished by weighting (12) by the data eigenvectors in $\underline{\underline{V}}$:

$$R_j = (N-r) \sum_{1}^{r} \sigma_i^2 |V_{ij}|^2 / r \sum_{r+1}^{N} \sigma_i^2 |V_{ij}|^2 \qquad (13)$$

where the subscript j refers to the j-th component. This variable also follows an F-distribution and can be evaluated in a manner similar to (12).

## 4.2 NOISE STRUCTURE OF THE DATA

A band averaging scheme was chosen that isolated the $K_1$, $S_2 + M_2$, $S_3$, $S_4$, $S_5$, and $S_6$ tidal lines in narrow frequency bands while yielding sufficient estimates in each signal band for statistical reliability. The analysis was done for both the original data and for the data with the tides removed. No difference was observed outside of the narrow tidal bands.

Figure 6 shows the composite signal-to-noise variance ratio as a function of signal matrix rank calculated using (12) with all five data components. The horizontal lines are 90% confidence levels calculated from the F-distribution for the appropriate number of degrees of freedom. A rank 1 signal matrix is inadequate at all save

FIGURE 6

Composite signal-to-noise variance or power ratio as a function of data matrix rank calculated using (12) for all five data components. The horizontal lines are the 90% confidence levels for each case calculated using the critical values of the F-distribution for the appropriate number of degrees of freedom.

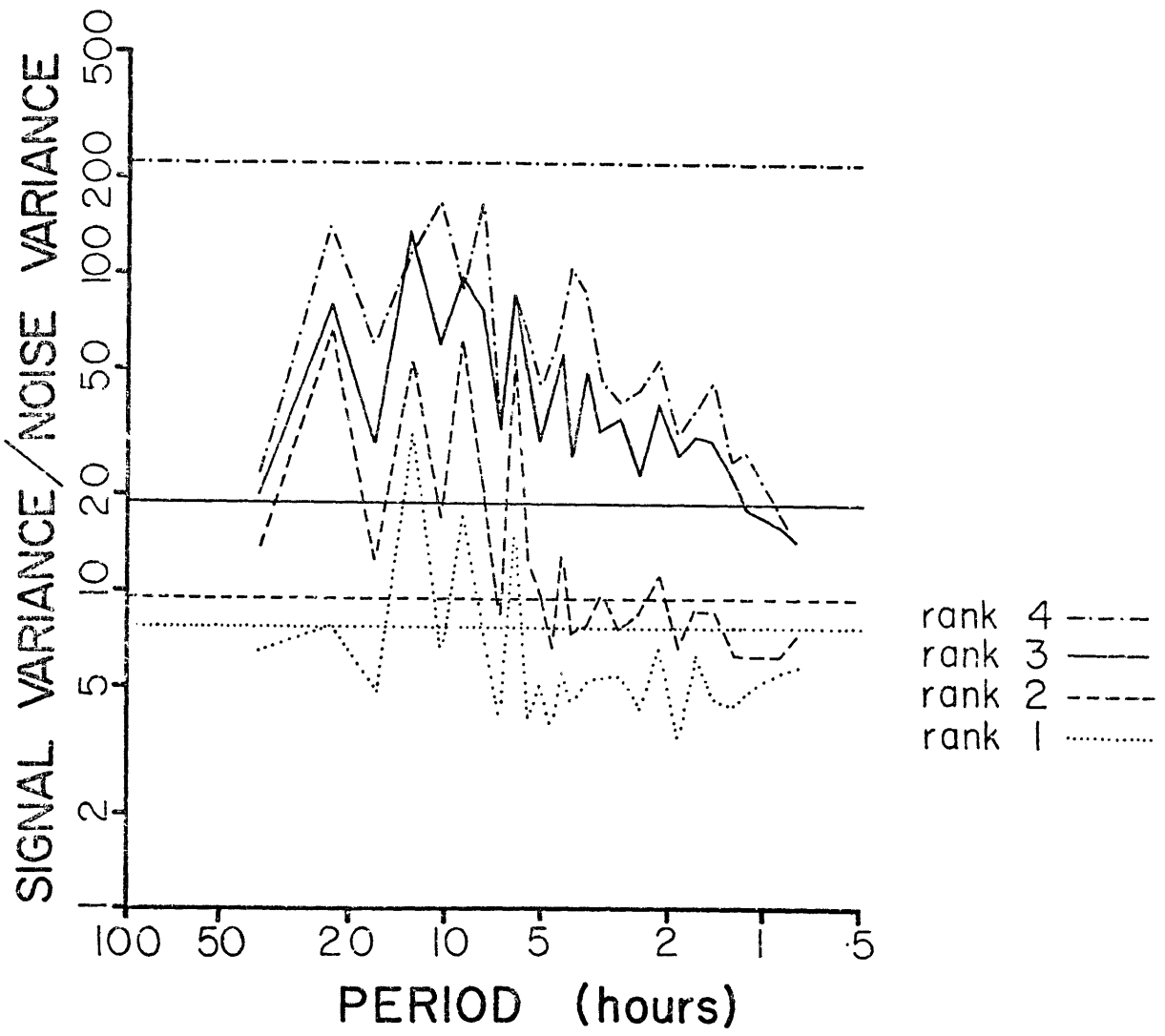
SIGNAL VARIANCE/NOISE VARIANCE
500
200
100
50
20
10
5
2
1
100
50
20
10
5
2
1
.5
PERIOD (hours)
rank 4
rank 3
rank 2
rank 1

tidal periods. At periods below 5 hours the rank 2 case is not significant at the 90% level. The rank 3 signal matrix is a good choice at all periods longer than 1 hour while 4 degrees of freedom is inadequate at any period. This suggests that there are three degrees of freedom in the data.

Figures 7 and 8 show the rank 2 and 3 signal-to-noise variance ratios using (13) along with the 90% and 95% confidence levels from the F-distribution. $E_y$ and H are considerably less noisy than $E_x$ and D at most periods. The D component is especially noisy for the rank 2 case below 8 hours. Addition of a third degree of freedom results in an improvement in D with a slight degradation of $E_x$. The Z signal level rises markedly, especially at the semidiurnal tidal period and below 5 hours.

The SVD analysis suggests that the Z variations are a prominent feature of the data set that are correlated with the horizontal magnetic field. This implies that some departure from ideality in the physics will require further examination. A change in this correlation at a period near 5 hours is also apparent. We will re-examine the relation of Z with the remaining data in a later section and proceed with the magnetotelluric analysis on the rank 2 signal matrix.

## 4.3 CALCULATION OF THE RESPONSE FUNCTIONS

The system of response functions (9) are an overdetermined set of equations in four unknowns with six measurements and can be solved in the least squares sense. Two choices of dependent of noise-free variables were considered for the least squares analysis: the horizontal electric and horizontal magnetic components taken together. We will refer to the first case as $Z^E$ and the second as $Z^B$. Uncertainties in the response functions were calculated using the results of Bentley (1973).

The SVD response functions for a rank 2 signal matrix were also obtained. Since the propagation of error in the SVD calculation is complex we used the average of the $Z^E$ and $Z^B$ uncertainties as an estimate of the error. The principal direction of the response tensor was found to be period independent from 1-18 hours. One of the principal response functions, $Z_{xy}$, strikes approximately $350^oT$,

FIGURE 7

Signal-to-noise variance or power ratio by data component for a rank 2 signal matrix calculated using (13). The 90% and 95% confidence levels from the critical values of the F-distribution are shown.

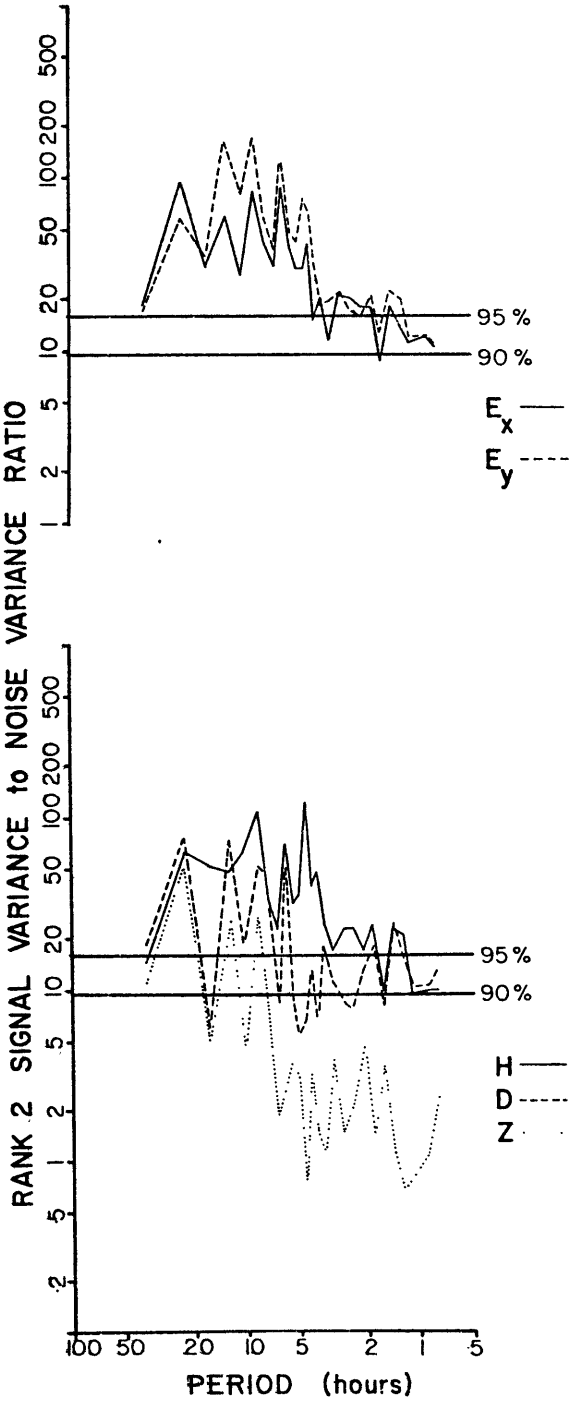
RANK 2 SIGNAL VARIANCE to NOISE VARIANCE RATIO
500
200
100
50
20
10
5
2
1
95 %
90 %
$E_x$
$E_y$
.5
.2
H
D
Z
100 50 20 10 5 2 1 .5
PERIOD (hours)

FIGURE 8

Signal-to-noise variance ratio by data component for a signal matrix of rank three. The 90% and 95% confidence levels from the critical values of the F-distribution are shown.

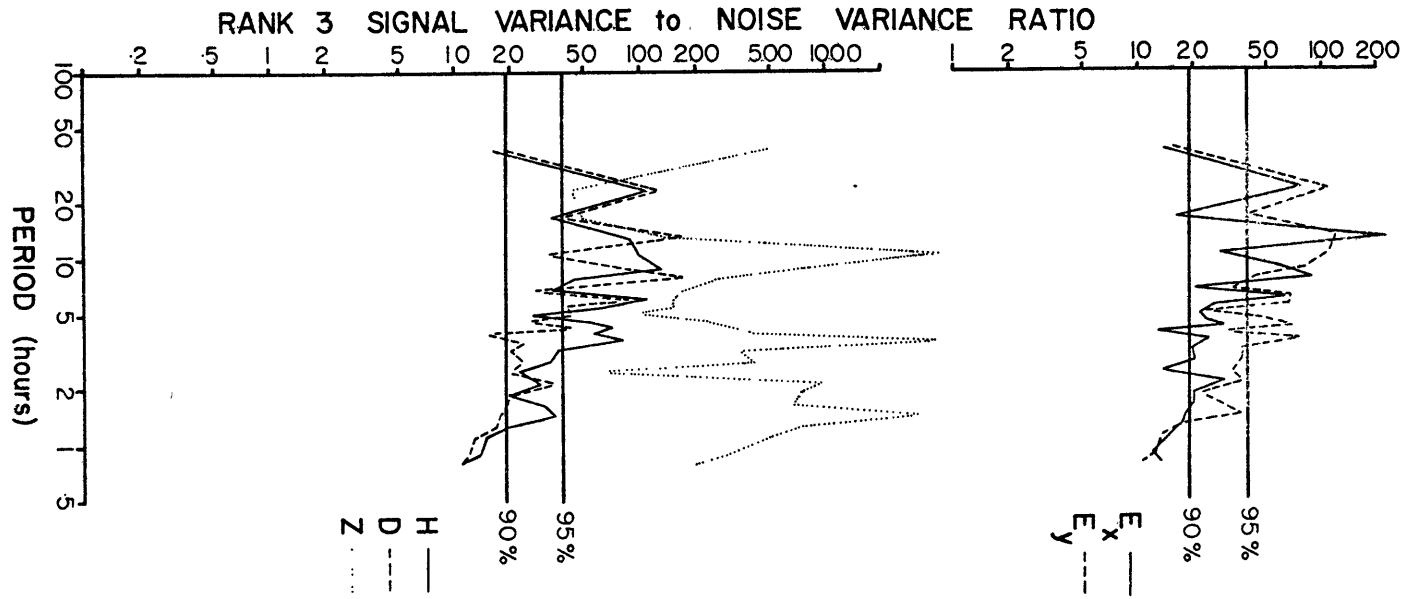
RANK 3 SIGNAL VARIANCE to NOISE VARIANCE RATIO
.2 .5 1 2 5 10 20 50 100 200 500 1000
1 2 5 10 20 50 100 200
PERIOD (hours)
100 50 20 10 5 2 1 .5
H
D
Z
90%
95%
Ex
Ey
90%
95%

with $Z_{yx}$ offset by $90^{o}$. Figure 9 shows the result for all three cases while Table 2 lists the response functions. For clarity error bars have been suppressed for $Z^{E}$ and $Z^{B}$. For graphical display the complex response functions are expressed as apparent resistivity and phase.

The SVD apparent resistivities lie between the $Z^{E}$ and $Z^{B}$ results, which is not surprising in view of the less extreme noise distribution assumptions made in the SVD analysis. The $Z^{B}$ result produces higher apparent resistivities, especially at short periods, while the $Z^{E}$ apparent resistivity is flat and small at periods less than 6 hours.

## 5. MANTLE CONDUCTIVITY PROFILES

To obtain a mantle conductivity profile we convert the frequency-response function information to get a conductivity-depth relation by standard inverse techniques. Response functions are usually interpreted in terms of a one dimensional structure where conductivity depends only on depth. There are certain physical constraints on the response functions that are necessary conditions for a one dimensional interpretation to be valid. Weidelt (1972) has presented twenty-two inequalities which the inductive scale length (10) must satisfy. Larsen (1980) has reformulated these in terms of the response functions (9) and included the effect of errors. Failure of the response functions to satisfy these inequalities is indicative of two or three dimensional conductive structure, source field polarization, or excessively noisy data.

The response function $Z_{xy}$ in Figure 9 does not satisfy the criteria of Larsen (1980) at most periods. Neither the apparent resistivities nor the phases are smooth and slowly varying. The data are very noisy below 5 hours period, probably due to the high noise level seen in Figure 7. The very rapid rise in apparent resistivity around 10 hours is physically unreasonable. No one dimensional interpretation of these data is possible.

The response function $Z_{yx}$ in Figure 9 does satisfy the one dimensionality conditions. The response curve is smooth with some residual bias in the phase near two and six hours, probably due to oceanic contamination. The rapid drop in apparent resistivity at long

FIGURE 9

Response functions for the two principal directions of the impedance tensor. $Z_{xy}$ (left side) is dominated by the north electric and east magnetic fields, while $Z_{yx}$ (right side) is governed by the east electric and north magnetic fields. The 95% confidence limits on the SVD response functions are shown. Solid dots are the $Z^B$ least squares response function and the open circles are the $Z^E$ case (see text).

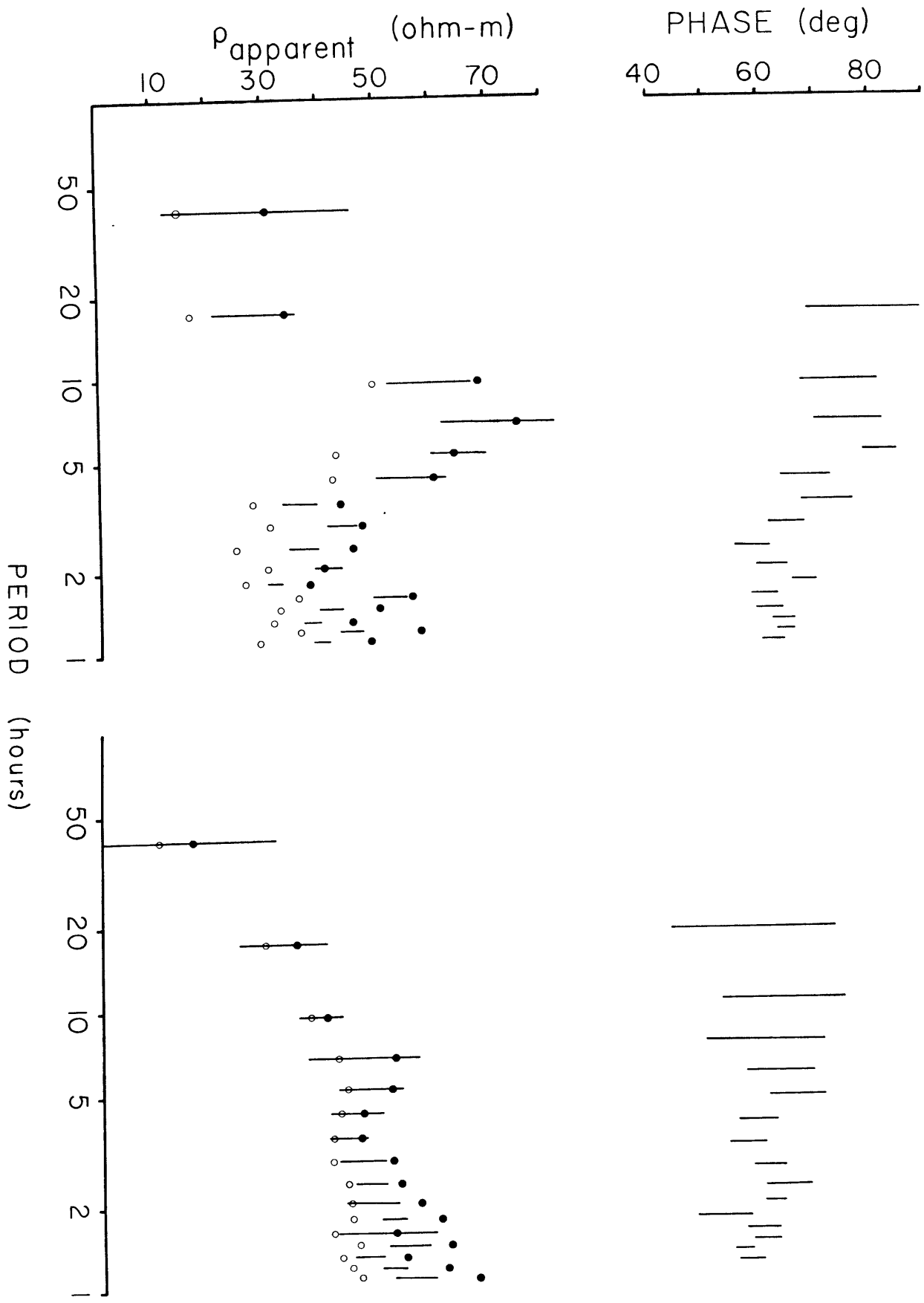
$\rho_{apparent}$ (ohm-m)
10
30
50
70
PHASE (deg)
40
60
80
PERIOD (hours)
50
20
10
5
2
1
50
20
10
5
2
1

TABLE 2-A

SVD RESPONSE FUNCTIONS

| Period (hr) | D.F. | $Z_{xy}$ Modulus | ±95% | Phase | ±95% | $Z_{yx}$ Modulus | ± 95% | Phase | ±95% |
|---|---|---|---|---|---|---|---|---|---|
| 40.9 | 52 | 0.0315 | 0.0127 | 91.3 | 67.8 | 0.0217 | 0.0139 | 60.6 | 60.4 |
| 17.4 | 62 | 0.0474 | 0.0081 | 79.4 | 14.5 | 0.0512 | 0.0059 | 59.6 | 15.0 |
| 9.59 | 76 | 0.0933 | 0.0080 | 75.3 | 9.6 | 0.0753 | 0.0037 | 65.1 | 11.2 |
| 6.85 | 78 | 0.1209 | 0.0117 | 76.6 | 8.8 | 0.0977 | 0.0105 | 61.6 | 10.7 |
| 5.32 | 78 | 0.1302 | 0.0069 | 82.3 | 3.9 | 0.1123 | 0.0066 | 64.4 | 5.9 |
| 4.36 | 76 | 0.1344 | 0.0098 | 69.0 | 6.7 | 0.1206 | 0.0061 | 67.1 | 5.5 |
| 3.57 | 120 | 0.1190 | 0.0070 | 73.1 | 6.6 | 0.1311 | 0.0049 | 60.4 | 3.5 |
| 2.94 | 160 | 0.1443 | 0.0063 | 65.6 | 4.5 | 0.1496 | 0.0055 | 58.4 | 3.3 |
| **2.45** | **160** | **0.1454** | **0.0065** | **59.5** | 4.0 | **0.1656** | **0.0046** | **62.4** | **2.7** |
| 2.09 | 160 | 0.1659 | 0.0072 | 63.3 | 3.8 | 0.1793 | 0.0084 | 65.9 | 4.0 |
| 1.83 | 160 | 0.1555 | 0.0046 | 69.0 | 2.8 | 0.1990 | 0.0040 | 63.5 | 1.7 |
| 1.63 | 160 | 0.2119 | 0.0078 | 61.8 | 3.1 | 0.2091 | 0.0174 | 54.3 | 4.9 |
| 1.46 | 160 | 0.2003 | 0.0068 | 62.7 | 3.2 | 0.2283 | 0.0075 | 61.4 | 2.8 |
| 1.33 | 160 | 0.2012 | 0.0053 | 65.3 | 2.5 | 0.2234 | 0.0058 | 62.0 | 2.2 |
| 1.22 | 160 | 0.2276 | 0.0061 | 65.7 | 2.1 | 0.2438 | 0.0050 | 57.8 | 1.5 |
| 1.12 | 160 | 0.2228 | 0.0062 | 63.5 | 2.7 | 0.2632 | 0.0086 | 59.2 | 2.3 |
| 1.04 | 160 | 0.2025 | 0.0059 | 64.0 | 2.2 | 0.2714 | 0.0062 | 66.7 | 1.6 |

TABLE 2-B

$Z^B$ RESPONSE FUNCTIONS

| | | $Z_{xy}$ | | | | $Z_{yx}$ | | | |
|---|---|---|---|---|---|---|---|---|---|
| Period (hr) | D.F. | Modulus | ±95% | Phase | ±95% | Modulus | ±95% | Phase | ±95% |
| 40.9 | 52 | 0.0225 | 0.0047 | 88.0 | 12.1 | 0.0190 | 0.0035 | 66.4 | 10.6 |
| 17.4 | 62 | 0.0372 | 0.0062 | 78.8 | 9.5 | 0.0485 | 0.0039 | 67.3 | 4.6 |
| 9.59 | 76 | 0.0848 | 0.0084 | 75.0 | 5.7 | 0.0739 | 0.0035 | 65.1 | 2.7 |
| 6.85 | 78 | 0.1137 | 0.0085 | 75.5 | 4.3 | 0.0927 | 0.0080 | 62.2 | 4.9 |
| 5.32 | 78 | 0.1060 | 0.0139 | 80.1 | 7.5 | 0.1073 | 0.0078 | 64.3 | 4.2 |
| 4.36 | 76 | 0.1161 | 0.0124 | 67.6 | 6.1 | 0.1169 | 0.0062 | 67.3 | 3.1 |
| 3.57 | 120 | 0.1044 | 0.0097 | 70.9 | 5.3 | 0.1271 | 0.0056 | 60.1 | 2.5 |
| 2.94 | 160 | 0.1212 | 0.0096 | 65.6 | 4.5 | 0.1402 | 0.0078 | 60.0 | 3.2 |
| 2.45 | 160 | 0.1196 | 0.0118 | 61.3 | 5.6 | 0.1586 | 0.0083 | 62.0 | 3.0 |
| 2.09 | 160 | 0.1422 | 0.0095 | 62.7 | 3.8 | 0.1724 | 0.0104 | 66.1 | 3.5 |
| 1.83 | 160 | 0.1419 | 0.0103 | 68.4 | 4.2 | 0.1846 | 0.0120 | 63.2 | 3.7 |
| 1.63 | 160 | 0.1754 | 0.0143 | 64.0 | 4.7 | 0.1883 | 0.0114 | 60.1 | 3.5 |
| 1.46 | 160 | 0.1766 | 0.0136 | 63.5 | 4.4 | 0.2094 | 0.0132 | 60.7 | 3.6 |
| 1.33 | 160 | 0.1817 | 0.0133 | 65.5 | 4.2 | 0.2122 | 0.0123 | 61.4 | 3.3 |
| 1.22 | 160 | 0.2037 | 0.0169 | 66.0 | 4.8 | 0.2263 | 0.0152 | 57.6 | 3.8 |
| 1.12 | 160 | 0.1892 | 0.0171 | 62.4 | 5.2 | 0.2392 | 0.0185 | 62.3 | 4.4 |
| 1.04 | 160 | 0.2140 | 0.0169 | 63.7 | 4.5 | 0.2291 | 0.0237 | 66.7 | 5.9 |

TABLE 2-C

$Z^E$ RESPONSE FUNCTIONS

| | | $Z_{xy}$ | | | | $Z_{yx}$ | | | |
|---|---|---|---|---|---|---|---|---|---|
| Period (hr) | D.F. | Modulus | ±95% | Phase | ±95% | Modulus | ±95% | Phase | ±95% |
| 40.9 | 52 | 0.0324 | 0.0104 | 87.3 | 18.2 | 0.0238 | 0.0071 | 68.6 | 15.3 |
| 17.4 | 62 | 0.0522 | 0.0030 | 78.9 | 2.7 | 0.0534 | 0.0036 | 67.5 | 3.4 |
| 9.59 | 76 | 0.0997 | 0.0075 | 75.0 | 3.6 | 0.0765 | 0.0039 | 65.2 | 2.5 |
| 6.85 | 78 | 0.1236 | 0.0115 | 75.6 | 4.6 | 0.1033 | 0.0063 | 62.2 | 3.0 |
| 5.32 | 78 | 0.1394 | 0.0074 | 80.2 | 2.5 | 0.1168 | 0.0061 | 64.1 | 2.6 |
| 4.36 | 76 | 0.1389 | 0.0085 | 67.6 | 3.0 | 0.1223 | 0.0060 | 67.3 | 2.3 |
| 3.57 | 120 | 0.1306 | 0.0061 | 70.9 | 2.5 | 0.1345 | 0.0033 | 60.4 | 1.4 |
| 2.94 | 160 | 0.1498 | 0.0040 | 65.7 | 1.5 | 0.1569 | 0.0036 | 59.9 | 1.4 |
| 2.45 | 160 | 0.1619 | 0.0038 | 61.1 | 1.3 | 0.2148 | 0.0046 | 63.2 | 1.1 |
| 2.09 | 160 | 0.1644 | 0.0040 | 63.3 | 1.5 | 0.1948 | 0.0077 | 66.1 | 2.3 |
| 1.83 | 160 | 0.1704 | 0.0044 | 68.2 | 1.3 | 0.2148 | 0.0046 | 63.2 | 1.1 |
| 1.63 | 160 | 0.2200 | 0.0043 | 64.2 | 1.1 | 0.2115 | 0.0098 | 60.3 | 2.7 |
| 1.46 | 160 | 0.2188 | 0.0047 | 62.7 | 1.3 | 0.2432 | 0.0077 | 61.8 | 1.8 |
| 1.33 | 160 | 0.2186 | 0.0042 | 65.6 | 1.0 | 0.2390 | 0.0067 | 61.4 | 1.5 |
| 1.22 | 160 | 0.2575 | 0.0063 | 65.8 | 1.3 | 0.2656 | 0.0057 | 57.6 | 1.2 |
| 1.12 | 160 | 0.2460 | 0.0047 | 63.6 | 1.0 | 0.2890 | 0.0109 | 60.9 | 2.1 |
| 1.04 | 160 | 0.2629 | 0.0054 | 64.3 | 1.1 | 0.3215 | 0.0102 | 66.8 | 1.6 |

periods as well as the constant $60^{o}$ phase suggest a general increase in conductivity at depth. The flattening and slight drop in apparent resistivity near five hours with the increase at shorter periods are suggestive of a higher conductivity layer sandwiched between lower conductivity zones, although an alternate explanation as a source field effect is possible. Whether any of these features are resolvable is not clear from the figure, and a formal inversion of the data is necessary.

## 5.1 INVERSION

The solutions of the induction equation (9) can be expressed in terms of non-dimensional functions $g_n$ that are determined recursively from the layered structure of the earth model (Schmucker, 1971):

$$g_n = ( \gamma_n g_{n+1} + \gamma_{n+1} \tanh(\gamma_n d_n) ) / ( \gamma_{n+1} + \gamma_n g_{n+1} \tanh(\gamma_n d_n) ) \qquad (14)$$

where the index n refers to one of the N layers and d is the layer thickness. The induction parameter $\gamma$ is defined as:

$$\gamma_n = \sqrt{k^2 + i\mu\sigma_n\omega} \qquad (15)$$

where k = 0 for the zero wavenumber source field approximation. The response of the half space at the bottom of the model is given by $g_N = 1$ and the response at any higher point is easily found by repeated use of (14). At the top layer the dimensional response function Z is easily obtained:

$$Z = i\omega g_1/\gamma_1 \qquad (16)$$

The recurrence relation (14) solves the forward problem, but is nonlinear due to the hyperbolic term. To solve the inverse problem and find the conductive structure given the response function it is necessary to linearize it. We have adopted the algorithm of Larsen (1975) after slight modification. Larsen solves for the conductance (product of layer thickness and conductivity) with weighting to prevent thin, highly conducting layers from dominating the result. We have chosen to reduce the number of free parameters and fix the layer thickness. We then search many different layered structures for those which produce realistic conductivity structures.

Finding a model which simply fits the data is not sufficient: models exist which have many more features than the data can actually resolve but which produce similar response functions. The non-uniqueness

property of inverse problems allows a trade-off to be made between resolution of conductivity and resolution of layer thickness. We have adopted the Backus-Gilbert smoothing scheme of Larsen (1975) to account for the uncertainty in the response functions and treat the real and imagninary parts of the response function separately. A good conductivity model is defined as one which fits the data and produces spreads in the layer thickness similar to the thickness, spreads in the conductivity that are much smaller than the layer conductivity, and which are insensitive to the starting model chosen.

## 5.2 CONDUCTIVITY STRUCTURE

The $Z^E$, $Z^B$, and SVD response curves for the $Z_{yx}$ direction were inverted separately using the formalism outlined above. In each case about one hundred starting layered models were tried. In no case were more than four layers and a half space required by the data. Attempts to increase the number of layers resulted in lack of resolution in all of the layers.

Figure 10 shows the three conductivity models for the three sets of response functions while Table 3 lists the results, including the spreads in the parameters. The structures for the three are similar, although the convergence properties were not. The SVD response functions were much easier to invert, requiring fewer iterations from a given starting model.

All of the models in Figure 10 include low conductivity near the surface. The inductive scale length at one hour is in excess of 100 km, suggesting that resolution is poor above this depth. This is reflected in the insensitivity of the model to large variations in the near surface structure. A rise in conductivity to 0.05 mho/m occurs at depths of 160-180 km for all of the response functions. A decrease below this, suggested by the data, is not resolvable. All of the models include a half space at depths near 400 km with a conductivity near that predicted by global induction studies.

Figure 11 compares the SVD result of this work to other conductivity models. The result of Filloux (1977) at station 3 is similar to ours near the surface, although the decrease in conductivity near 220 km is not resolved by our data. It must be noted that the

FIGURE 10

Layered conductivity structure obtained by inverting the $Z^B$ (short dotted line), $Z^E$ (long dotted line), and SVD (solid line) response functions. The error bars are the 95% confidence limits obtained from Backus-Gilbert smoothing with layer kernels similar to the layer thicknesses.

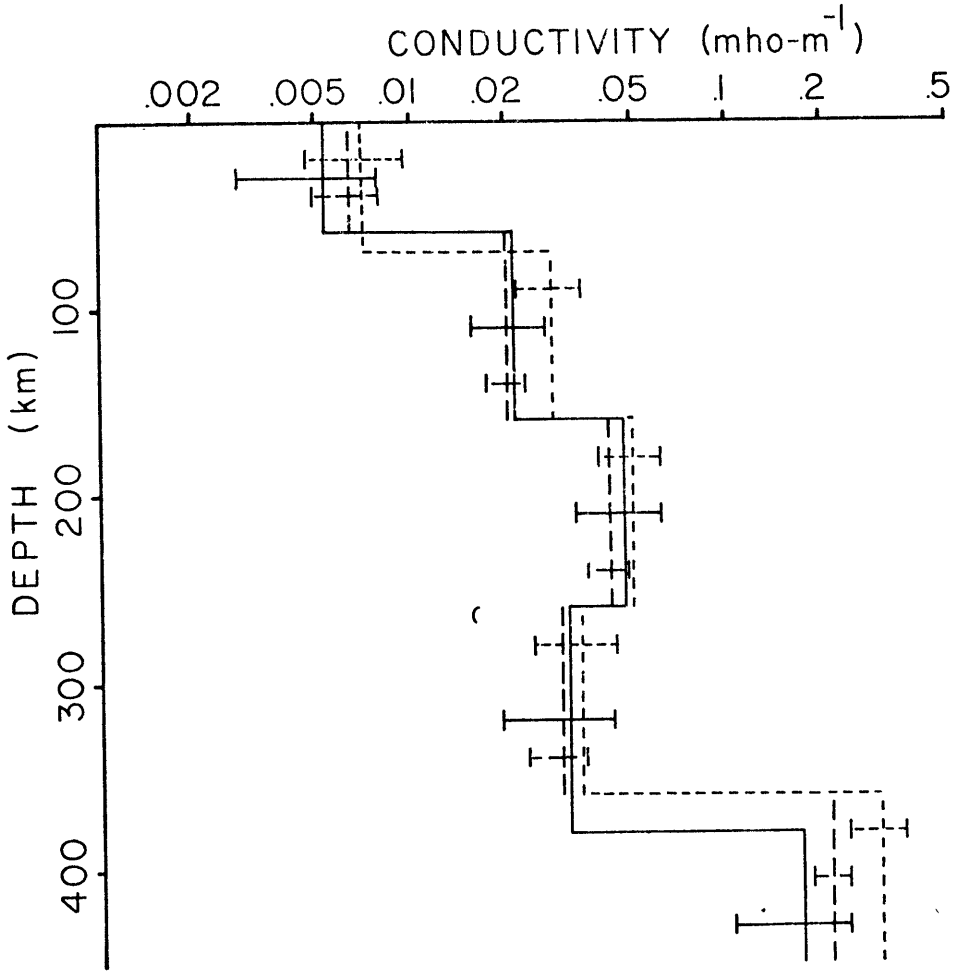
CONDUCTIVITY (mho-m$^{-1}$)
.002
.005
.01
.02
.05
.1
.2
.5
DEPTH (km)
100
200
300
400

TABLE 3

ELECTRICAL CONDUCTIVITY STRUCTURE

| Layer (km) | ±95% | Conductivity (mho/m) | ±95% |
|---|---|---|---|
| | | SVD | |
| 60 | 132 | 0.0053 | 0.0025 |
| 100 | 101 | 0.021 | 0.0055 |
| 100 | 105 | 0.047 | 0.014 |
| 120 | 122 | 0.031 | 0.012 |
| Halfspace | --- | 0.17 | 0.067 |
| | | $Z^B$ | |
| 70 | 83 | 0.0071 | 0.0024 |
| 90 | 96 | 0.028 | 0.0064 |
| 100 | 104 | 0.050 | 0.011 |
| 100 | 124 | 0.034 | 0.010 |
| Halfspace | --- | 0.20 | 0.058 |
| | | $Z^E$ | |
| 60 | 120 | 0.0064 | 0.0015 |
| 100 | 110 | 0.020 | 0.0027 |
| 100 | 104 | 0.042 | 0.0062 |
| 100 | 115 | 0.029 | 0.0060 |
| Halfspace | --- | 0.21 | 0.027 |

uncertainties given by Filloux indicate that the low conductivity layer in his model may not be real. The Hawaii result from Klein and Larsen (1978) is also similar to ours, the former with slightly higher conductivity at depths in excess of 200 km. The high conductivity zone at 400 km in their model is not resolved by us due to the much shorter length data set (36 days against 22 months). Their results do not include a decrease in conductivity near 200 km in spite of their much better resolution in this depth range.

## 6. SOURCE FIELDS

The unusual, two dimensional complexity seen in the $Z_{xy}$ response function requires further investigation. Additional information is present in the vertical magnetic field variations. Figure 5 suggests that the Z fluctuations are significant from periods near 4 hours, where the spectrum falls off and whitens, to long periods. This result is supported by the SVD analysis of section 4.

### 6.1 Z VARIATIONS

In the absence of lateral conductive gradients the vertical magnetic field above a conducting medium should be small. This is because the internal (induced) and external (inducing) parts of the horizontal field reinforce each other while the vertical components cancel one another (Schmucker, 1970b). It is instructive to examine the Maxwell equations for the causes of time varying vertical magnetic fields. Taking the Z component of (7):

$$\nabla^2 Z - \mu\sigma \partial Z/\partial t = -\mu/\sigma(\partial\sigma/\partial x J_y - \partial\sigma/\partial y J_x) - \mu\sigma(F\cdot\nabla)w \qquad (17)$$

where w is the vertical component of fluid velocity. There are two source terms in (17): the first involves current channeling by lateral conductivity gradients while the second involves oceanic sources.

Lateral conductivity changes are the inferred cause of the anomalous Z variations seen at the coast-continent transition (Cox et al., 1970) and at major tectonic features on land (Gough, 1973). Currents concentrate in the most highly conductive material, producing anomalous Z variations on either side of the current system. The vertical magnetic field is most coherent with the component of the horizontal magnetic field orthogonal to the trend of the conductivity

FIGURE 11

Comparison of the SVD conductivity structure (solid line) to the results of Filloux (1977, short dashed line) and Klein and Larsen (1978, long dashed line) at Hawaii.

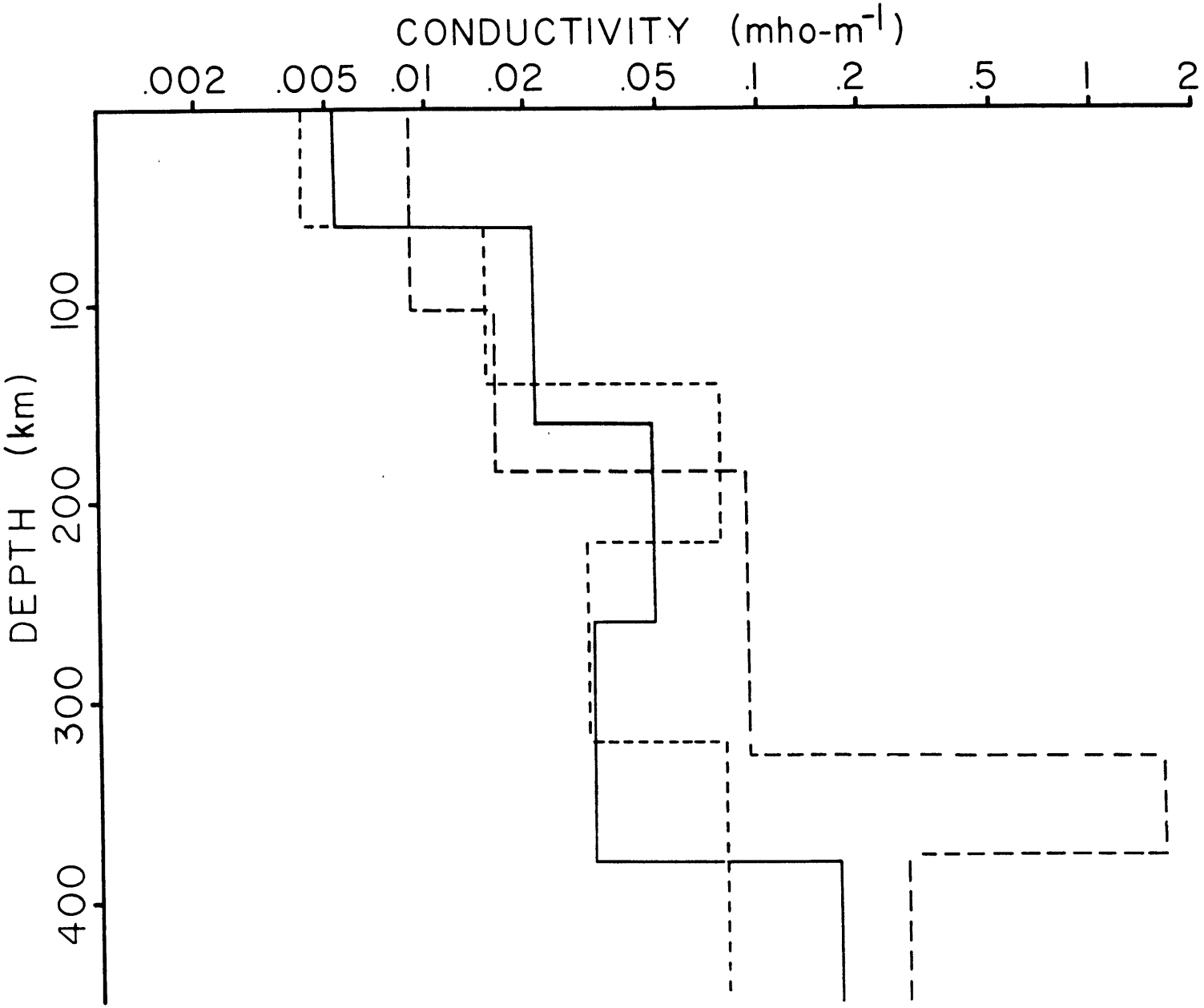
CONDUCTIVITY (mho-m$^{-1}$)
.002
.005
.01
.02
.05
.1
.2
.5
1
2
DEPTH (km)
100
200
300
400

contrast.

The oceanic term in (17) is unlikely to be significant outside of the tidal bands. Large scale, steady state motion in the deep ocean is approximated by the geostrophic equations on an f-plane: the pressure gradient and the Coriolis terms balance on a flat, rotating earth. It can be shown that the last term in (17) is zero to this degree of approximation. This means that oceanic flows which contribute to Z must exhibit departure from geostrophy, and the discussion of section 3.2 applies.

The nonuniformity of the source fields will also produce anomalous Z variations. It should be noted that a similar effect is produced by moving current systems in the ionosphere: horizontal drift of broad current systems lead to time-varying horizontal current gradients.

In order to evaluate the possible influence of either source fields or lateral conductivity changes we will consider the relationship between the vertical and horizontal magnetic fields in a quantitative manner. We will then consider the unusual response function $Z_{xy}$ and find some common factor that may explain it.

## 6.2 TRANSFER FUNCTIONS

From the magnetic field data we wish to determine the degree of correlation and the horizontal field direction of highest coherence with the vertical field. For two dimensional conductive structures that direction is constant with frequency and normal to the most conductive direction. For polarized source fields similar relations between the source currents and the magnetic fields exist.

We assume that Z is linearly related to H and D:

$$\tilde{Z} = A\tilde{H} + B\tilde{D} \qquad (18)$$

The complex, frequency dependent functions A and B are called tippers because they act to tip the horizontal field into the vertical plane. For noise-free data A and B will have identical phases and the most coherent horizontal field points in a direction arctan(A/B) from the strike of H (Vozoff, 1972). If A and B have different phases within the confidence limits then departures from ideality are indicated.

Rather than interpreting A and B individually we will derive composite quantities: the tipper coherence and the tipper function.

FIGURE 12

Tipper coherence calculated from (18) and the observed Z variations with twenty estimates or forty degrees of freedom per frequency band. The solid horizontal line is the 95% significance level above which the correlation is real.

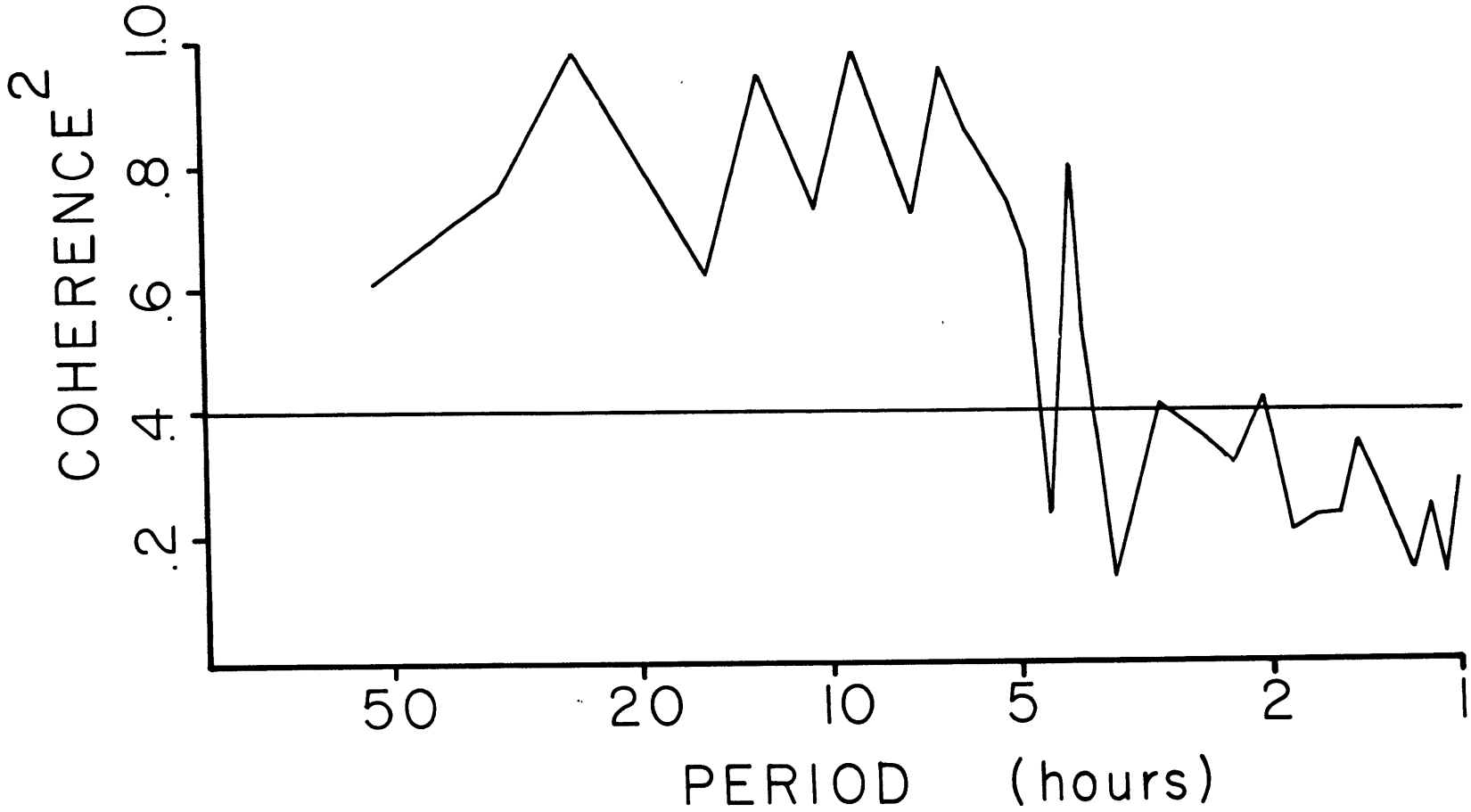
COHERENCE$^2$
1.0
.8
.6
.4
.2
50
20
10
5
2
1
PERIOD (hours)

FIGURE 13

Tipper function calculated from (19) and (20) with the 95% confidence limits calculated from the $\chi$-squared property of the auto and cross spectra. The large uncertainty makes the phase meaningless below five hours and it is not shown.

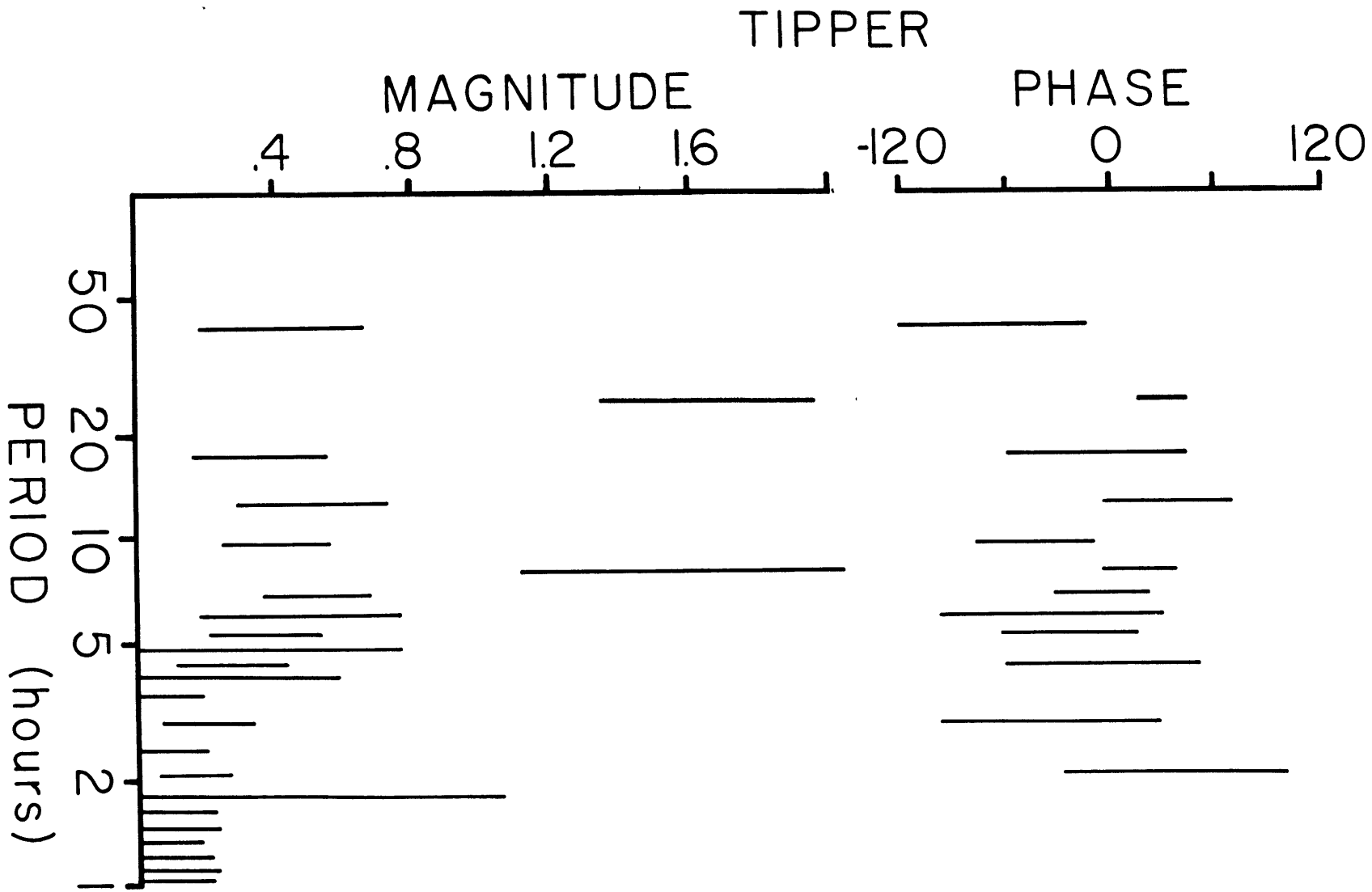
TIPPER
MAGNITUDE
PHASE
.4
.8
1.2
1.6
-120
0
120
50
20
10
5
2
1
PERIOD (hours)

Tipper coherence is the simple coherence between Z observed and that predicted by (18). It is a measure of the similarity of the Z variations and the horizontal magnetic field fluctuations. The tipper function combines A and B to get an amplitude and a phase:

$$T = \sqrt{A^2 + B^2} \qquad (19)$$

$$\delta = (A^2 \arctan(a_i/a_r) + B^2 \arctan(b_i/b_r))/T^2 \qquad (20)$$

where the subscripts i and r refer to the imaginary and real parts respectively. The absence of a slowly varying tipper permits the use of a simple layered interpretation. In addition, if the earth is two dimensional various estimates of the best rotation direction are possible (Jupp and Vozoff, 1976).

A connection between the tipper function in (19) and (20) and the response functions is easily made. Both are related to the inductive scale length (10) through different factors under the assumption of two dimensionality. For the tipper function the relation is:

$$C(\omega,k) = i\Lambda(\omega,k)/k \qquad (21)$$

where k is the source field wavenumber and $\Lambda$ is the complex tipper function combining (19) and (20). This also suggests that the tipper function is negligible if the zero wavenumber approximation is valid.

## 6.3 MOTION OF THE SOURCE FIELDS

Both the tipper coherence and tipper function were computed and appear as Figures 12 and 13. The 95% confidence limits on the least squares tipper functions have been estimated from the chi-squared property of the auto and cross spectra (Otnes and Enochson, 1972). Each of the frequency bands shown had twenty estimates for forty degrees of freedom per band.

The tipper coherence is significant for periods longer than 4-5 hours with a rapid fall-off at short periods. In the tidal bands the coherence approaches one. The low coherence below 4 hours could be due to low amplitude in Z: the signal-to-noise ratio is very low at these periods. Similar behavior is displayed by the tipper function in Figure 13: it is insignificant at the 95% level below 5 hours and the uncertainty makes the phase meaningless in this range. The tipper is smooth at long periods, suggesting a real correlation of Z with H and

D rather than a statistical fluctuation.

The inductive scale length is easily calculated from the data in Table 3. At five hours the appropriate length scale is 150 km, increasing to 270 km at 17 hours. This serves as a measure of the vertical and horizontal region influencing the induction and should encompass any conductive anomalies. There are no visible tectonic features on bathymetric charts over such distances (Figure 1). Anisotropy in the oceanic mantle would also explain the Z variations. The inductive scale length argument does apply here and we would require deep rather than shallow anisotropy. Other geophysical data, especially seismic surface waves, do not indicate large lateral changes in structure at great depths (Forsyth, 1975). We consider it unlikely that the long period Z coherence is due to lateral conductivity changes.

Source field complications deserve more serious consideration. It is possible to estimate the two dimensional source field wavenumber from (10) and (21) using the response and tipper functions. An alternate derivation from first principles is given in the appendix. In the range of 5-17 hours the source field wavenumber is approximately $10^{-3}$-$10^{-4}$ $km^{-1}$ for a mean wavelength of 5000 km. This is much larger than the inductive scale length and implies that finite source fields will not bias the response functions appreciably. This analysis applies only to stationary source fields and moving source currents should be examined.

Studies of the spatial extent and temporal behavior of source fields at mid-latitudes are rare. Nopper and Hermance (1974) used polarization analysis at a single high latitude station to show that motion of the ionospheric current system during polar magnetic substorms was common. Bannister and Gough (1977) deployed a large array of magnetometers from 55-60°N latitude and found rapid motion of the ionospheric current systems during a polar substorm in an east-west direction on a time scale of one hour. Beamish (1979) showed that source field effects biased the transfer functions for single events and used vertical field coherence as a weighting function to combine many events and minimize the contamination. All of these investigations were carried out north of 50°N latitude, much nearer

the auroral electrojet than our site. No comparable studies have been conducted at lower latitudes. It is not clear that the more globally distributed current systems associated with the $S_q$ daily variation and major magnetic storms do not display similar behavior.

A single site cannot be used to quantitatively determine source field behavior and an array of suitable dimensions is required. Polarization analysis can indicate the presence or absence of moving ionospheric current systems. Stationary current systems will produce stationary polarization ellipses when Z is plotted against the horizontal magnetic field. Motion of the current system produces rotation of the major axis of the ellipse and the direction of this motion is easily calculated from the vector relations of the field components.

We have selected two representative data sections for polarization analysis: one is a three day section during a magnetically quiet period that is dominated by $S_q$ and occasional bay disturbances and the second is a three day section after the start of a major storm event near the end of the time series in Figure 2. The latter section was chosen because the Z component seems to be suppressed. The tides were removed from the magnetic data by least squares to avoid dominance of the ellipses by the large diurnal and semidiurnal signals.

Figure 14 shows the first set of polarization diagrams for three bands: 1-5 hours, 5-10 hours, and 10-36 hours. Rotation of the polarization ellipse is marked at all periods while no consistent direction of motion for the current system was observed. The complex behavior in the shortest period band indicates that polar substorms, which produce the bay disturbances seen in the data, are complicated even at this low latitude. The longer period variations also demonstrate complex source field temporal morphology.

Figure 15 shows the same analysis for the storm time variations. The shortest period band shows suppression of the Z component and enhancement of the horizontal components of the magnetic field. Little ellipse rotation is apparent and it is likely that the plane wave source field assumption is valid here. At longer periods ellipse rotation with little consistency of the motion direction is seen.

The polarization analysis suggests a simple explanation for the

FIGURE 14

Polarization diagrams for quiet time variations using three period ranges: 10-36 hours, 5-10 hours, and 1-5 hours from left to right. The axes represent 7.5 nT for the first and last band and 5 nT for the middle one.

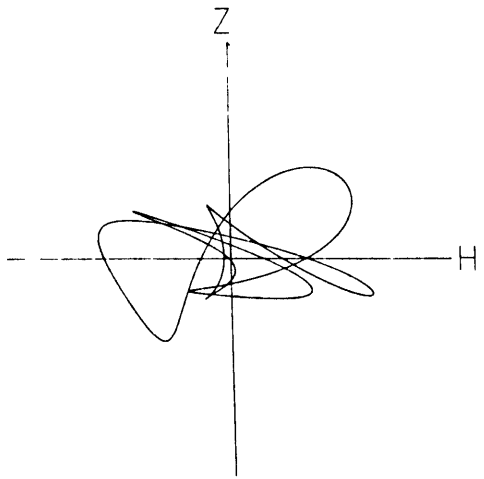
Z
H

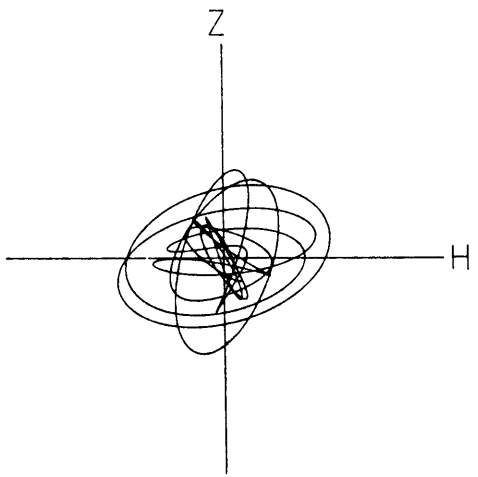
Z
H

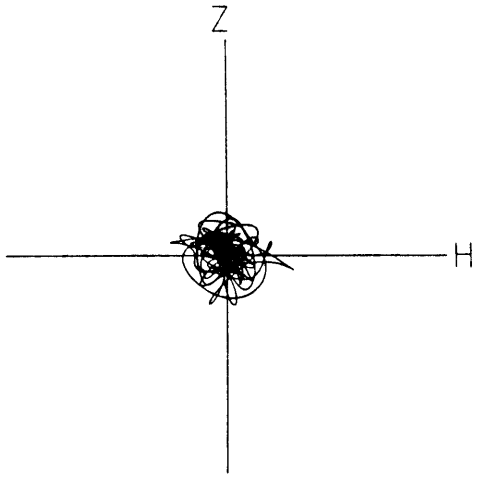
Z
H

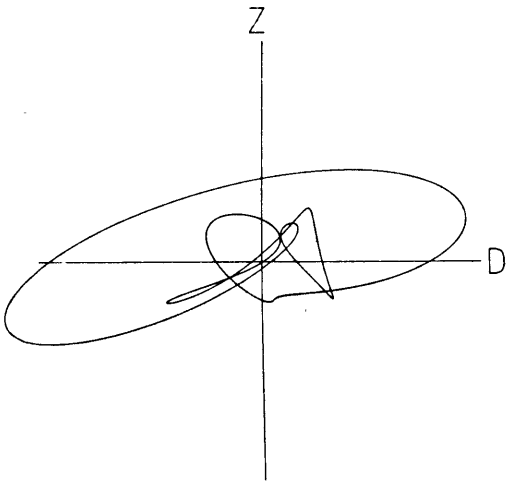
Z
D

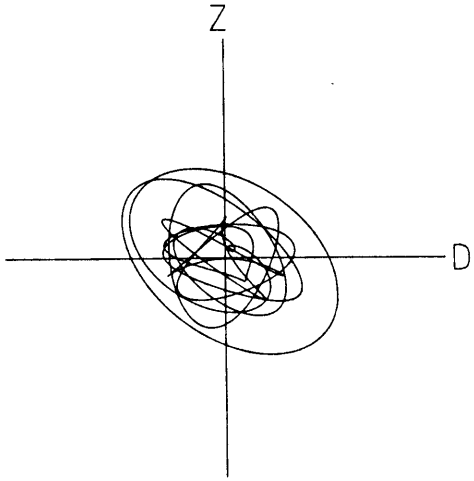
Z
D

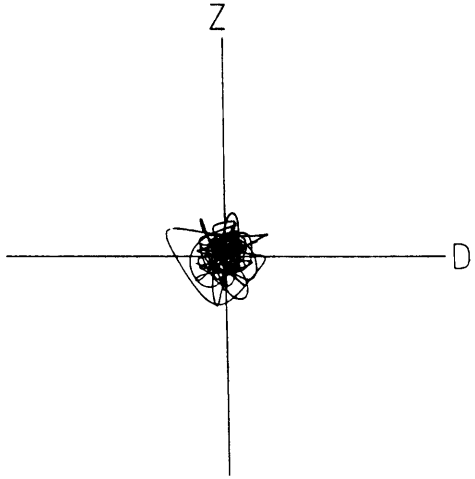
Z
D

FIGURE 15

Polarization diagram for storm time variations. See Figure 14 caption for details.

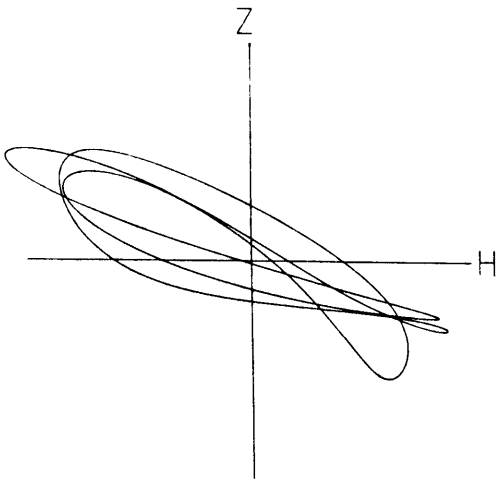
Z
H

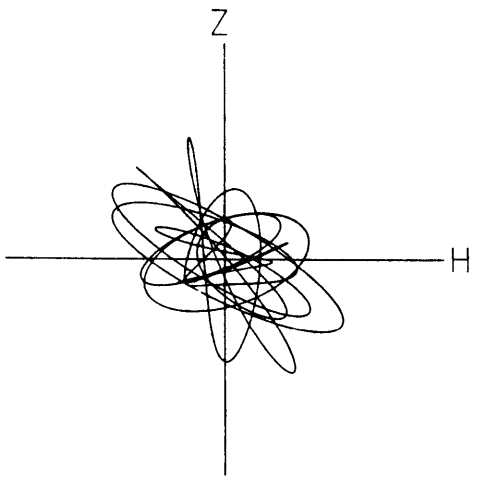
Z
H

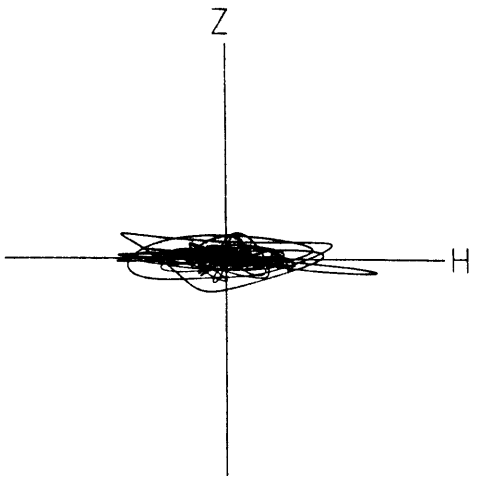
Z
H

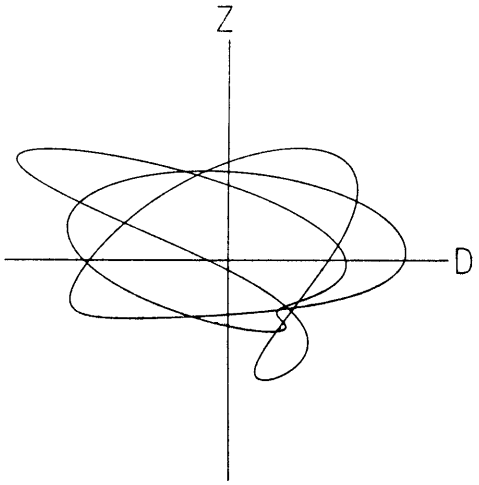
Z
D

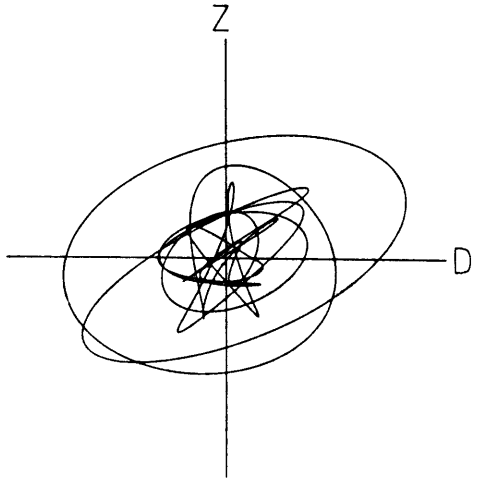
Z
D

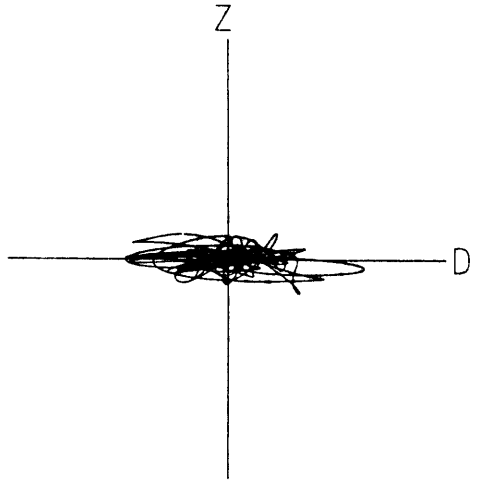
Z
D

large tipper and tipper coherence at periods longer than 5 hours. The source fields at long periods are complex and moving, yielding a high correlation of Z with the horizontal magnetic field. The best direction of this correlation is not constant as a function of period, a result consistent with the moving source hypothesis. At short periods the sources are strongly influenced by the type of ionospheric disturbance producing the fields. This means that Z will not be stationary in its relationship to the horizontal field and produces a low tipper coherence.

Moving source fields influence electromagnetic induction and the response functions will reflect this. Hermance (1978) has developed the theory of electromagnetic induction by moving, two dimensional current systems above layered media. He considered the influence of the motion on magnetotelluric impedances at short periods and concluded that the spectral broadening of the source increased the range of periods over which the zero wavenumber approximation is valid.

Solutions of the induction equation (8) for moving sources include a travelling wave term and modify the induction parameter (15) (Hermance, 1978):

$$\gamma_n = \sqrt{k^2 + i\mu\sigma_n(\omega \pm kv)} \qquad (22)$$

where v is the current system drift velocity. The inductive response is controlled by the relative magnitudes of the three terms in (22). Since the moving source term is linear in k it may be significant even for fairly low wavenumbers when the first or source field term can be neglected.

In order to quantitatively evaluate the effect of moving sources we have calculated the inductive response of a half space of conductivity 0.05 mho/m for a moving source with velocities of 0 to 300 m/sec. Current system speed of this order has been observed at high latitudes during polar magnetic substorms (Bannister and Gough, 1977). We take the source field wavelength to be 5000 km. The ratio of the last and first terms in (22) is 200:1 while the second and last terms have similar magnitudes. Because the polarization analysis suggests no consistent direction for the source motion, we assume that v is positive or negative half of the time and average the inductive responses. The results appear in Figure 16.

FIGURE 16

Model response curves for a uniform half space of conductivity 0.05 mho/m, which produces a constant 20 ohm-m apparent resistivity and a $45^{o}$ phase in the absence of any source field effects. The effect of drifting sources are shown. The sources are assumed to have both positive and negativee velocities on a shared basis. The drift velocity in m/sec are shown.

APPARENT RESISTIVITY
20
40
60
80
100
PHASE (degrees)
50
70
90
110
PERIOD (hours)
50
20
10
5
2
1
0
50
100
150
200
300
0
50
100
150
200
300

Moving source fields produce a peak in the apparent resistivity and a sharp increase in the phase at a period which increases with decreasing current system drift velocity and wavenumber. The transition becomes sharper as the velocity increases. This behavior is qualitatively similar to the $Z_{xy}$ response function in Figure 9. The peak in $Z_{xy}$ occurs near 8 hours and the phase rapidly approaches $90^{o}$ at longer periods. A current system drift at 150 m/sec produces a similar change in Figure 16. Increasing the source field wavenumber will lower this velocity. Since it is unlikely that the ionospheric current systems are entirely two dimensional or of uniform velocity, this model is highly idealized. It does suggest that north-south flowing currents drifting in the east-west direction will affect the mantle response function in the sense that is observed.

## 7. CONCLUSIONS

From this deep ocean study of the electromagnetic fields we conclude:

1. Oceanic tides are prominent in the east electric and north magnetic fields while ionospheric tides are dominant in the north electric and east magnetic components.
2. Application of singular value decomposition to a 36 day set of electricaand magnetic field data suggests three degrees of freedom in the data set for periods longer than five hours, decreasing to two degrees of freedom below this. This implies that source fields are influencing the induction at long periods.
3. Response functions, calculated using least squares and SVD techniques, yield two principal directions and small off-diagonal terms. The apparent resistivity is over and under estimated by least squares due to the unrealistic assumptions made about noise distribution. Only one of the principal response functions, $Z_{yx}$, can be interpreted as a one dimensional conductive structure. Two dimensionality of the layered medium or of the source fields must be invoked to explain the other.
4. The one dimensional interpretation of $Z_{yx}$ includes a rise in conductivity to 0.05 mho/m at depths in excess of 160 km. No decrease in conductivity below this can be resolved and the conductivity in the top 100 km is poorly constrained. Both SVD and least squares response

functions produce similar results although the former are much easier to fit with a layered model.

5. The vertical and horizontal magnetic fields are highly correlated at periods in excess of five hours. Polarization analysis suggests that the source fields are in constant motion with respect to the observation site. Source field wavelengths are near 5000 km. Electromagnetic induction models for moving sources produce two dimensionality in the response curves similar to that in $Z_{xy}$. This suggests that east-west drift of north-south flowing electric currents influences the inductive response at this mid-latitude site.

# APPENDIX

## DETERMINATION OF THE SOURCE FIELD WAVENUMBER

Schmucker (1970b) defined the inductive scale length and derived its relationship to the response and tipper functions through the use of convolution integrals. A similar form can easily be derived from the Maxwell equations (1)-(4).

We assume that a two dimensional source field induces a magnetic field in a flat layered earth. Solutions of the induction equation (8) have the form:

$$B = \tilde{B}(z)\ e^{i(kx - \omega t)} \qquad \text{(A-1)}$$

where ~ indicates the Fourier transform in k and $\omega$. A solution of (8) for $B_z$ is:

$$B_z = e^{-\gamma z}\ e^{i(kx - \omega t)} \qquad \text{(A-2)}$$

where $\gamma$ is the induction parameter. The divergence condition (2) on the magnetic field yields:

$$B_x = \gamma/ik\ B_z \qquad \text{(A-3)}$$

Ampere's law (4) is easily solved for $E_y$ and combined with (A-3) to yield the response function $Z = E_y/B_x$. Elimination of $\gamma$ then gives the desired result:

$$k = \omega\Lambda/Z \qquad \text{(A-4)}$$

where $\Lambda = B_z/B_x$.

# REFERENCES

Banks, R.J., 1969. Geomagnetic variations and the electrical conductivity of the upper mantle, Geophys. J. Roy. astr. Soc. 17, 457-487.

Bannister, J.R. and D.I. Gough, 1977. Development of a polar magnetic substorm: a two-dimensional magnetometer array study, Geophys. J. Roy. astr. Soc. 51, 75-90.

Beamish, D., 1979. Source field effects on transfer functions at mid-latitudes, Geophys. J. Roy. astr. Soc. 58, 117-134.

Bentley, C.R., 1973. Error estimation in two-dimensional magnetotelluric analyses, Phys. E. Pl. Int. 7, 423-430.

Cox, C.S., J.H. Filloux, and J.C. Larsen, 1970. Electromagnetic studies of ocean currents and electrical conductivity below the sea floor, in A.E. Maxwell (ed.), The Sea, V. 4, Pt. 1, New York: John Wiley, pp. 637-693.

Cox, C.S., J.H. Filloux, D.I. Gough, J.C. Larsen, K.A. Poehls, R.P. Von Herzen, and R. Winter, 1980. Atlantic lithosphere sounding, submitted to J. Geomag. Geoelec.

Daniel, T.H., 1978. Tri-axial electric field measurements for determining deep ocean water motions: techniques and a preliminary application, Ph.D. dissertation, Univ. of Hawaii, Honolulu, 185 pp.

Filloux, J.H., 1973. Techniques and instrumentation for the study of natural electromagnetic induction at sea, Phys. E. Pl. Int. 7, 323-338.

Filloux, J.H., 1974. Electric field recording on the sea floor with short span instruments, J. Geomag. Geoelec. 26, 269-279.

Filloux, J.H., 1977. Ocean floor magnetotelluric sounding over north central Pacific, Nature 269, 297-301.

Fisher, R., 1929. Test of significance in harmonic analysis, Proc. R. Soc. Lon. A125, 54-59.

Forsyth, D.W., 1975. The early structural evolution and anisotropy of the oceanic upper mantle, Geophys. J. Roy. astr. Soc. 43, 103-162.

Gough, D.I., 1973. The geophysical significance of geomagnetic variation anomalies, Phys. E. Pl. Int. 7, 379-388.

Hermance, J.F., 1978. Electromagnetic induction in the earth by moving ionospheric current systems, Geophys. J. Roy. astr. Soc. 55, 557-576.

Jupp, D.L.B., 1978. Estimation of the magnetotelluric impedance functions, Phys. E. Pl. Int. 17, 75-82.

Jupp, D.L.B. and K. Vozoff, 1976. Discussion on "The magnetotelluric method in the exploration of sedimentary basins", Geophysics 41, 325-328.

Klein, D.P. and J.C. Larsen, 1978. Magnetic induction fields (2-30 cpd) on Hawaii Island and their implications regarding electrical conductivity in the oceanic mantle, Geophys. J. Roy. astr. Soc. 53, 61-77.

Lanczos, C., 1961. Linear Differential Operators, D. Van Nostrand, London, 564 pp.

Larsen, J.C., 1966. Electric and magnetic fields induced by oceanic tidal motion, Ph.D. dissertation, Univ. of California, San Diego, 99 pp.

Larsen, J.C., 1968. Electric and magnetic fields induced by deep sea tides, Geophys. J. Roy. astr. Soc. 16, 47-70.

Larsen, J.C., 1973. An introduction to electromagnetic induction in the ocean, Phys. E. Pl. Int. 7, 389-398.

Larsen, J.C., 1975. Low frequency (0.1-6.0 cpd) electromagnetic study of deep mantle electrical conductivity beneath the Hawaiian Islands, Geophys. J. Roy. astr. Soc. 43, 17-46.

Larsen, J.C., 1980. One-dimensional layered electrical conductivity interpretation, submitted to Geophysics.

Nopper, R.W. and J.F. Hermance, 1974. Phase relations between polar magnetic substorm fields at the surface of a finitely conducting earth, J. geophys. Res. 79, 4799-4801.

Otnes, R.K. and L. Enochson, 1972. Digital Time Series Analysis, New York: John Wiley, 467 pp.

Parker, R.L., 1970. The inverse problem of electrical conductivity in the mantle, Geophys. J. Roy. astr. Soc. 22,121-138.

Poehls, K.A., 1975. Geomagnetic variations in the northwest Atlantic: implications for the electrical resistivity of the oceanic lithosphere, Ph.D. dissertation, Mass. Inst. of Technology and Woods Hole Oceanographic Inst., 134 pp.

Poehls, K.A. and R.P. Von Herzen, 1976. Electrical resistivity structure beneath the northwest Atlantic Ocean, Geophys. J. Roy. astr. Soc. 48, 331-346.

Sanford, T.B., 1971. Motionally induced electric and magnetic fields in the sea, J. geophys. Res. 76, 3476-3492.

Schmucker, U., 1970a. Anomalies of geomagnetic variations in the southwestern United States, Bull. Scripps Inst. Ocean. 13, 1-165.

Schmucker, U., 1970b. An introduction to induction anomalies, J. Geomag. Geoelec. 22, 9-33.

Schmucker, U., 1971. Interpretation of induction anomalies above nonuniform surface layers, Geophysics 36, 156-165.

Sokal, R.R. and F.J. Rohlf, 1969. Biometry, San Francisco: Freeman and Co., 776 pp.

Vozoff, K., 1972. The magnetotelluric method in the exploration of sedimentary basins, Geophysics 37, 98-141.

Weidelt, P., 1972. The inverse problem of geomagnetic induction, J. Geophys. 38, 257-289.

# CHAPTER FOUR

# GEOMAGNETIC SECULAR VARIATION RECORDED IN SEDIMENTS FROM THE NORTHEAST ATLANTIC OCEAN

# GEOMAGNETIC SECULAR VARIATION RECORDED IN SEDIMENTS FROM THE NORTHEAST ATLANTIC OCEAN*

Alan D. Chave[1]

Woods Hole Oceanographic Institution
Woods Hole, MA 02543
and
Department of Earth and Planetary Sciences
Massachusetts Institute of Technology
Cambridge, MA 02139

Charles R. Denham

Woods Hole Oceanographic Institution
Woods Hole, MA 02543

* submitted to J. geophys. Res.

1. present address:

Geological Research Division A-015
Scripps Institution of Oceanography
La Jolla, CA 92093

ABSTRACT

A suite of piston cores, obtained in a high deposition rate area in the northeast Atlantic Ocean, were used for a detailed geomagnetic secular variation study over the time interval 25-127 kybp. Stratigraphic control was provided by planktonic foraminiferal assemblages with a resolution of a few thousand years. An inter-core correlation procedure was used on five sets of down-core stratigraphic data to show that a significant change in sedimentation rate occured at the interglacial-glacial transition 60-80 kybp. The sedimentation rate was 4 cm/ky during glacial times, increasing to 7-9 cm/ky during interglacials.

Demagnetization analysis on forty-six pilot samples from four piston cores reveals a stable remanence with a median demagnetizing field of 315±44 oe and a directional change of $4.8\pm2.2^{o}$ over a 300 oe range. ARM reproduces the coercive force spectrum of the NRM over a 150-400 oe range. Down-core paleomagnetic time series were obtained in four cores covering parts of the interval 25-127 kybp. The directions correlate visually only in the glacial interval prior to 77 kybp. Relative paleointensity, determined by the pNRM/pARM method, is dominated by a long period (30 ky) signal that may be of climatic origin. Spectral analysis of the directions indicates long period (10 ky) looping of the geomagnetic field vector with no characteristic direction for the motion. In the interglacial interval 77-127 kybp no consistent result could be found, suggesting erosion or sediment rate variations that are not resolvable.

# 1. INTRODUCTION

The geomagnetic spectrum is open-ended, covering a range of periods from seconds to tens of millions of years. For periods shorter than thirteen years the variations are due to processes in the ionosphere and magnetosphere external to the earth (Alldredge, 1976). Changes in the average frequency of geomagnetic reversals occupy the opposite end of the spectrum with a characteristic period near 50 my (Cox, 1975). Between these two extremes lies the range of secular variation and geomagnetic reversals, both caused by complex magnetohydrodynamic processes in the earth's core. Geomagnetic reversals are well documented over Cenozoic and Mesozoic times, and the resulting magnetic time scale is a key tool in geological and geophysical investigations. The secular variation field on a time scale of $10^2$-$10^5$ years is less well understood, mainly due to a lack of resolution and continuity in the paleomagnetic record.

We report here on a replicate set of paleomagnetic field directions and relative paleointensities measured in four cores in a high deposition rate area of the northeast Atlantic Ocean. The cores cover a time interval through the last interglacial, which started 127 kybp. Continuous paleomagnetic measurements allow a resolution of 300-1000 years over parts of this range. Rather than emphasize a subjective visual correlation of the magnetic time sequences, we take a quantitative approach and apply time series analysis techniques to the data. The resulting power spectra show that looping motion of the geomagnetic field vector with a characteristic period near 10 ky has been prevalent for the last 100 ky. The field intensity has changed on a much longer time scale, with a marked peak near 30 ky period.

## 1.1. PREVIOUS WORK

The present day geomagnetic field is made up of two components: a dipole offset by about $11^{\circ}$ from the rotation axis of the earth and a more complex, higher order multipole or nondipole field. Westward drift of both parts at a rate of 0.1-0.4 degrees per year has been observed in historic data covering the last few hundred years. James (1970) showed that only the large dipole and quadrapole fields move, while the remaining nondipole field is stationary and fluctuating in

intensity.

Extension of historic observations of geomagnetic behavior to a time scale of $10^3$-$10^5$ years requires paleomagnetic records that are both detailed and continuous. High deposition rate sedimentary environments offer the best resolution available, as shown by paleomagnetic work on present day lacustrine sediments (Thompson, 1975; Creer, 1977), dry lake beds (Denham and Cox, 1971; Denham, 1974; Liddicoat and Coe, 1979), and marine sediments (Opdyke et al., 1972). Most of these studies show a looping motion of the ancient field vectors on a time scale of 2-5 ky. Skiles (1970) used the looping sense to infer a drift direction for the geomagnetic multipoles. Westward drift usually produces clockwise field vector motion, although exceptions do occur (Dodson, 1979).

The characteristic relaxation time of the magnetohydrodynamic processes in the earth's core is $10^3$-$10^4$ years (Busse, 1975). Extension of paleomagnetic records beyond the $10^4$ year maximum available in glacial lakes can provide valuable constraints on the theory of planetary dynamos. The longest available directional paleomagnetic record spans about 20 ky (Opdyke et al., 1972) and no comparable paleointensity determination exists.

## 2. REGIONAL SEDIMENTARY ENVIRONMENT

The sediment cores used in this study were collected from a 1500 $km^2$ area near $56^oN$, $29^oW$ on cruise 94 of the Atlantis II in July 1977 (Figure 1). The site is located on the eastern flank of the Reykjanes Ridge on 35 my old lithosphere. Detailed surveys were conducted using a 12 kHz profiler, 40 cubic inch airgun seismics, and towed magnetometer with detailed navigational control from frequent Loran-C fixes. Figure 2 shows the bathymetry and sediment isopachs for the survey area. Thirteen 10 m long piston cores were successfully recovered.

The sedimentary regime in the North Atlantic is dominated by localized bottom current erosion and redistribution. Sediment cover is uneven and not conformable to basement topography throughout the area shown in Figure 1 (Ruddiman, 1972). The present day deep water circulation in the northeast Atlantic is controlled by episodic overflow of cold, saline water from the Norwegian Sea via the Iceland-Faeroes

FIGURE 1

Index map showing the principal physiographic features of the northeast Atlantic Ocean with Iceland at the top and Ireland at the right (shaded areas). The Gardar Drift is idealized as the elongate stippled area in the center of the figure. Bathymetric contours at 1, 2, 3, and 4 km are shown. The boxed area at the left center of the map is the detailed study area shown in Figure 2.

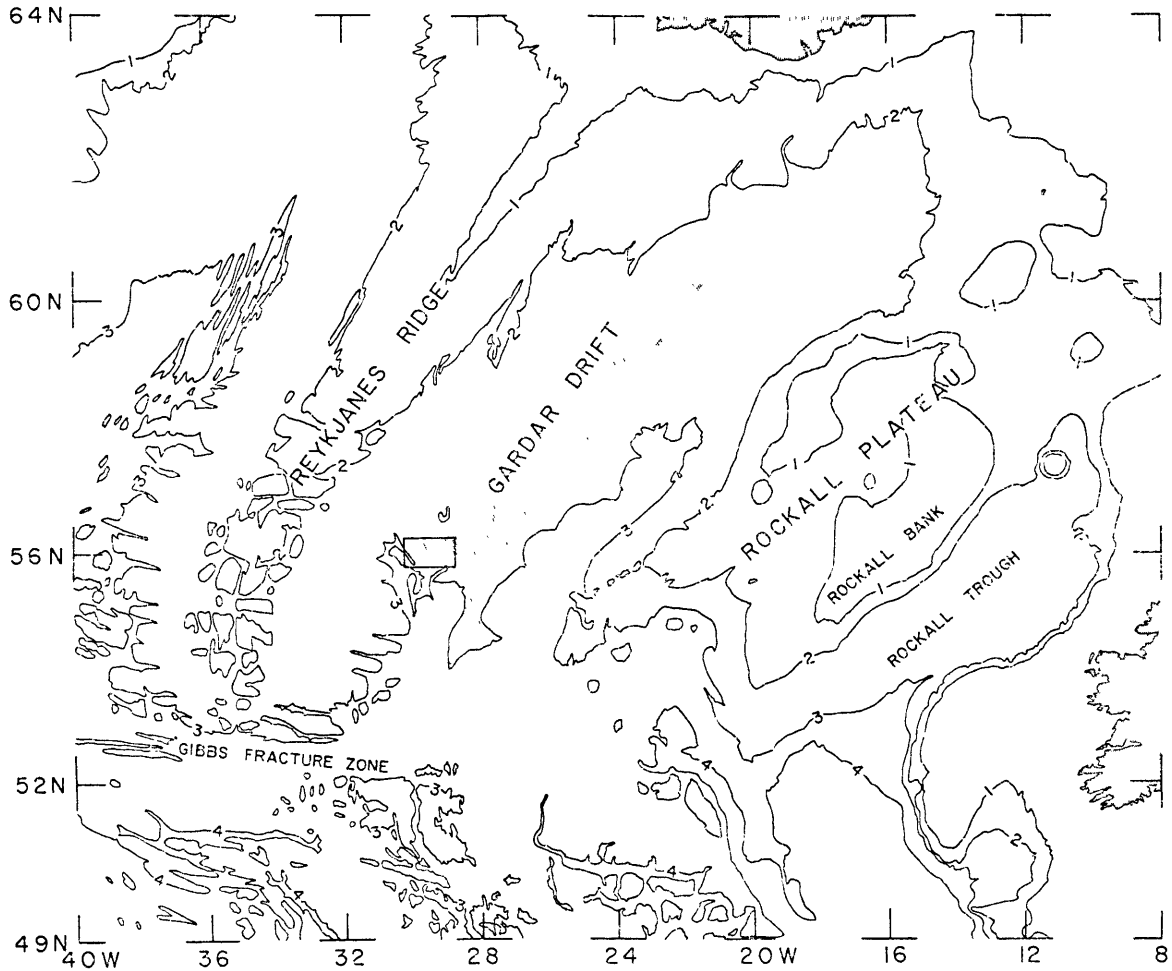
64N
60N
56N
52N
49N
40W
36
32
28
24
20W
16
12
8
REYKJANES RIDGE
GARDAR DRIFT
ROCKALL PLATEAU
ROCKALL BANK
ROCKALL TROUGH
GIBBS FRACTURE ZONE

Ridge. This water flows southwest along the eastern flanks of both the Rockall Plateau and the Reykjanes Ridge, eventually passing through the Gibbs Fracture Zone into the western basin. The path taken by the flow is largely controlled by bathymetry below 1500 m with flow velocities in the range of 10-30 cm/s reported (Steele et al., 1962).

Deposition of sediment ridges or drifts occurs at the boundary between a moving current and surrounding stationary water with peak sedimentation where the velocity gradient is largest. The Gardar Drift, shown in Figure 1 as the stippled area, has been laid down since late Eocene or early Oligocene time (Ruddiman, 1972). It is an elongate pile of acoustically transparent, nonconformable sediment 50 km wide and 300 m high (Johnson and Schneider, 1969).

The detailed bathymetry of the collection site (Figure 2) reveals east-west lineation with water depth varying from 2700 m at the north to 2850 m at the south edge. We infer that the survey area is located on the southern flank of a western extension of the drift. The sediment isopach map shows rugged basement topography and nonconformable draping of the sediment cover. Sediment isopachs vary from zero on outcropping basement to nearly one second between the basement ridges which strike north-south, corresponding to sediment thicknesses of 0-1000 m.

## 3. STRATIGRAPHY

### 3.1 SEDIMENT CORES

The sediments used in this study were recovered using a standard 15 m piston coring apparatus with plastic core liners to contain the sediments. The core liners were locked into the steel core barrels during coring operations to preserve the orientation of the plastic sections. A core orienting device (Seyb et al., 1977) was installed in the core head. Poor quality of the film record precludes use of the accelerometer data, and an actual trace of core orientation with penetration depth is not available. The magnetic compass data indicate only limited rotation through $10\text{-}30^{\circ}$ during the 2-3 seconds required for penetration and the geographic orientation of the corer was nearly identical in all cores. Heat flow outriggers mounted on the core barrels could explain the limited rotation, but the geographic

FIGURE 2

Sediment isopachs (top) and bathymetry (bottom) for the boxed area of Figure 1. Bathymetric contours are expressed in corrected meters and sediment isopachs are in seconds of two way travel time. The circles indicate the locations of piston cores with the five solid circles corresponding to the five cores selected for this study (see text).

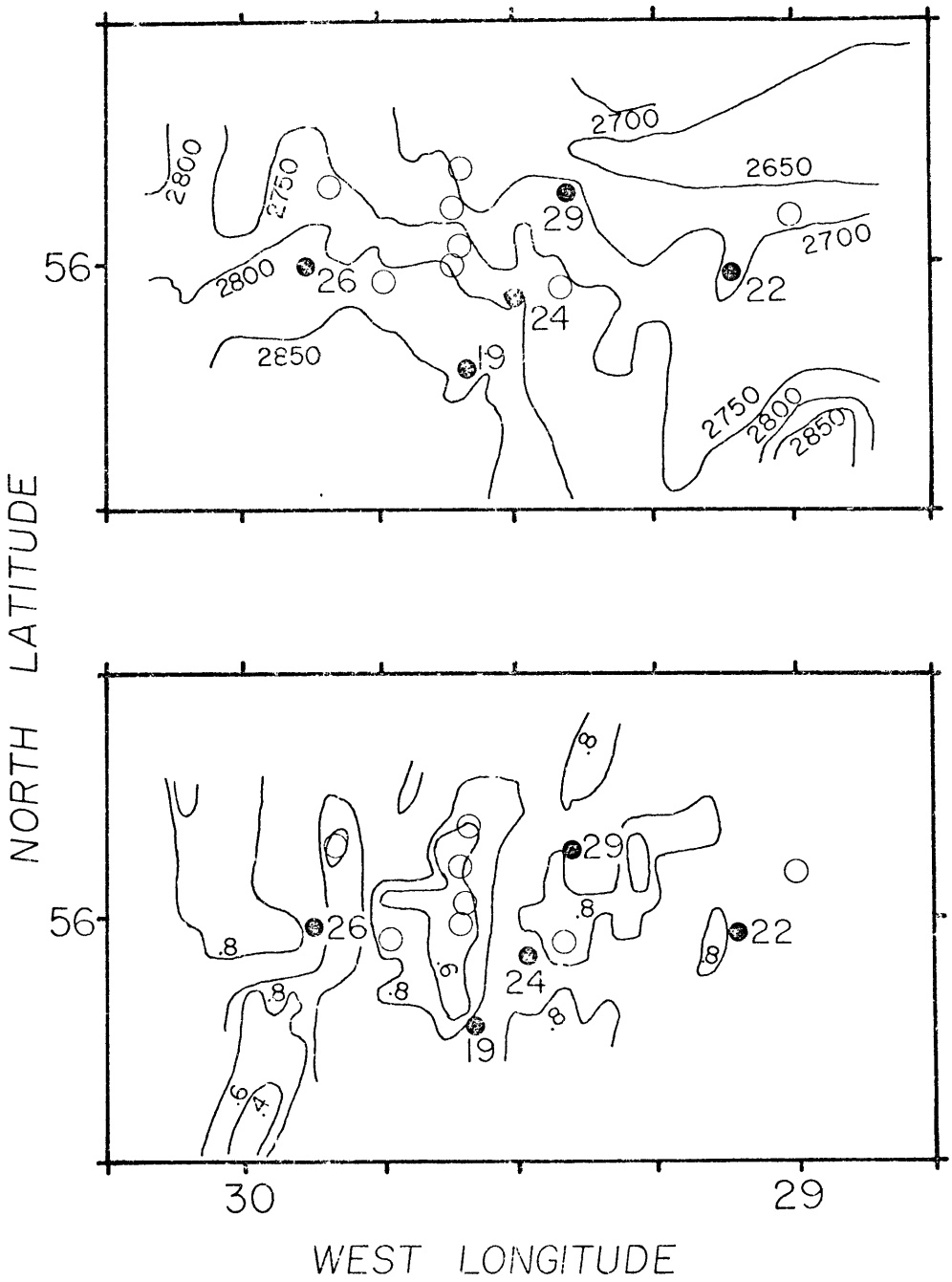
2700
2650
2800
2750
29
2700
56
2800
26
22
24
2850
19
2750
2800
2850
.8
29
.8
56
26
.8
22
.8
.8
.8
24
.8
.8
19
.6
.4
30
29
NORTH LATITUDE
WEST LONGITUDE

orientation is unlikely to occur at random. We infer that the trip arm and associated trigger core acted as a vane in the ambient bottom current and controlled the position of the corer.

The sediments in all thirteen piston cores consist of alternating layers of white to tan carbonate ooze and brown glacial marine deposits. Ice rafted debris and erratics are common in the latter sediment type. Calcium carbonate content was determined gasometrically and varies from 20-80% by weight. Dissolution effects on the microfossil assemblages are negligible. The transition zone between the two sediment types is gradual and mottled by burrows from biological organisms. Flow-in and other coring disturbance is minimal, affecting only the bottom 10-50 cm of any given core. No turbidites were observed.

Visual examination of the sediment core tops showed carbonate ooze, indicative of the present warm climate, in only five cores. This was confirmed by faunal analysis: the five cores had low abundances of the planktonic foraminifer Globigerina pachyderma, s., in contrast to the remaining eight cores. The trigger cores displayed the same pattern, suggesting that the Holocene section is missing from the sedimentary record. Figure 2 reveals a direct correlation of the five intact cores with sediment thickness: erosion occurs where the sediment cover is thinnest. This is consistent with action by bathymetrically controlled bottom currents. Due to the real possibility of undetectable down-core erosional events that could distort the magnetic record, we chose to continue the analysis on only the five complete cores.

## 3.2 BIOSTRATIGRAPHY

Late Quaternary stratigraphic control in North Atlantic sediments is excellent, largely due to the efforts of the CLIMAP group (Cline and Hays, 1976). Extensive information on floral and faunal stratigraphy and ash layer chronology is available. The climatic cycle exerts a dominating influence on the ecological system at high latitudes and this is reflected in sediment lithology and fossil assemblages. Large amplitude changes in down-core species abundance yields a detailed, multivariate measure of stratigraphic level. The choice of several chronostratigraphic horizons can then be used to develop a time scale.

The ecological water mass assemblages proposed by McIntyre et al.

(1972) and modified by Ruddiman and McIntyre (1976) provide the required detailed biostratigraphy. Through statistical analyses and studies on living foraminifera they found that some 15 species could be grouped into four assemblages due to covariation of abundance. Table 1 lists the assemblage, species, and a taxonomic reference used in this work. The most important assemblage is the polar group, consisting of the left coiling form of Globigerina pachyderma, whose abundance is an excellent first order indicator of climate (Ruddiman and McIntyre, 1976). High concentrations of this species indicates cold climate. Additional stratigraphic control is provided by three silicic ash layers mapped throughout the high latitude North Atlantic by Ruddiman and Glover (1972).

We obtained samples every 10-20 cm from the split core working half, varying the sample interval in order to adequately resolve any visible changes in sediment lithology. The sediment plugs were washed and sieved using standard techniques. Small splits from the coarse fraction (greater than 149 μm) were counted. At each level 100 planktonic foraminifera were identified and sorted using the assemblages of Table 1. The total number of non-carbonate fragments and silicic ash shards were also noted. The nine species listed in the table dominated the fauna in all samples. During warm intervals additional tropical species were seen only occasionally. These were excluded from the sums along with any unidentified species. The total rejected fauna did not constitute more than a few percent of the total. Additional taxonomic guidelines may be found in Ruddiman and McIntyre (1976) and the references cited in Table 1.

Figure 3 shows the resulting down-core stratigraphy for the five cores used in this study. The foraminiferal data are expressed as cumulative percentages as in Ruddiman and McIntyre (1976) with non-carbonate detritus excluded from the total. The detrital data are expressed as a percentage of the total coarse fraction, excluding silicic bubble shards. Visual correlation of these curves is excellent, especially in the high amplitude polar assemblage which changes from 0 to nearly 90% of the total. Warm climate is suggested at the top of each core and again near the bottom. The detrital fraction is low to nonexistent during warm intervals and high during cold climate with

TABLE 1

PLANKTONIC FORAMINIFERAL ASSEMBLAGES

| Assemblage | Foraminiferal Species | Reference |
|---|---|---|
| Polar | Globigerina pachyderma, s. | 1 |
| Subpolar | Globigerina bulloides | 2 |
| | Globigerina pachyderma, d. | 1 |
| | Globigerina quinqueloba | 2 |
| Transitional | Globorotalia inflata | 2 |
| | Globoquadrina dutertrei | 2 |
| Subtropical | Globorotalia hirsuta | 2 |
| | Globorotalia truncatulinoides | 2 |
| | Globorotalia scitula | 2 |

1. Kennett, 1968.
2. Parker, 1962.

FIGURE 3

Raw down-core stratigraphy using the planktonic foraminiferal assemblages of Table 1 (top) and non-carbonate detritus and bubble ash shards (bottom). The faunal data are expressed as cumulative percentages of the water mass assemblages. The stippled area is the polar assemblage. The remaining assemblages are, from right to left, subpolar, transitional, and cold subtropical. See text for details. The inferred oxygen isotope stage boundaries are shown by the dotted lines.

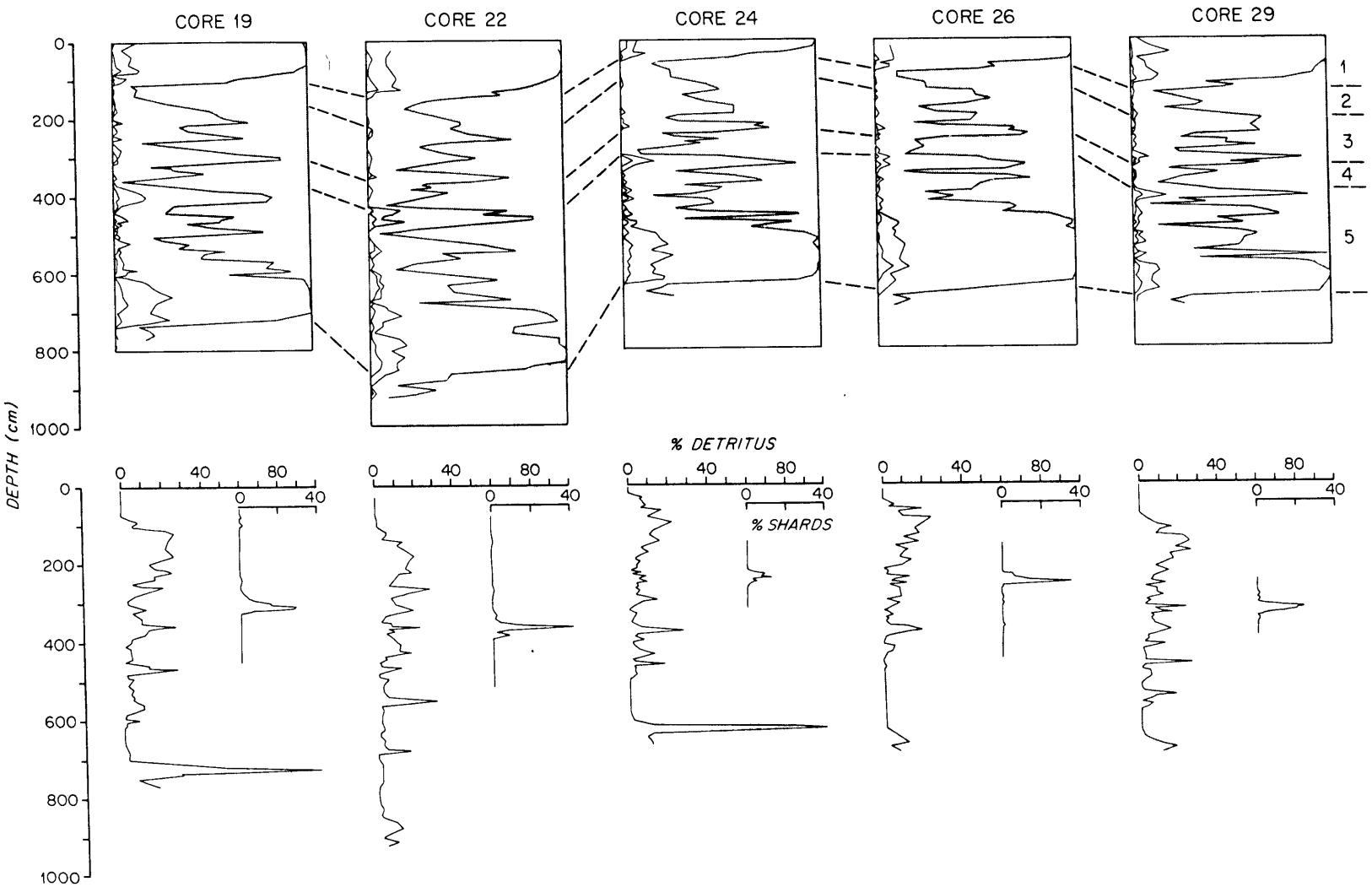
CORE 19
CORE 22
CORE 24
CORE 26
CORE 29
DEPTH (cm)
0
200
400
600
800
1000
1
2
3
4
5
% DETRITUS
% SHARDS
0
40
80

prominent spikes during deglaciation events. A single ash layer of the type described by Ruddiman and Glover (1972) is seen near the middle of each core. Figure 3 also shows the oxygen isotope stage boundaries inferred by correlation to global data.

## 3.3 CHRONOSTRATIGRAPHY

Microscopic examination of smear slides for all five sediment cores reveals a high abundance of the coccolithophorid Emiliania huxleyi. This species evolved late in oxygen isotope stage 8 some 270 kybp (Thierstein et al., 1977). This limits the single climatic cycle seen in Figure 3 to either major cycle B (13.5-127 kybp) or C (127-225 kybp). By comparison to the extensive work of Ruddiman and McIntyre (1976) we conclude that it represents the last glacial/interglacial cycle.

The ages of several of the prominent climatic events seen in Figure have been determined by radiometric methods. Exposed reef terraces created during ancient high stands of sea level have been dated on Barbados (Mesolella et al., 1969; James et al., 1971) and Bermuda (Harmon et al., 1978) using both $Th^{230}/U^{234}$ and $Pa^{231}/U^{235}$ techniques. Shackleton and Matthews (1977) connected these results to the global oxygen isotope time scale, providing an absolute calibration for climatically controlled stratigraphic variables. The major climatic Terminations I at the stage 1/2 boundary and II at the stage 5/6 boundary have been dated using $C^{14}$ and other methods (Ku and Broecker, 1966; Broecker and van Donk, 1970; McIntyre et al., 1972; Ruddiman and McIntyre, 1973). The correspondence of the isotopic and faunal cycles over the last 600,000 years was established by Ruddiman and McIntyre (1976). This yields a set of absolute ages to which the faunal data can be linked by correlation.

Table 2 list ten possible chronostratigraphic horizons chosen from the literature. Ruddiman and McIntyre (1979) found a consistent lag of 3-5 ky between sea surface temperature, as measured by planktonic foraminiferal abundance, and isotopic ratios. The ages listed in Table 2 have been modified by 4 ky to reflect this.

A possible time scale for the faunal data can be obtained by interpolation between Terminations I and II. If the sedimentation rate

TABLE 2

CHRONOSTRATIGRAPHIC HORIZONS

| Event | Age | Uncertainty | Source | Reference |
|---|---|---|---|---|
| Ash I | 9.3 | 0.5 | $C^{14}$ | 1 |
| Younger Dryas cooling | 10.2 | 0.5 | $C^{14}$ | 2 |
| Termination I | 13.5 | 0.5 | $C^{14}$ | 2 |
| Oxygen isotope 3/2 bdy | 29 | 6 | $O^{18}$ interpolation | -- |
| Oxygen isotope 4/3 bdy | 60 | 6 | $O^{18}$ interpolation | -- |
| Ash II | 61 | 6 | interpolation | 3 |
| Oxygen isotope 5/4 bdy | 72 | 6 | $O^{18}$ interpolation | -- |
| Barbados I | 77 | 4 | $Th^{230}/U^{234}$, $Pa^{231}/U^{235}$ | 4 |
| Oxygen isotope 5e/5d bdy | 115 | 6 | $O^{18}$ interpolation | -- |
| Termination II | 127 | 6 | $Th^{230}/U^{234}$ | 5,6 |


1. Ruddiman and McIntyre, 1973.
2. Ruddiman et al., 1977.
3. Ruddiman and Glover, 1972.
4. Mesolella et al., 1969.
5. Ku and Broecker, 1966.
6. Broecker and Van Donk, 1970.

does not change between interglacial and glacial times, then this is probably the best estimate possible. Since additional age picks are available, a quantitative procedure to determine those points which are necessary and sufficient is required. A correlation approach using five local measurements of the stratigraphic variables is outlined in the appendix. Those age picks which maximize the inter-core correlation, as determined by empirical orthogonal function (EOF) analysis, are used.

Figure 4 shows the polar assemblage EOF's for age picks at Terminations I and II. The first or signal EOF contains 67% of the variance in the original data. The remaining four noise EOF's have been summed for graphical display. Comparison of the data to Figure 4 reveals a lack of detail in the correlated result over the interval 60-100 kybp. The residual is both large and slowly varying over this range, suggesting discordance of the correlation due to a glacial/ interglacial contrast in sedimentation rate.

Figure 4 shows the EOF's for three age picks with the addition of the Barbados I event at 78 kybp. The signal EOF contains 82% of the variance, an improvement over the previous result which is significant at the 95% level (see appendix). The stratigraphic detail seen in the original data is now present in the signal EOF. The variation in the noise EOF has a high frequency character that is widely distributed in age.

Other trial horizons from Table 2 were used and the analysis repeated. In no case were four age picks necessary. Results identical to those in Figure 6 were obtained by substituting either the stage 4/3 boundary or the stage 5/4 boundary for the Barbados I warming. This means that the decrease in sedimentation rate seen in glacial times may have started anywhere from 60-80 kybp.

Figure 5 shows the final stratigraphy using Terminations I and II and the Barbados I event as chronostratigraphic horizons. Visual correlation is high with some inter-core discrepancies apparent in the interglacial section, especially at the end of stage 5e where rapid oscillations of temperature are inferred. The extreme width of the latter part of stage 5 in core 26 is another example of this. These differences indicate additional, unresolvable changes in sedimentation

FIGURE 4

Signal and residual empirical orthogonal functions for the polar assemblage and five cores. The top set of curves are derived using age picks at Terminations I and II and the signal EOF (left) represents 67% of the variance. The bottom curves are determined by three age picks with the addition of the Barbados I event at 77 kybp. The signal EOF represents 82% of the variance, an improvement which is significant at the 95% confidence level.

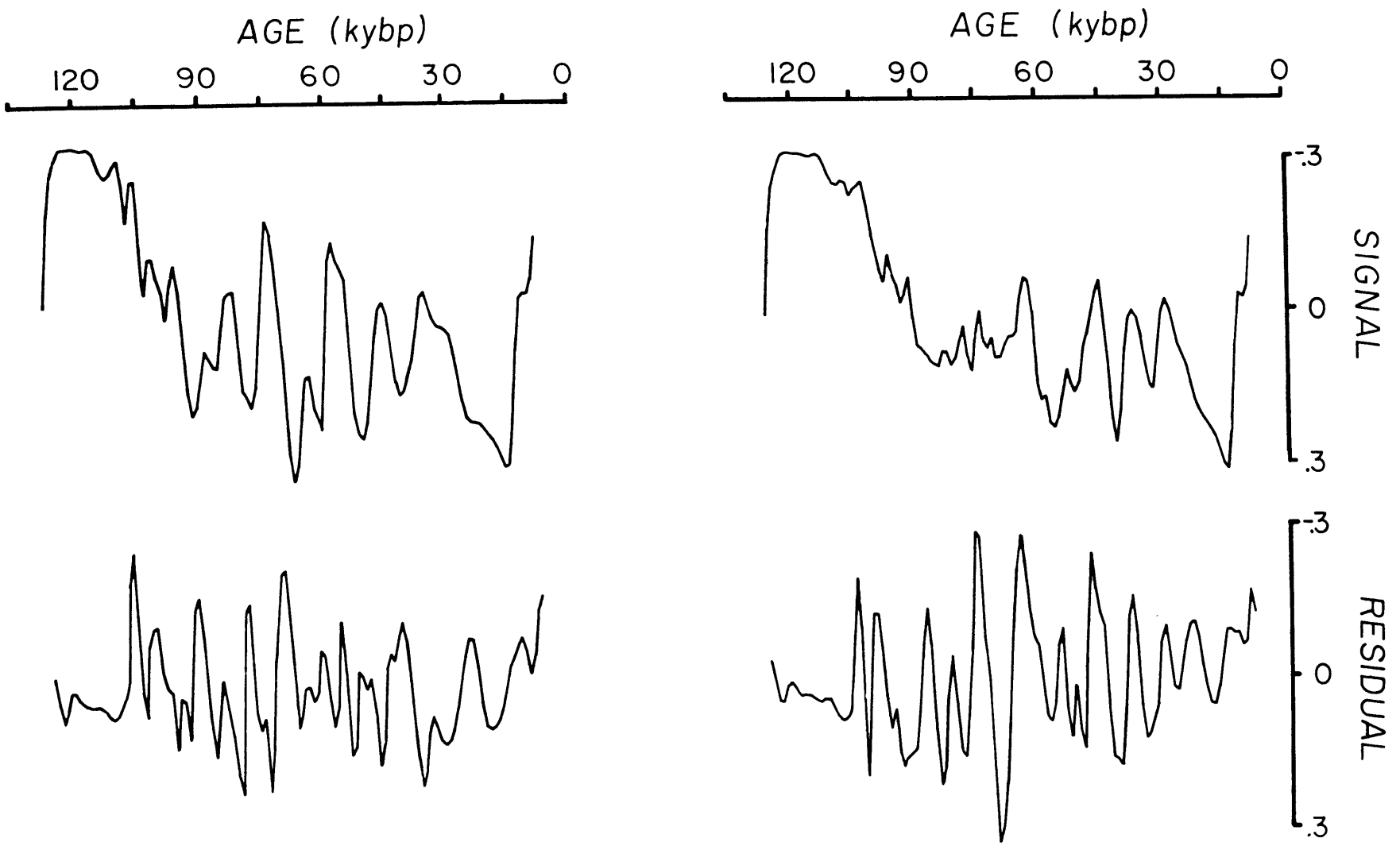
AGE (kybp)
120
90
60
30
0
AGE (kybp)
120
90
60
30
0
-.3
0
.3
SIGNAL
-.3
0
.3
RESIDUAL

FIGURE 5

Stratigraphic data of Figure 3 plotted against age using the three time horizons of Terminations I and II and the Barbados I event. See Figure 3 and the text for a discussion of the variables.

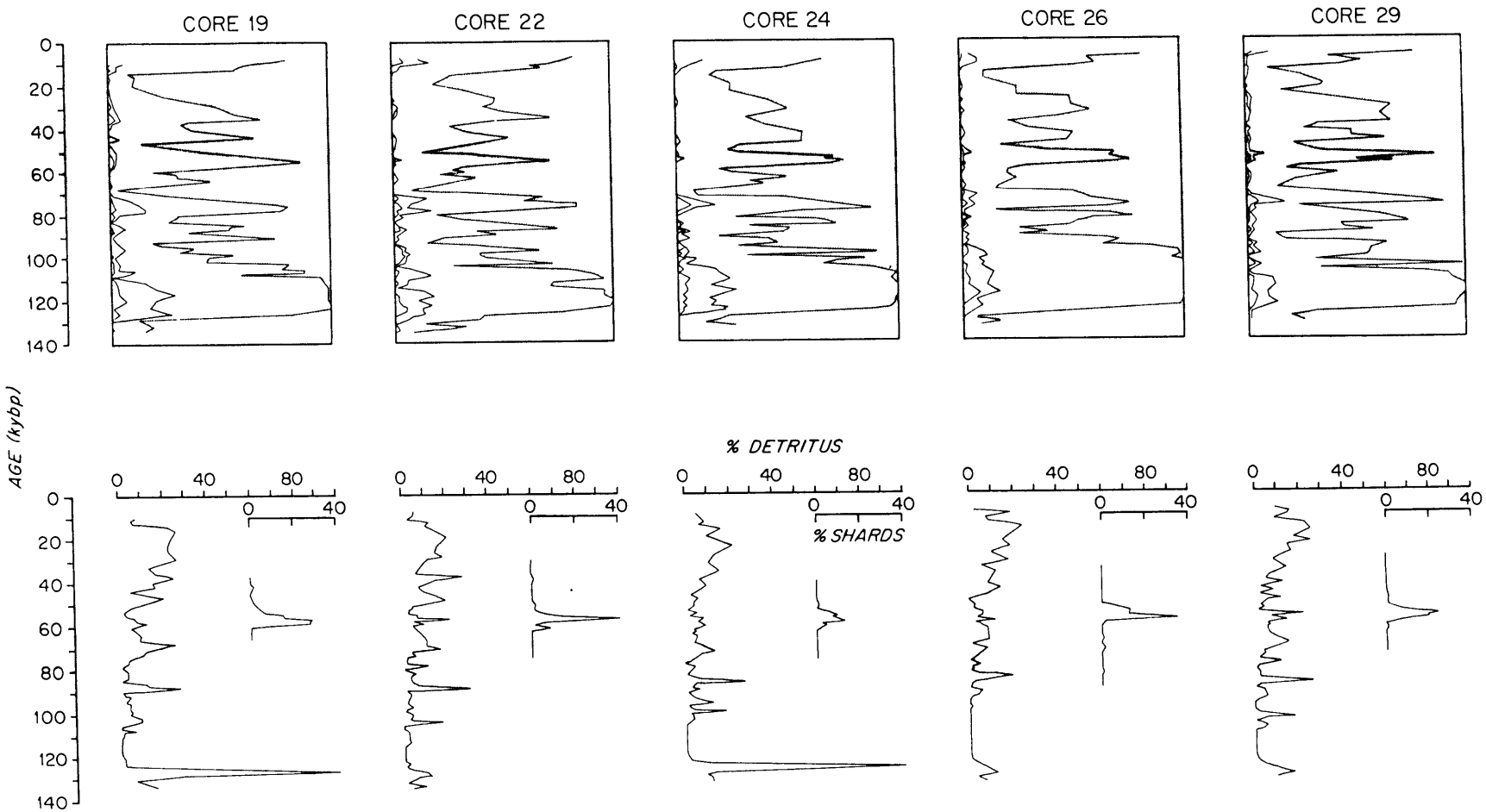
CORE 19
CORE 22
CORE 24
CORE 26
CORE 29
AGE (kybp)
0
20
40
60
80
100
120
140
% DETRITUS
% SHARDS
0
40
80
0
40

patterns which will be considered again in the spectral analysis section.

An additional check on the internal consistency of the data can be made by examining the location of the ash layer, which appears at 57 0.7 kybp. The inter-core scatter in the apparent age of this unit is much lower than the uncertainty in the dates listed in Table 2. It should be noted that Ruddiman and Glover (1972) place the age of this ash at 65 kybp using linear interpolation between Terminations I and II.

Figure 6 shows the sedimentation rates inferred for the five cores. The deposition rate is near 4 cm/ky in all five cores during glacial times. The scatter is much higher during interglacial times with sedimentation rates in the range of 5-9 cm/ky.

## 4. PALEOMAGNETIC DATA

Due to limitations of time, detailed paleomagnetic sampling was completed in the archive halves of four of the cores at 2.5 cm intervals. The core split half in its plastic liner was mounted in a specially designed holder and locked in place. A movable carriage which rigidly holds a miniature, nonmagnetic piston corer of 2.2 cm diameter was used to obtain 3 cm long plugs of sediment normal to the face of the core. Rotation of either the corer or its piston was prevented during all sampling operations. A 1 cm piece pf sediment from the core wall side of the plug was discarded to minimize the effect of wall drag. The remaining sediment was extruded into a nonmagnetic plastic sample box mounted in a special jig which controls sample orientation and rotation. Finally, the sample was potted in nonmagnetic polyester resin to prevent dessication and capped. The resin has a low heat of fusion, and any thermal remanent-magnetization imparted by it was negligible.

### 4.1 PILOT SAMPLE DEMAGNETIZATION

In order to establish a demagnetization program for the samples as well as to verify the magnetic stability of the sediment, frequent samples were selected for detailed study. A total of 46 pilot samples from the four cores were examined.

All magnetic measurements were made on a Superconducting Technology two-axis cryogenic rock magnetometer (Goree and Fuller, 1976). The

FIGURE 6

Age plotted against depth for the five piston cores using three age picks at Terminations I and II and the Barbados I event.

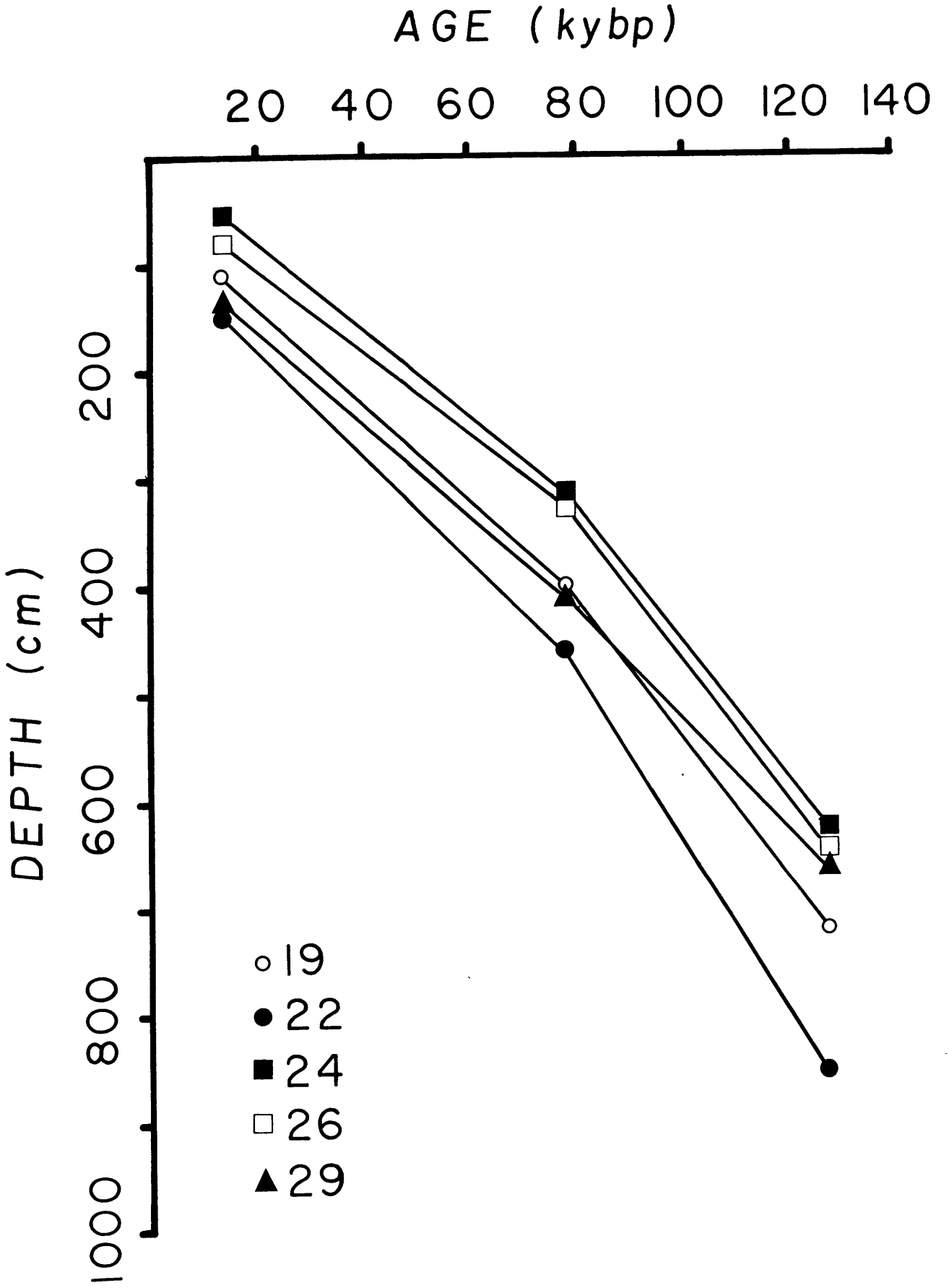
AGE (kybp)
20
40
60
80
100
120
140
DEPTH (cm)
200
400
600
800
1000
19
22
24
26
29

instrumental noise level was $3 \times 10^{-9}$ amp-$m^2$. Six back-to-back measurements were made on each specimen to minimize the effect of sample holder orientation error. All samples were treated twice at 25, 50, 100, 150, 200, 250, 300, 400, and 600 oe with the orientation reversed on alternate runs to reduce possible ARM contamination. The vector mean of the two measurements at each partial demagnetization step serves as an average for that step.

Table 3 lists the pilot sample locations and ages, median demagnetizing fields (MDF), and directional changes from demagnetization. The average median demagnetizing field for all samples is 315 oe with a standard deviation of 44 oe, while the mean directional change is $4.8 \pm 2.2^{o}$ over a 300 oe range. No correlation of either directional stability or MDF with climate or sediment lithology was detected.

Figure 7 shows a typical example of pilot demagnetization behavior. Directional change after the 200 oe step was minimal. The coercive force spectrum (slope of the magnetic moment demagnetization curve) is nearly flat over the range 100-400 oe, as is typical of marine sediments with a wide distribution of magnetic grain sizes. The remanence moment is high, exceeding the instrument noise level by two orders of magnitude. About 20% of the remanence remains after the final 600 oe treatment.

All pilot sample runs in the four cores indicated that 200 oe was an appropriate cleaning field. A program of demagnetization was chosen and all down-core samples were treated twice at 200 and 300 oe, plus a final 600 oe step. The 300 oe step serves as a check on the stability of each sample and is useful for a relative paleointensity estimate.

## 4.2 PILOT SAMPLE REMAGNETIZATION AND ARM NORMALIZATION

All of the pilot samples were remagnetized in a 0.2 oe coaxial field with a 600 oe, 60 Hz alternating field superimposed. The acquired ARM was then demagnetized using the six step program described previously. This procedure serves a dual purpose: normalization of the NRM to ARM is a measure of paleointensity and the ARM demagnetization behavior provides valuable information on the rock magnetism of the magnetic carriers.

The demagnetized NRM moment is not an adequate measure of

TABLE 3

PILOT SAMPLE DATA

| Sample | Age | Median Demagnetizing Field | Directional Change (degrees) NRM-200 | NRM-300 | NRM-600 |
|---|---|---|---|---|---|
| 19-150 | 23.0 | 385 | 3.3 | 3.5 | 2.7 |
| 19-192.5 | 32.2 | 318 | 7.7 | 7.1 | 4.7 |
| 19-220 | 38.1 | 363 | 7.1 | 7.3 | 5.5 |
| 19-250 | 44.6 | 332 | 1.8 | 1.8 | 8.0 |
| 19-300 | 55.4 | 363 | 3.8 | 3.1 | 3.0 |
| 19-325 | 60.8 | 345 | 3.2 | 3.7 | 2.2 |
| 19-345 | 65.1 | 370 | 3.0 | 3.2 | 2.2 |
| 19-365 | 69.4 | 340 | 5.6 | 4.4 | 4.0 |
| 19-400 | 77.0 | 346 | 2.5 | 2.6 | 1.7 |
| 19-450 | 84.7 | 281 | 2.4 | 2.1 | 2.0 |
| 19-490 | 90.8 | 365 | 1.7 | 2.0 | 2.1 |
| 19-525 | 96.2 | 324 | 2.7 | 2.2 | 2.0 |
| 19-565 | 102.3 | 371 | 2.4 | 1.6 | 2.6 |
| 19-600 | 107.7 | 347 | 1.4 | 1.6 | 3.7 |
| 19-650 | 115.3 | 261 | 5.1 | 5.3 | 3.2 |
| 19-700 | 123.0 | 248 | 5.0 | 6.7 | 6.1 |
| 22-280 | 40.2 | 235 | 4.8 | 5.4 | 20.8 |
| 22-340 | 52.3 | 325 | 4.8 | 4.0 | 2.5 |
| 22-375 | 59.4 | 323 | 5.3 | 5.8 | 12.4 |
| 22-430 | 70.5 | 307 | 7.8 | 8.4 | 19.3 |
| 22-460 | 76.5 | 297 | 6.6 | 7.7 | 8.2 |
| 22-500 | 81.7 | 289 | 6.1 | 6.9 | 5.4 |
| 22-540 | 86.7 | 289 | 8.6 | 9.6 | 10.8 |
| 22-730 | 110.5 | 278 | 6.0 | 7.1 | 9.6 |
| 22-750 | 113.0 | 277 | 6.5 | 8.5 | 10.1 |
| 22-825 | 122.4 | 285 | 9.0 | 9.9 | 10.4 |
| 26-295 | 68.9 | 397 | 4.5 | 5.8 | 9.4 |
| 26-325 | 76.5 | 349 | 2.8 | 3.0 | 3.1 |
| 26-355 | 81.3 | 273 | 4.3 | 4.3 | 1.5 |
| 26-375 | 84.4 | 315 | 5.3 | 5.8 | 9.4 |
| 26-410 | 89.8 | 329 | 0.9 | 2.2 | 2.5 |
| 26-437.5 | 94.1 | 349 | 3.3 | 3.1 | 2.6 |
| 26-475 | 99.9 | 289 | 7.2 | 7.8 | 6.3 |
| 26-532.5 | 108.8 | 303 | 4.5 | 5.0 | 5.6 |
| 26-600 | 119.3 | 256 | 3.0 | 3.3 | 3.0 |
| 26-630 | 123.9 | 288 | 5.4 | 6.2 | 8.2 |
| 29-260 | 42.4 | 253 | 4.6 | 5.0 | 5.6 |
| 29-310 | 53.9 | 357 | 2.2 | 2.2 | 2.7 |
| 29-360 | 65.5 | 353 | 3.1 | 6.9 | 5.2 |
| 29-405 | 75.8 | 279 | 2.9 | 3.4 | 2.9 |
| 29-480 | 90.6 | 393 | 2.8 | 3.2 | 2.9 |
| 29-537.5 | 101.8 | 358 | 3.2 | 3.5 | 3.3 |
| 29-555 | 105.2 | 328 | 4.0 | 5.2 | 5.6 |
| 29-575 | 109.0 | 264 | 3.6 | 4.0 | 3.9 |
| 29-625 | 118.7 | 241 | 4.8 | 5.2 | 8.9 |
| 29-670 | 127.8 | 263 | 3.7 | 4.3 | 1.2 |

FIGURE 7

Typical pilot sample demagnetization curves. The demagnetization intensity curve shows a flat coercive force spectrum from 150-400 oe. The directional data are stable after the 200 oe step. The ARM demagnetization curve is also shown.

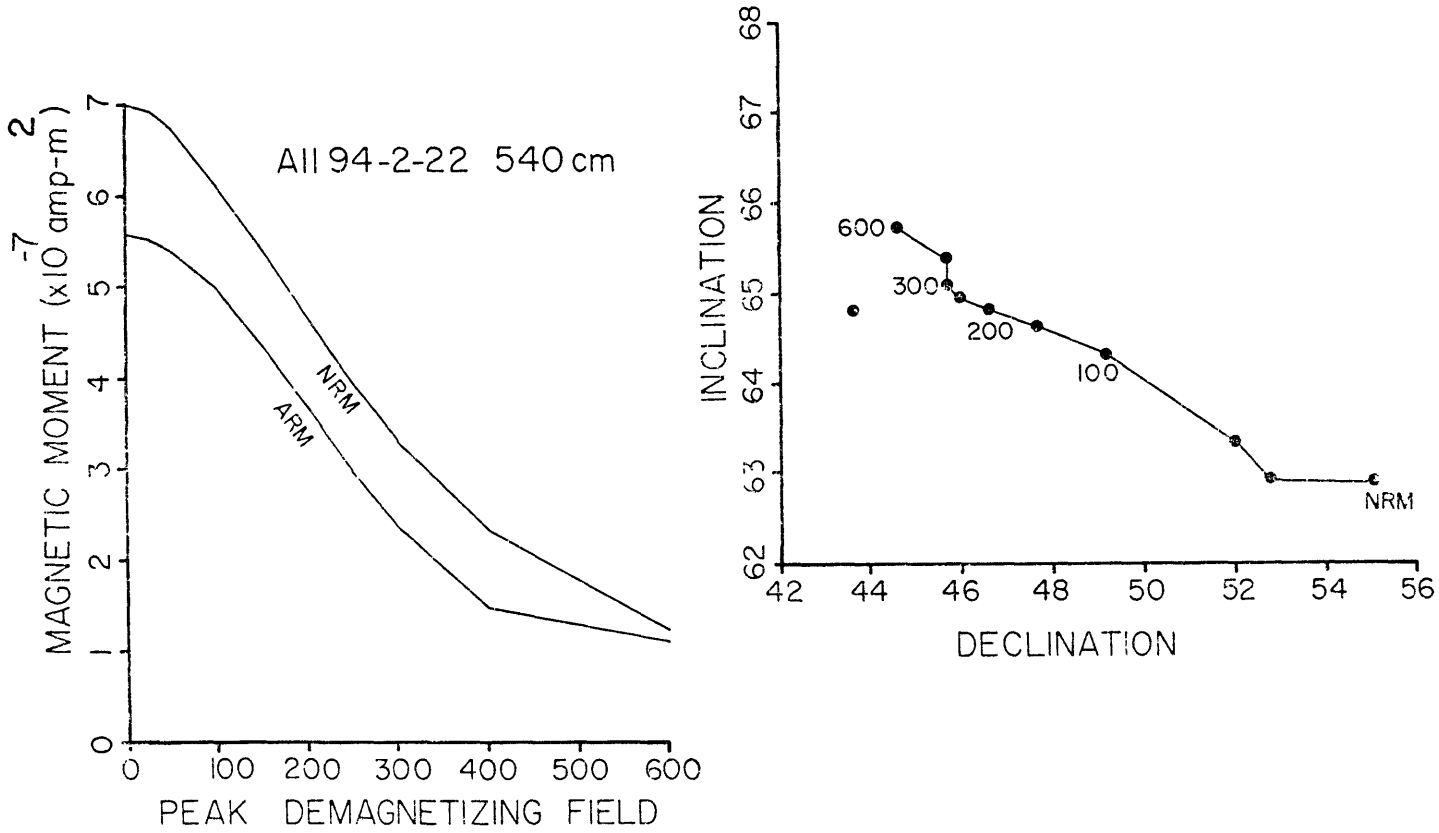
All 94-2-22 540 cm
MAGNETIC MOMENT (x10^-7 amp-m^2)
NRM
ARM
0
1
2
3
4
5
6
7
0
100
200
300
400
500
600
PEAK DEMAGNETIZING FIELD
INCLINATION
62
63
64
65
66
67
68
42
44
46
48
50
52
54
56
DECLINATION
600
300
200
100
NRM

paleofield intensity due to the possibility of variation of the concentration and mineralogy of the magnetic minerals with time. The mineral composition and terrigenous fraction of North Atlantic sediments is controlled by climate (Ruddiman and McIntyre, 1976). The resulting down-core changes in magnetic mineral concentration and NRM moment have led to correlations of the field intensity with the orbital parameters of the earth (Wollin et al., 1978) that are spurious (Chave and Denham, 1979).

Various bulk magnetic properties have been used to normalize NRM and remove concentration effects from intensity data. ARM is the only one of these quantities which does not overemphasize the contributions of less stable multidomain grains (Johnson et al., 1975; Levi and Banerjee, 1976). It is most important that the particular normalizing parameter activate the same coercive force spectrum as the NRM. Careful demonstration of this correspondence also serves as an important check on magnetic stability: different demagnetization behavior of the NRM and ARM is suggestive of post-depositional chemical alteration and probably invalidates any paleointensity estimate. It should be noted that normalized NRM is only a relative paleointensity value, and no way to obtain absolute paleointensity from sediments exists.

Figure 7 shows a typical demagnetization curve from the pilot data. The coercive force spectrum of the ARM is similar to that of the original remanence, as demonstrated by the nearly identical slopes of the curves. After demagnetization of the ARM at 600 oe the magnetic vector is within a few degrees of the final demagnetized NRM.

Levi and Banerjee (1976) normalized NRM to ARM at the same level of partial demagnetization. We have chosen to normalize partial NRM to partial ARM by taking the ratio of the vector differences between two selected demagnetization steps. Unless the resulting pNRM/pARM curve is independent of the demagnetizing fields actually used and the additivity of partial demagnetization is established the method is suspect. Figure 8 shows the pNRM/pARM behavior of a pilot sample as a function of initial and final demagnetizing fields. Any choice of steps between 150 and 400 oe produces a similar relative paleointensity with a scatter of about 10%. We selected the 200 and 300 oe

FIGURE 8

The pNRM/pARM behavior of the pilot sample of Figure 7 as a function of the partial demagnetizing fields. The pNRM/pARM ratio is derived by vector subtracting the NRM and ARM data at two partial demagnetizing steps and dividing to obtain the ratio. The first partial demagnetizing field is shown by the symbol while the final one is indicated on the horizontal axis.

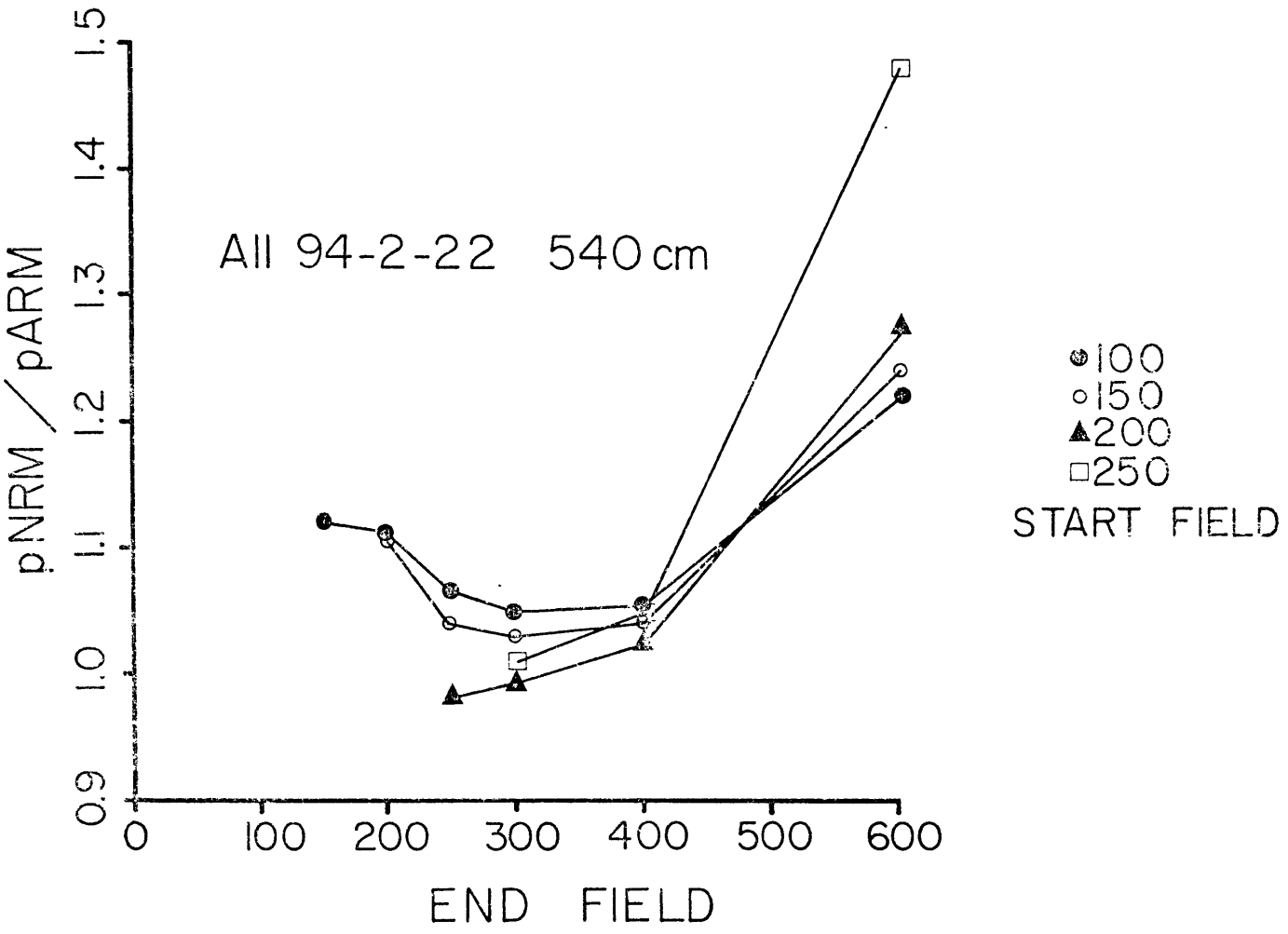
All 94-2-22 540 cm
pNRM / pARM
0.9
1.0
1.1
1.2
1.3
1.4
1.5
0
100
200
300
400
500
600
END FIELD
100
150
200
250
START FIELD

demagnetization steps to produce a down-core measure of relative paleointensity. The same demagnetization treatments were applied to both the original and artificial remanences for a total of twelve steps per specimen.

## 4.3 PALEOMAGNETIC TIME SERIES

Various sections of the four cores were sampled for continuous paleomagnetic measurements. An initial attempt was made to cover the last interglacial interval due to the higher sedimentation rate and potentially improved temporal resolution of the magnetic record. This time sequence was extended into the glacial epoch in three of the cores. After the twelve measurements were carried out, each sample was assigned an age using the stratigraphic control of section 3.

Coring disturbance was noted in some cores at the breaks between sections of plastic core liner. These interruptions took the form of large changes in declination near the section breaks and were treated as wild points and deleted. Some differential motion of the plastic core liners occured in spite of the use of locking bolts. The core orienting device compass indicated slight twisting of the corer during penetration. Least squares straight lines were fit to the declination data by core section and removed if the slope of the line was statistically significant. In general, only the lowermost core sections required this treatment. The mean declination per section was then set to a constant value, the average value indicated by the compass, to correct for differential rotation of the liners.

The corrected time series were interpolated to even 500 year samples using a natural cubic spline function. The directional data were treated by interpolation of the direction cosines, as suggested by Parker and Denham (1979). The final inclination and declination curves appear as Figure 9. The paleointensity data were interpolated separately and plotted as Figure 10. Dotted lines indicate long data gaps where the interpolated result is artificial.

Visual correlation of the directional data is fair in the interval prior to 77 kybp. The directions vary slowly in the interval 25-77 kybp and have a much higher frequency content at older times, making curve matching difficult. The paleointensities are smooth with a

FIGURE 9

Interpolated directional data plotted against age for the four cores. The treatment of the declination data is discussed in the text. Dotted lines indicate long data gaps where the interpolated result is suspect. The horizontal dashed lines separate the data sections used for the spectral analysis.

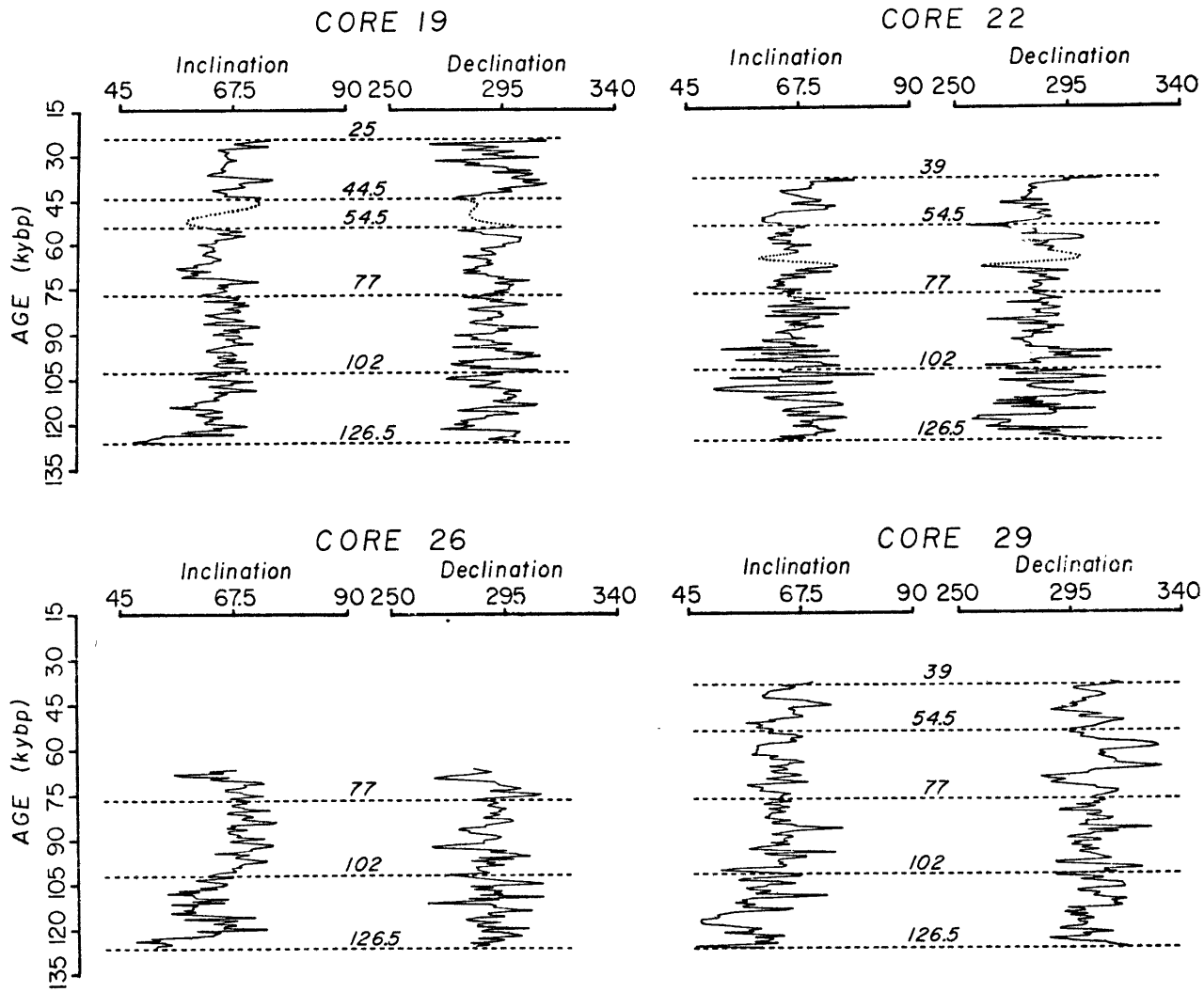
CORE 19
Inclination
Declination
45
67.5
90
250
295
340
AGE (kybp)
15
30
45
60
75
90
105
120
135
25
44.5
54.5
77
102
126.5
CORE 22
Inclination
Declination
45
67.5
90
250
295
340
39
54.5
77
102
126.5
CORE 26
Inclination
Declination
45
67.5
90
250
295
340
AGE (kybp)
15
30
45
60
75
90
105
120
135
77
102
126.5
CORE 29
Inclination
Declination
45
67.5
90
250
295
340
39
54.5
77
102
126.5

FIGURE 10

Relative paleointensities plotted against age. The dotted lines indicate long gaps in the data where the interpolated result is suspect. See text for details of the calculation.

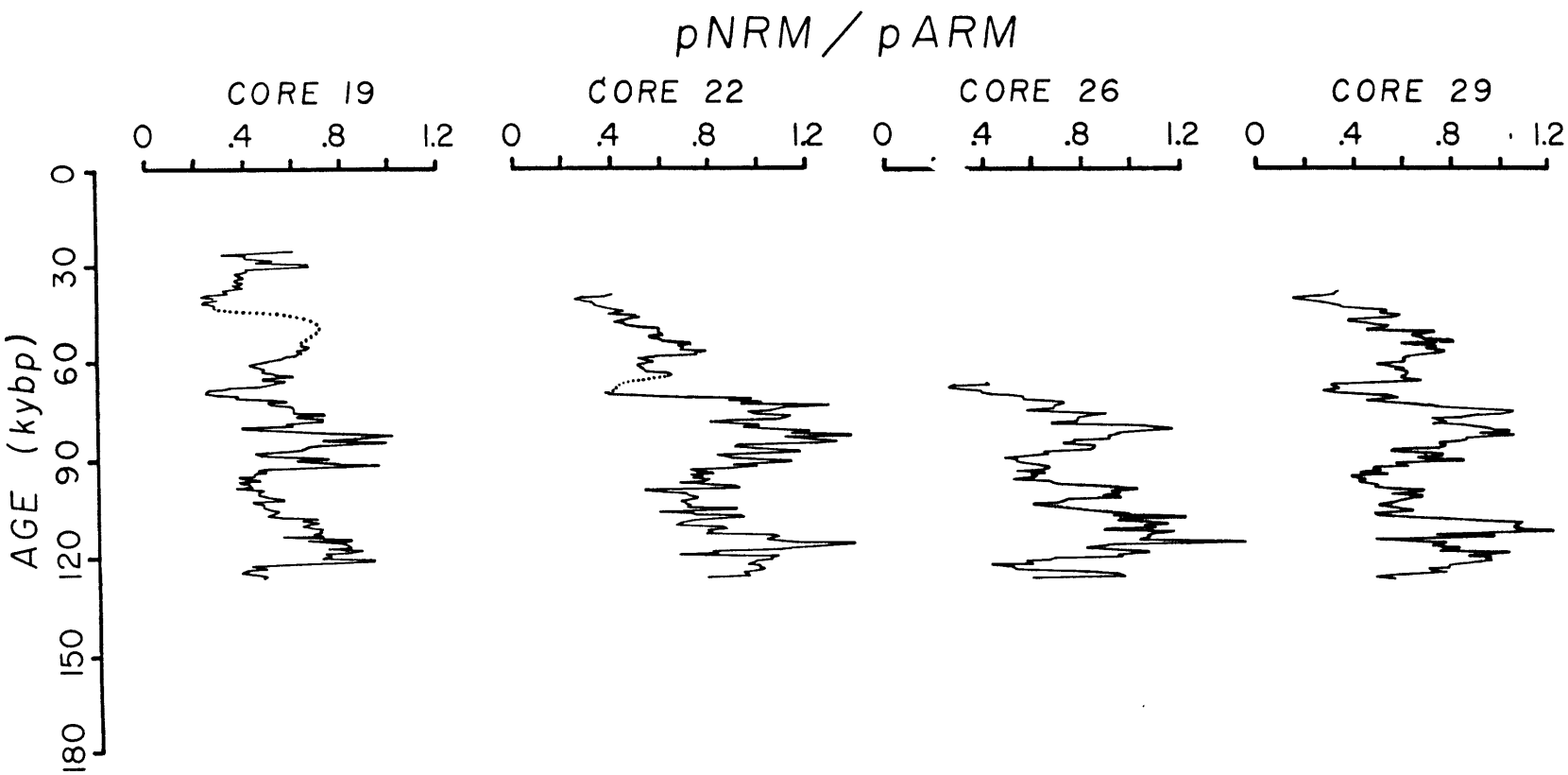
pNRM / pARM
CORE 19
CORE 22
CORE 26
CORE 29
0
.4
.8
1.2
AGE (kybp)
0
30
60
90
120
150
180

dominant low frequency signal that correlates well from core-to-core.

The mean declination values of about 290° in Figure 9 are markedly lower than the present day value of 335°. The mean inclinations are lower than both the axial dipole value of 71.4° and the present day value of 70.5°. The VGP for the mean inclination and declination is located in central North America for all four cores, and it is unlikely that the ancient geomagnetic pole differed by this much from the present day one. Some systematic error in the core orienting process is suspected, and analysis of VGP paths is not feasible. Spectral analysis of the directions themselves will not be affected since we will project them about the mean.

## 5. SPECTRAL ANALYSIS

### 5.1 SPECTRAL ANALYSIS TECHNIQUES

Estimation of the second order statistics of a sampled, band-limited, stationary time sequence is a classical problem of time series analysis. Several different approaches to the calculation of power spectra exist and are divided into two classes: linear and nonlinear spectral estimation techniques. The former include the autocorrelation or Blackman-Tukey method and direct calculation using the discrete Fourier transform. These two computational methods require unreasonable assumptions about the data: the autocorrelation technique makes the data zero outside of the observation window and the direct approach makes the observed data periodic in time. Both approaches require the use of a weighting function that is independent of the statistical properties of the process under study. This is equivalent to viewing the true power spectrum through a window which distorts and smears it. For long time series with many cycles of the process under study no serious bias results, but short realizations require other approaches.

The nonlinear spectral analysis methods avoid many of the limitations of conventional time series analysis. They are data adaptive, in the sense that the window through which the true spectrum is viewed is calculated from the data. An excellent review of the field is contained in Haykin (1979). We have applied the maximum entropy method (MEM) of Burg (1975) to the paleomagnetic directions of this study. MEM power spectra are marked by two important properties: greatly

improved resolution and smoothness of the spectral estimates. These characteristics make the MEM useful in studying deterministic processes, although the technique is not limited to them.

The MEM spectrum is that subset of an infinite number of spectral estimates that corresponds to the most random or unpredictable time series that is consistent with the known autocorrelation values. Van den Bos (1971) established the equivalence of least squares fitting of an autoregressive (AR) model to data and application of the MEM algorithm. AR processes are not the most general models for time series, but are easy to calculate.

Burg (1975) derived the MEM spectrum from a general variational principle and presented several algorithms for their computation. A more heuristic approach will be outlined here. An AR process is modelled as a linear feedback filter excited by white noise. The mathematical description of such a model is:

$$y_t = \sum_{p} -\alpha_i y_{t-i} + x_t \qquad (1)$$

where $y_t$ is the data, predicted from its p past values, and $x_t$ is a white noise process with variance $\sigma^2$. To obtain the spectrum from (1) we calculate the Z transform:

$$Y(z) = X(z)/(1 + \sum_{i=1}^{p} \alpha_i z^i) \qquad (2)$$

The form of (2) illustrates the all pole or feedback nature of AR models and explicitly indicates that the output Y is determined by exciting the filter with white noise. The power spectrum of Y is obtained by evaluation of (2) on the unit circle with $z = e^{i2\pi f}$ and f the frequency to be examined:

$$S(f) = \sigma^2 / \left| \sum_{k=0}^{p} \alpha_k e^{i2\pi kf} \right|^2 \qquad (3)$$

where $\alpha_0 \equiv 1$ and f lies in the Nyquist band. The coefficients $\alpha_i$ are the elements of a prediction error filter (PEF) which can be calculated either from the data or its autocorrelation function.

## 5.2 DETERMINATION OF THE PEF LENGTH

An important step in applying the MEM to data is determination of the order p of the AR process (1) or,equivalently, the length of the

PEF. Too few terms in the PEF results in poor spectral resolution while too many terms can result in spurious detail in the spectrum. Choice of the optimum PEF length results in a good trade-off between resolution and stability of the spectral estimate. A number of objective PEF length criteria have been proposed, but in practical cases additional, more subjective, approaches are sometimes necessary.

An important concept in PEF theory is the error power. A PEF predicts a given data point from past values of the data, and the mean squared difference between the observed and predicted values is the error power. As the length of the filter increases, the error power decreases monotonically.

The final prediction error (FPE) criterion was proposed by Akaike (1969) and applied by Ulrych and Bishop (1975). It is an estimate of the prediction error to be expected if the PEF is applied to a new and independent observation of the same physical process. For an N point sample of a zero mean process with a p point PEF the FPE is given by:

$$FPE(p) = ((N + p + 1)/(N - p - 1))E_p \qquad (4)$$

where $E_p$ is the pth error power.

A second length criterion is an information theoretic one also suggested by Akaike (1974). It is based on minimization of the log likelihood function for the model and has the form:

$$AIC(p) = \ln(E_p) + 2p/N \qquad (5)$$

The third criterion to be applied was derived by Parzen (1974). He assumed that the true time series was infinite order AR in form and found that finite order approximation which minimized the mean squared difference between the two. The quantity is known as the criterion autoregressive transfer function or CAT:

$$CAT(p) = (\sum_p (N-p)/NE_p)/N - ((N-p)/NE_p) \qquad (6)$$

All three of these filter length criteria have a minimum value at the optimum value of p.

If all three quantities yield the same value for p, then the application of the MEM to data becomes automatic. For short data sections we found that all underestimate the true AR order. A heuristic approach to the selection of the PEF length using the behavior of the roots of the filter was taken. The spectral peaks in

(3) occur near the roots of the polynomial (2) and the distance of the roots from the unit circle determines the resolution and power level. As the root approaches the unit circle, the spectral peaks are sharper and the Z transform root approaches the true peak frequency. Experiments with artificial time series show that the unit circle distance approaches a constant when the correct AR order is reached and the PEF has the correct length. Spurious line splitting at too high an order is easily identified as it is accompanied by motion of the roots away from the unit circle.

Figures 11 and 12 illustrate our PEF selection procedure for a section of directional data from core 29 covering the interval 54.5-77 kybp. The data set consists of 45 data points. Figure 11 shows the normalized FPE, AIC, and CAT criteria as a function of PEF length. The minimum of all quantities occurs at p = 5, but the spectrum is featureless and broad. Figure 12 shows the unit circle distance for the two largest peaks for the same data section. Both approach a nearly constant value at 9 PEF terms. One of the peaks splits at 11 terms, accompanied by abrupt motion away from the unit circle. Examination of the MEM spectra as a function of PEF length confirms that 9 or 10 terms produces the sharpest and most complete spectra. Typically, a PEF length near 20% of the time series length was required for all data sections, much longer than suggested by the FPE, AIC, or CAT criteria.

## 5.3 SPECTRA OF PALEOMAGNETIC DIRECTIONS

The directional data of Figure 9 were divided into short sections of about 20 ky duration, as shown by the horizontal lines in the figure. The linear detrending operation applied to the declination data for each core section makes the analysis of longer time series risky due to the possible addition of spurious components. Figure 9 also suggests that the spectral nature of the directions changes with age, and this is easily detected by examining short sections. Figure 9 shows two long gaps in the data which should be avoided.

Inclination and declination are one representation of points on the unit sphere. A region of the unit sphere can be approximated as a plane using a map projection such as the stereographic type. This

FIGURE 11

Normalized length criteria for a 45 point long set of complex equivalent paleomagnetic directions from core 29 covering the interval 54.5-77 kybp. All of these quantities have a minimum value at 5 terms in the PEF.

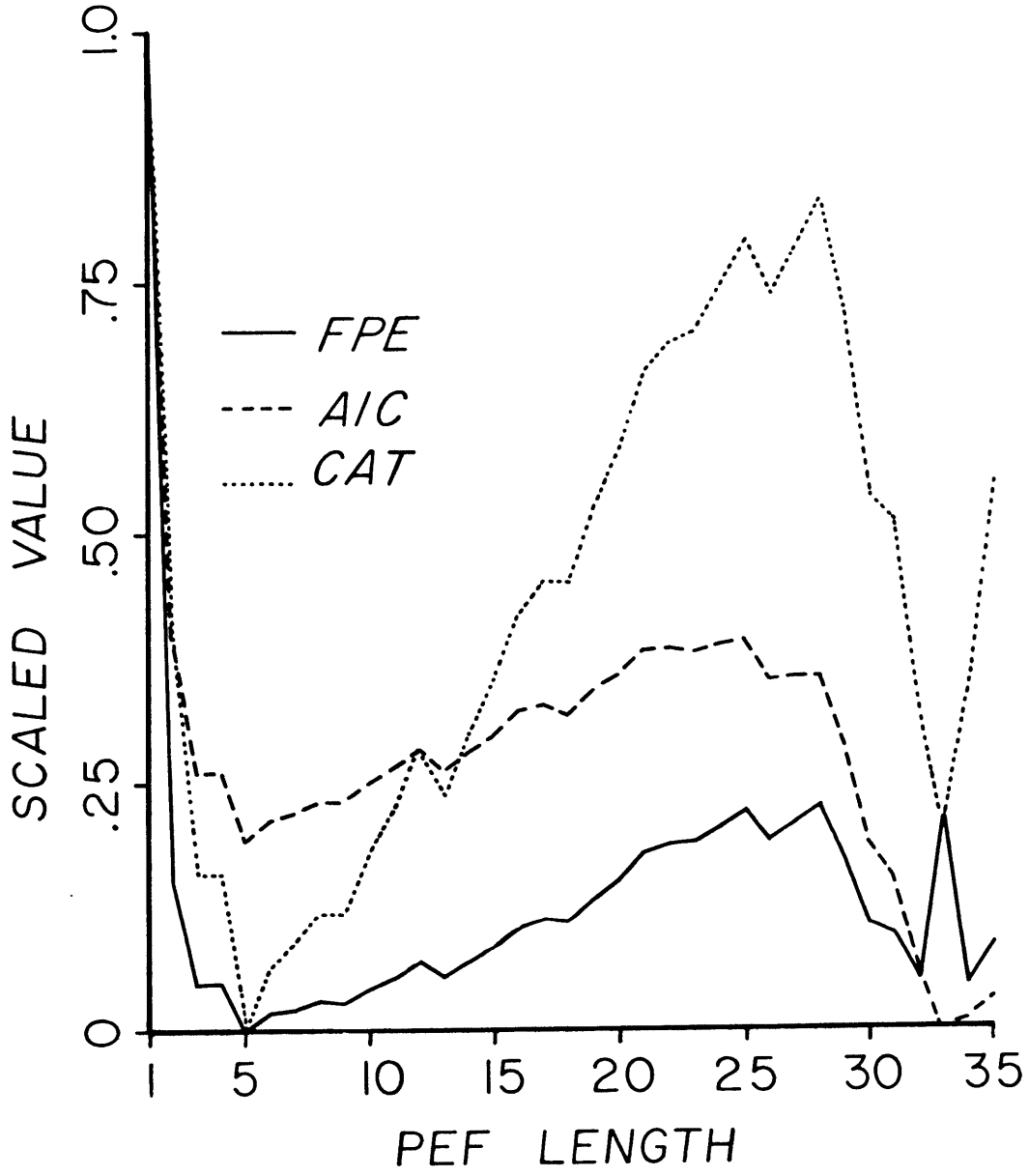
SCALED VALUE
1.0
.75
.50
.25
0
FPE
AIC
CAT
1
5
10
15
20
25
30
35
PEF LENGTH

FIGURE 12

Distance of the main two roots of the PEF from the unit circle using the same data as in Figure 11. The lower solid line represents a spectral peak centered near 7 ky. The upper solid line represents a spectral peak centered near -15 ky which splits into two peaks at 11 terms in the PEF.

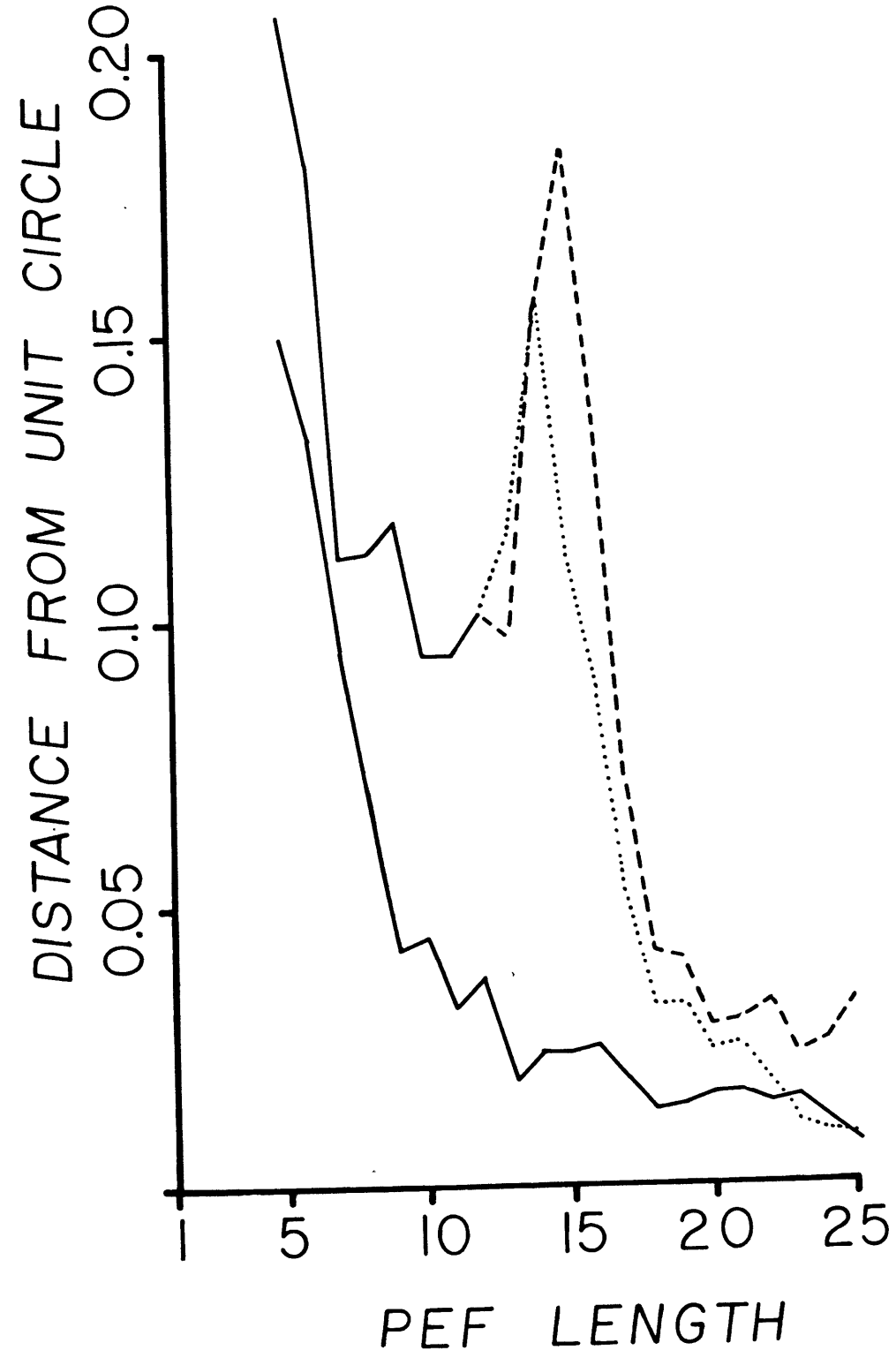
DISTANCE FROM UNIT CIRCLE
0.05
0.10
0.15
0.20
1
5
10
15
20
25
PEF LENGTH

procedure reduces the time series of directions to a sequence of complex numbers which can be analyzed using scalar time series techniques (Denham, 1975). The projection pole can be chosen arbitrarily, but it is convenient to use the mean direction for each core so that the process is of zero mean type.

Power spectral analysis of complex time series reveals both the magnitude and direction of each frequency component of the time series. Clockwise circular motion is described by positive frequencies and no negative frequency part. Elliptical motion appears as unequal magnitude peaks at the appropriate positive and negative frequency. As the ellipse approaches a straight line, the two peaks approach similar magnitudes and the time series becomes real rather than complex. These observations can be applied to paleomagnetic data to determine the dominant direction of motion of the ancient field vector.

After performing the complex mapping for each core and time section, the correct PEF length was determined using the procedure of section 5.2. A PEF length of 9-11 terms was appropriate for all cases. The spectrum of the PEF was calculated using (3). Since several independent realizations of each time band were available, the data were stacked to yield a composite spectrum. Common features in the separate cores will appear as large, sharp peaks.

MEM spectra must be interpreted with caution as visual appearance is often misleading. The power in a given spectral band is proportional to the area under a peak rather than the peak height (Lacoss, 1971). This means that a sharp, narrow peak may actually contain less power than a broader but smaller one. The distance of a pole of the PEF from the unit circle determines both the power in and resolution of a given spectral feature and the trade-off between these quantities is not simple. The integrated power spectrum can be displayed as a cumulative sum and used to find the power within a frequency band. This avoids many of the problems in using raw power spectra for quantitative geophysical interpretations.

Since the MEM is a nonlinear spectral estimator, the calculation of uncertainty on the spectrum is a complex and poorly understood problem. We have arbitrarily chosen to consider only those frequency bands containing at least 10% of the total power as significant.

These bands appear as steep line segments in the integrated power spectrum, corresponding to the largest peaks in the composite power spectrum. Table 4 lists those major features of the stacked power estimates in Figure 13. The number of spectral estimates in each composite spectrum is listed in the table.

The first time slice, 25-44.5 kybp, is dominated by a negative peak near 10.5 ky in period with two smaller positive features centered on 6.5 and 2 ky. Overlap between the bands is not large, suggesting several independent processes in the ancient field. The power spectrum is indicating slow counter-clockwise looping of the field vector modulated by two more rapid and clockwise signals. It should be noted that only one core is used to find this spectrum, and no check on its reliability is possible.

The next time section shows simpler paleofield behavior with only two positive and negative frequency components at about 11.5 ky period. The field vector followed an elongate, clockwise path with positive to negative power in the ratio of 1.3:1. The following time slice, 54.5-77 kybp, marks a return to slightly more complex field behavior. The clockwise component, with a period near 6.5 ky, is modulated by a counter-clockwise component at 13 ky. These frequency bands contain similar amounts of power, but do not overlap significantly.

The final two data sections cover the interval 77-126.5 kybp. The spectral estimates for these times are not reliable, with different cores giving markedly different results. This is reflected in the rough and irregular nature of the last spectra of Figure 13. The data in Figure 9 also show a dramatic change in appearance near 77 kybp with a reduced visual correlation and higher frequency character.

## 6. DISCUSSION

The replicate set of directional spectra of the last section display the importance of making repetitive measurements at a single site. The unusable data in the interglacial part of the record can only be detected by this procedure. The magnetic stability of the bad sections is indistinguishable from the more recent material, and an explanation for the poor results either in the time control or in post-depositional disturbance must be sought.

TABLE 4

PRINCIPAL SPECTRAL BANDS

| Age | Cores | Period-low | Period-high | % Power |
|---|---|---|---|---|
| 25-44.5 | 19 | -15.8 | -7.6 | 31.3 |
| | | 10.5 | 4.9 | 19.9 |
| | | 2.12 | 1.79 | 17.2 |
| 39-54.5 | 22,29 | 14.1 | 9.1 | 36.5 |
| | | -18.1 | -5.3 | 28.8 |
| 54.5-77 | 19,22,29 | 10.0 | 6.7 | 28.5 |
| | | -23.0 | -8.8 | 25.1 |
| 77-102 | All | 12.7 | 3.3 | 20.9 |
| | | 1.68 | 1.38 | 16.1 |
| | | -1.50 | -1.03 | 13.9 |
| | | -8.2 | -5.6 | 12.6 |
| 102-126.5 | All | 36.0 | 8.2 | 31.8 |
| | | 36.0 | -4.9 | 27.9 |

FIGURE 13

Maximum entropy power spectra of the complex paleomagnetic directions for five time sections in the interval 25-127 kybp. Dominant positive frequency spectral peaks represent clockwise looping of the magnetic field vector. The five stacked spectra cover 25-44.5 kybp (1), 39-54.5 kybp (2), 54.5-77 kybp (3), 77-102 kybp (4), and 102-126.5 kybp (4). The numbers in parentheses correspond to the number of spectral estimates that were averaged to obtain the composite spectra.

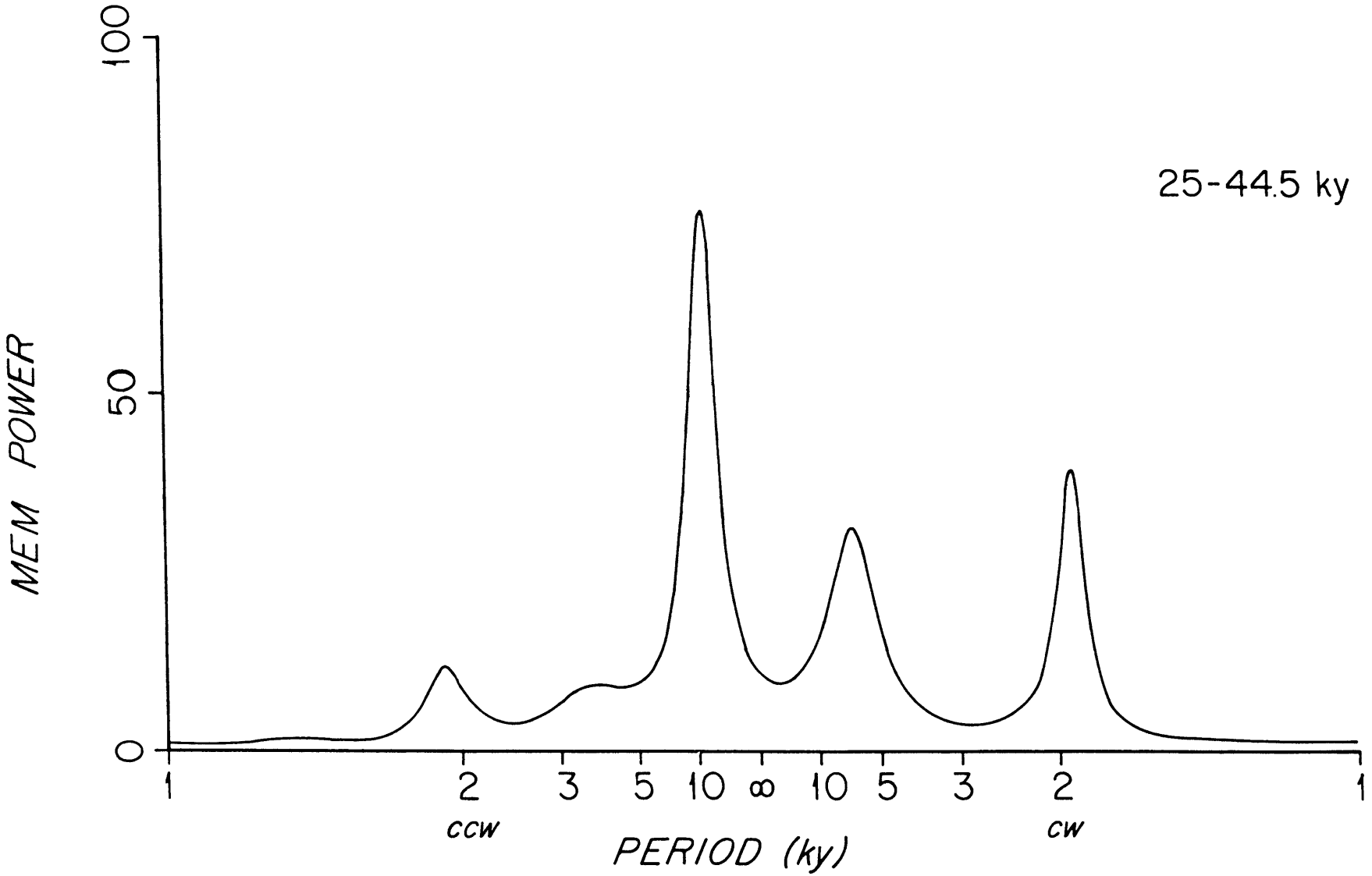
MEM POWER
100
50
0
25-44.5 ky
1
2
3
5
10
∞
10
5
3
2
1
ccw
cw
PERIOD (ky)

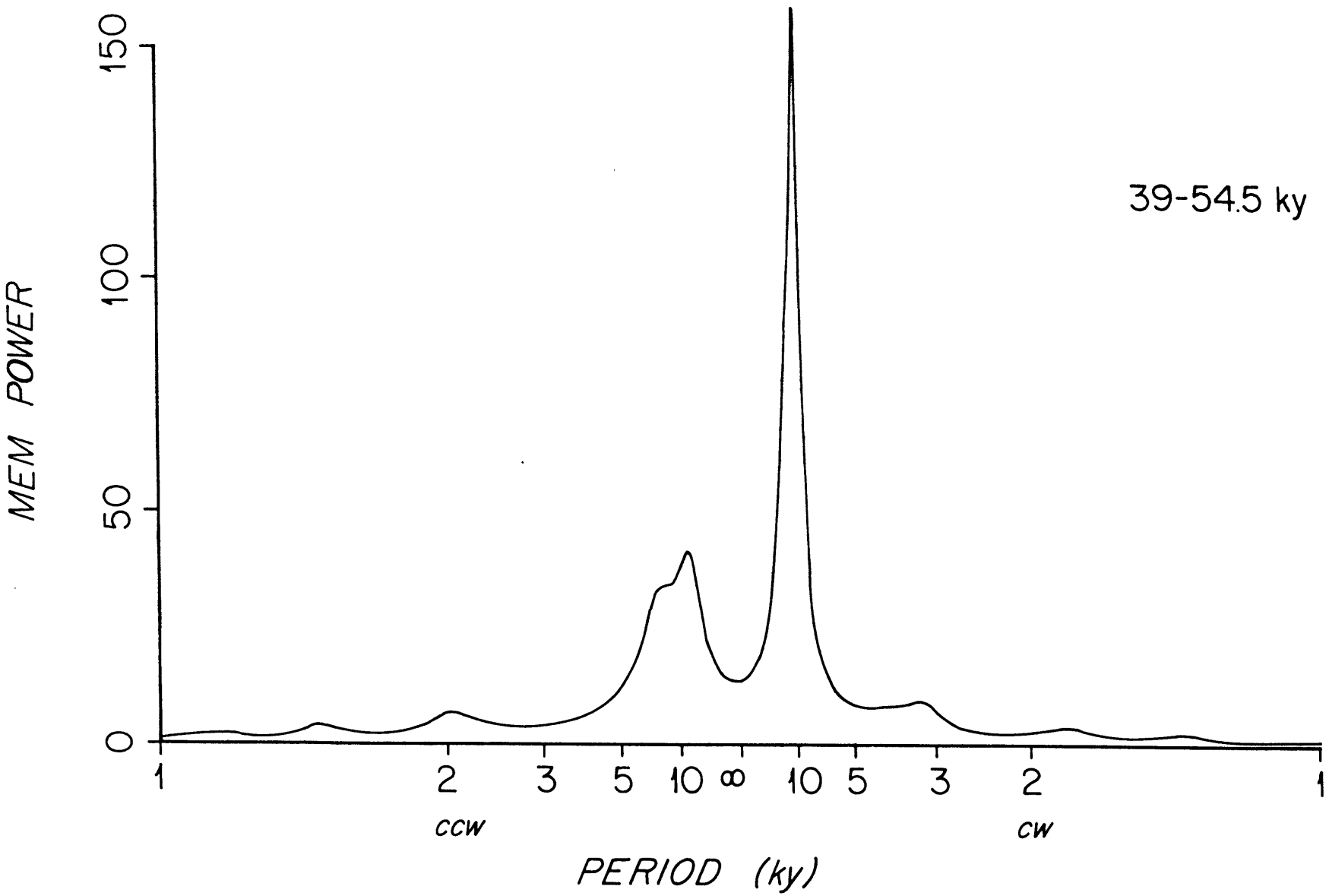
MEM POWER
150
100
50
0
39-54.5 ky
1
2
3
5
10
∞
10
5
3
2
1
ccw
cw
PERIOD (ky)

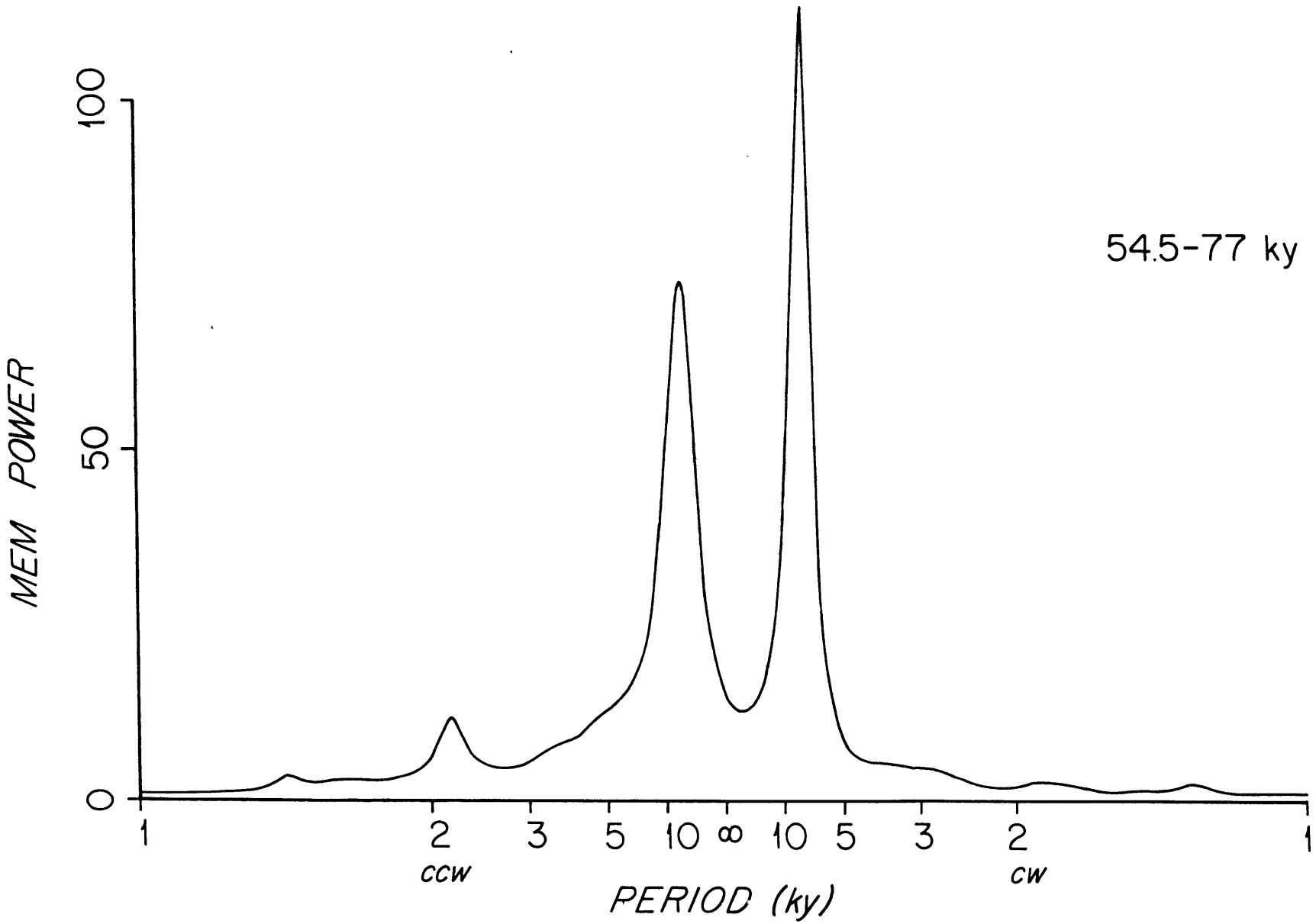
54.5-77 ky
MEM POWER
100
50
0
1
2
3
5
10
∞
10
5
3
2
1
ccw
cw
PERIOD (ky)

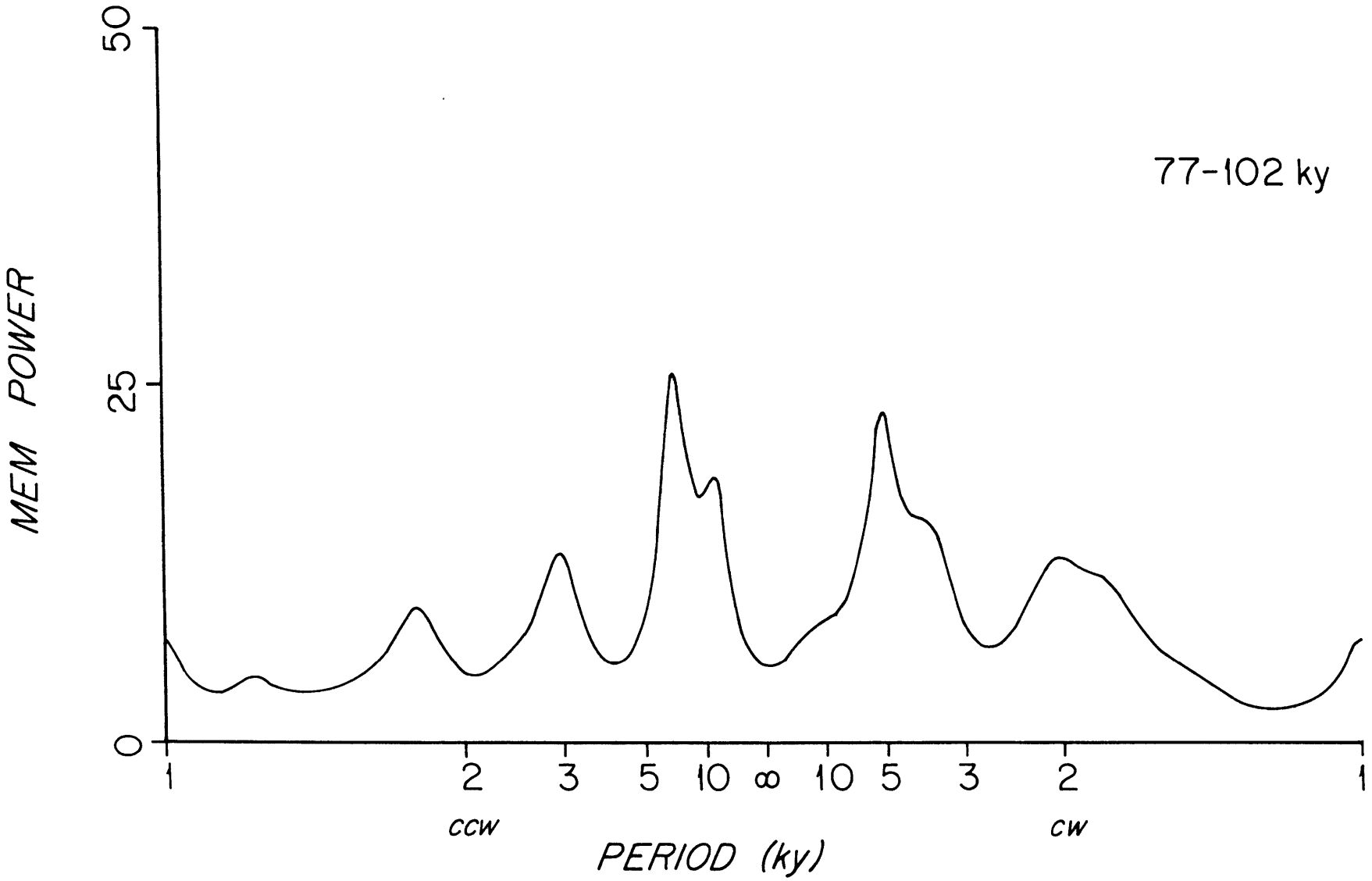
77-102 ky
MEM POWER
50
25
0
1
2
3
5
10
∞
10
5
3
2
1
ccw
cw
PERIOD (ky)

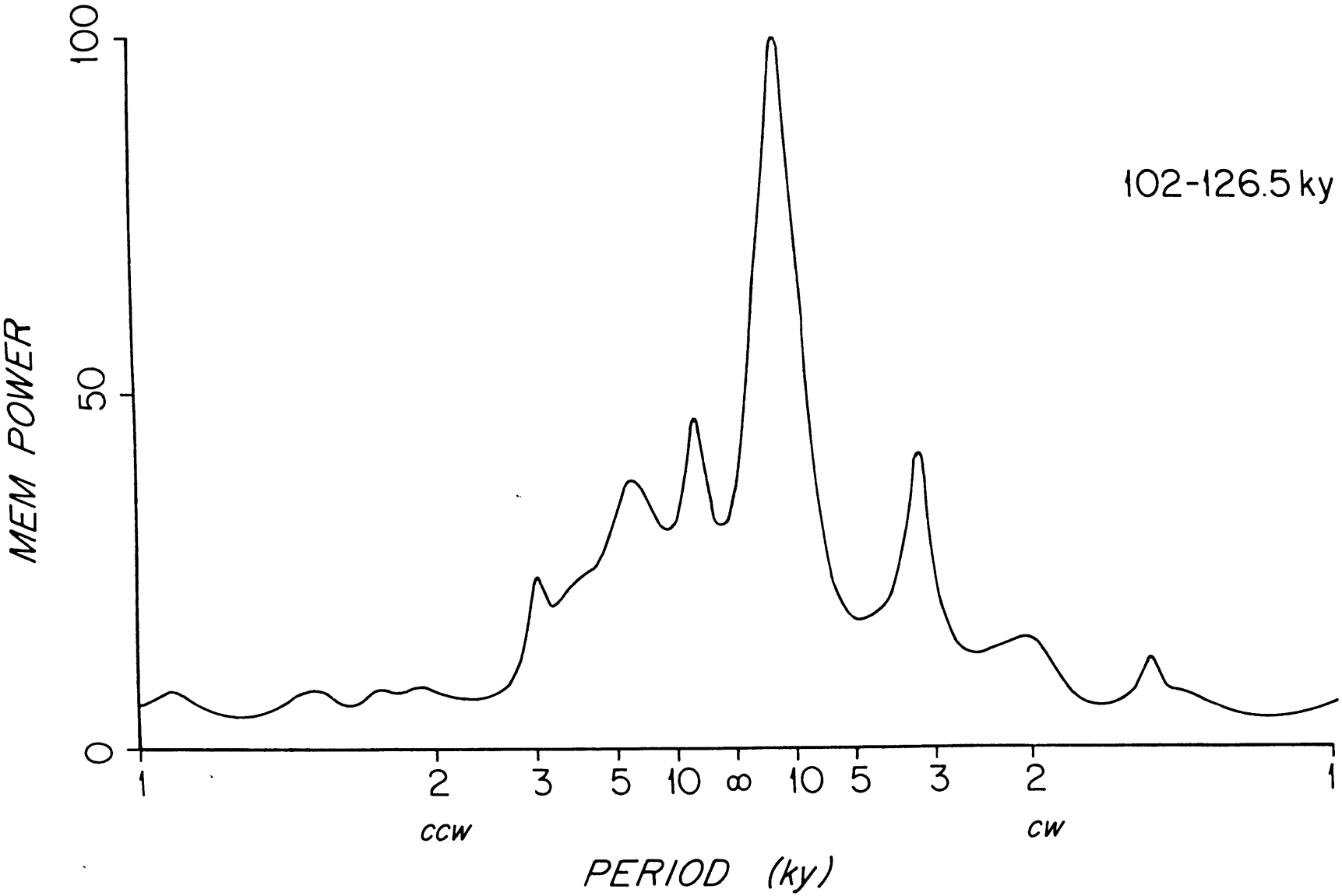
MEM POWER
100
50
0
102-126.5 ky
1
2
3
5
10
∞
10
5
3
2
1
ccw
cw
PERIOD (ky)

The faunal analysis of section 3 indicates that inter-core correlation is degraded in the interval 77-102 kybp. Rapid climatic fluctuations occured from 80-110 kybp which could have been accompanied by small scale changes in accumulation of sediment that are not detectable by our stratigraphic technique. The existence of localised sedimentation patterns derives support from the appearance of the data in Figures 3 and 5. Marked faunal changes that do not correlate well between cores are evident. Core 26 contains large quantities of the diatom Thalassionema nitszchioides throughout the 100-127 kybp interval, but this was not observed in other cores. These depositional effects could influence the magnetic record either by removing short sections or by stretching and shrinking the time scale.

The process of remanence acquisition in sediments is not well understood. Marine deposits are heavily bioturbated and do not show an inclination error, suggesting that the magnetization is of post-depositional origin (Opdyke and Henry, 1969; Verosub, 1977). Since the depth extent and degree of mixing by biological activity is undoubtedly climatically controlled, the rapid climatic oscillations in the interval 80-110 kybp could have led to marked variation in the detrital remanent magnetization process.

The signal-to-noise ratio (SNR) for the directional data can be estimated by examining the prediction error in the AR fitting procedure. The normalized error power is typically 0.3-0.5, suggesting an SNR of less than 1:1 to 2:1 in each core. This conclusion is supported by the data in Table 4: if the large spectral peaks contain the only signal the computed SNR is also 1:1 to 2:1. This exemplifies another reason for redundant paleomagnetic measurements as a means of improving the SNR.

The pNRM/pARM data show a large and long term (30 ky) change. We have not emphasized the spectral properties of this data because it is not clear that the variation is not of climatic origin. Cross spectra of the paleointensity data with climatic parameters are needed to determine this relationship, and such work is beyond the scope of this paper.

The most important result obtained.in this study is the time scale of geomagnetic behavior. The directional data display periodicities near

$10^4$ years period and changes in the nature of the periodicities requires a longer time of 20 ky. Most secular variation work in lakes suggests much shorter time scales near $10^3$ years (Creer, 1977), but the short available record in lakes precludes resolution of longer term behavior. If the $10^3$ year changes were present, they have either been destroyed by post-depositional processes or are dwarfed by longer period power.

## 7. CONCLUSIONS

From this study of the stratigraphy and geomagnetic secular variation record in marine sediments from the North Atlantic we conclude:

1. Only five in a suite of thirteen piston cores from a 1500 $km^2$ area contained the Holocene section, suggesting extensive erosion by bottom currents.
2. Sediment lithology, mineralogy, and accumulation rate is controlled by climate. A glacial/interglacial contrast in sedimentation rate was detected by a correlation procedure. The sedimentation rate is 4 cm/ky during glacial times, increasing to 7-9 cm/ky during interglacials.
3. Forty-six pilot samples were selected from four cores for detailed analysis of demagnetization behavior. The magnetic stability of the sediments is high, with a median demagnetizing field of 315 44 oe and directional changes of less than $5^o$ over a 300 oe range. ARM reproduces the coercive force spectrum of the NRM. The relative paleointensity, calculated using the pNRM/pARM method, is independent of the partial demagnetizing fields used over a 150-400 oe range.
4. Paleomagnetic time series of directions and relative paleointensities were obtained over an age range of 25-127 kybp. The directions correlate well only in the interval prior to 77 kybp. The paleointensity data are smooth and dominated by a long period signal.
5. The paleomagnetic directions display periodic looping of the field directions with a principal period near 10 ky. Behavior of the paleofield is complex with no dominant looping direction. Adjacent 20 ky long sections of data are not spectrally similar. The inter-core variation of the directional spectra in the interval 77-127 kybp is large, suggesting either post-depositional effects or sediment accumulation changes that are not detectable.

APPENDIX: QUANTITATIVE ASSESSMENT OF STRATIGRAPHIC CORRELATION

A single stratigraphic variable, such as the polar assemblage in this study, measured at a number of closely spaced sites is modeled as a common signal with additive noise in each core. Changing the number and location of the age picks alters the signal level, which is to be maximized. By expanding the data in empirical orthogonal functions (EOF) it is possible to find both the best regional stratigraphic curve and the fraction of data variance which it predicts. The use of EOF's results in the most efficient method of compressing multiple measurements of a variable and separates the data into uncorrelated orthogonal modes. The common signal which is sought is the first or signal EOF Expansion in EOF's is equivalent to performing a principal components analysis.

A data matrix A is constructed whose columns are measurements of the stratigraphic variable down-core and whose rows are the different variables at a single age. To simplify the calculation the data are interpolated to even intervals using a natural cubic spline after choosing the time horizons. The variance of each column of A is set to one to avoid weighting any one measurement excessively. The eigenvalues and eigenvectors of the covariance matrix $AA^T$ are obtained using standard techniques. The EOF's are the five unique eigenvectors of $AA^T$ weighted by the square root of the corresponding eigenvalue and arranged in order of decreasing size. The eigenvalues are proportional to the fraction of data variance explained by the corresponding EOF.

Two methods of assessing the significance of the correlation are possible. A qualitative approach requires the first EOF to appear similar to the original data with the remaining noise variance widely distributed in age. A high frequency form for the residual is indicative of low residual variance. Since the eigenvalues of the covariance matrix matrix reflect the variance in the signal and noise EOF's, a quantitative approach can also be used. The signal variance for different choices of time horizons can be compared and a significance level attached to the variance ratio using a two-tailed F-test (Sokal and Rohlf, 1969).

REFERENCES

Akaike, H., 1969. Fitting autoregressive models for prediction, Ann. Inst. Stat. Math. 21, 243-247.

Akaike, H., 1974. A new look at the statistical model identification, IEEE Trans. AC-19, 716-723.

Alldredge, L.R., 1976. Effects of solar activity on annual means of geomagnetic components, J. geophys. Res. 81, 2990-2996.

Broecker, W.S. and J. Van Donk, 1970. Insolation changes, ice volumes, and the O-18 record in deep-sea cores, Rev. Geophys. 8, 169-198.

Burg, J.P., 1975. Maximum entropy spectral analysis, Ph. D. dissertation, Stanford Univ., 123 pp.

Busse, F., 1975. A model of the geodynamo, Geophys. J. Roy. astr. Soc. 42, 437-459.

Chave, A.D. and C.R. Denham, 1979. Climatic changes, magnetic intensity variations and fluctuations of the earth's orbit during the past 2,000,000 years and a mechanism which may be responsible for the relationship--a discussion, E. Pl. Sci. Lett. 44, 150-152.

Cline, R.M. and J.D. Hays (ed.), 1976. Investigation of late Quaternary paleoceanography and paleoclimatology, Geol. Soc. Am. Mem. 145, 464 pp.

Cox, A., 1975. The frequency of geomagnetic reversals and the symmetry of the nondipole field, Rev. Geophys. 13, 35-51.

Creer, K., 1977. Geomagnetic secular variation during the last 25000 years: an interpretation of data obtained from rapidly deposited sediments, Geophys. J. Roy. astr. Soc. 48, 91-109.

Denham, C.R., 1974. Counter-clockwise motion of the paleomagnetic directions 24000 years ago at Mono Lake, California, J. Geomag. Geoelec. 26, 487-498.

Denham, C.R., 1975. Spectral analysis of paleomagnetic time series, J. geophys. Res. 80, 1897-1901.

Denham, C.R. and A. Cox, 1971. Evidence that the Laschamp polarity event did not occur 13300-30400 years ago, E. Pl. Sci. Lett. 13, 181-190.

Dodson, R.E., 1979. Counterclockwise precession of the geomagnetic field vector and westward drift of the nondipole field, J. geophys. Res. 84, 637-644.

Goree, W.S. and M. Fuller, 1976. Magnetometers using RF-driven squids and their applications in rock magnetism and paleomagnetism, Rev. Geophys. 14, 591-608.

Harmon, R.L., H.D. Schwarz, and D.C. Ford, 1978. Late Pleistocene sea level history of Bermuda, Quat. Res. 9, 205-218.

Haykin, S. (ed.), 1979. Nonlinear Methods of Spectral Analysis, New York: Springer-Verlag, 247 pp.

James, R.W., 1970. Decomposition of geomagnetic secular variation into drifting and nondrifting components, J. Geomag. Geoelec. 22, 241-252.

James, N.P., E.W. Mountjoy, and A. Omura, 1971. An early Wisconsin reef terrace at Barbados, West Indies, and its climatic implications, Geol. Soc. Am. Bull. 82, 2011-2018.

Johnson, G.L. and E.D Schneider, 1969. Depositional ridges in the North Atlantic, E. Pl. Sci. Lett. 6, 416-422.

Johnson, H.P., H. Kinoshita, and R. Merrill, 1975. Rock,magnetism and paleomagnetism of some North Pacific deep sea sediments, Geol. Soc. Am. Bull. 86, 412-420.

Kennett, J.P., 1968. Latitudinal variation in Globigerina pachyderma (Ehrenberg) in surface sediments of the southwest Pacific Ocean, Micropaleontology 14, 305-318.

Ku, T.C. and W.S. Broecker, 1966. Atlantic deep-sea stratigraphy: extension of absolute chronology to 320,000 years, Science 151, 448.

Lacoss, R., 1971. Data adaptive spectral analysis methods, Geophysics 36, 661-673.

Levi, S. and S.K. Banerjee, 1976. On the possibility of obtaining relative paleointensities from lake sediments, E. Pl. Sci. Lett. 29, 219-226.

Liddicoat, J. and R.S. Coe, 1979. Mono Lake geomagnetic excursion, J. geophys. Res. 84, 261-271.

McIntyre, A., W.F. Ruddiman, and R. Jantzen, 1972. Southward penetrations of the North Atlantic polar front: faunal and floral evidence of large scale surface water mass movements over the last 225,000 years, Deep Sea Res. 19, 61-77.

Mesolella, K.J., R.K. Matthews, W.S. Broecker, and D.C. Thurber, 1969. The astronomical theory of climatic change: Barbados data, J. Geol. 77, 250-274.

Opdyke, N.D.,and K.W. Henry, 1969. A test of the dipole hypothesis, E. Pl. Sci. Lett. 6, 138-151.

Opdyke, N.D., D. Ninkovich, W. Lowrie, and J.D. Hays, 1972. The paleomagnetism of two Aegean deep sea cores, E. Pl. Sci. Lett. 14, 145-159.

Parker, F.L., 1962. Planktonic foraminiferal species in Pacific sediments, Micropaleontology 8, 219-254.

Parker, R.L. and C.R.Denham, 1979. Interpolation of unit vectors, Geophys. J. Roy. astr. Soc. 58, 685-687.

Parzen, E., 1974. Some recent advances in time series modeling, IEEE Trans. AC-19, 723-730.

Ruddiman, W.F., 1972. Sediment redistribution on the Reykjanes Ridge: seismic evidence, Geol. Soc. Am. Bull. 83, 2039-2062.

Ruddiman, W.F. and L.K. Glover, 1972. Vertical mixing of ice-rafted ash in North Atlantic sediments, Geol. Soc. Am. Bull. 83, 2817-2836.

Ruddiman, W.F. and A. McIntyre, 1973. Time-transgressive deglacial retreat of polar water from the North Atlantic, Quat. Res. 3, 117-130.

Ruddiman, W.F. and A. McIntyre, 1976. Northeast Atlantic paleoclimatic changes over the past 600,000 years, in R.M. Cline and J.D. Hays (ed.), Geol. Soc. Am. Mem. 145, pp 111-146.

Ruddiman, W.F. and A. McIntyre, 1979. Warmth of the subpolar North A Atlantic Ocean during northern hemisphere ice-sheet growth, Science 204, 173-175.

Ruddiman, W.F., C.D. Sancetta, and A. McIntyre, 1977. Glacial/interglacial response rate of subpolar North Atlantic waters to climatic change: the record in oceanic sediments, Phil. Trans. R. Soc. Lon. B280, 119-142.

Seyb, S.M., S.R. Hammond, and T. Gilliard, 1977. A new device for recording the behavior of a piston corer, Deep Sea Res. 24, 943-950.

Shackleton, N.J. and R.K. Matthews, 1977. Oxygen isotope stratigraphy of late Pleistocene coral reef terraces in Barbados, Nature 268, 618-619.

Skiles,D.D., 1970. A method of inferring the direction of drift of the geomagnetic field from paleomagnetic data, J. Geomag. Geoelec. 22, 441-462.

Sokal, R.R. and F.J Rohlf, 1969. Biometry, San Francisco: Freeman, 776 pp.

Steele, J.H., J.R. Barrett, and L.V. Worthington, 1962. Deep currents south of Iceland, Deep Sea Res. 9, 465-474.

Thierstein, H.R., K.R. Geitzenauer, B. Molfino, and N.J. Shackleton, 1977. Global synchroneity of late Quaternary coccolith datum levels: validation by oxygen isotopes, Geology 5, 400-404.

Thompson, R., 1975. Long period European geomagnetic secular variation confirmed, Geophys. J. Roy. Soc. 43, 847-859.

Ulrych, T.J., and T.N. Bishop, 1975. Maximum entropy spectral analysis and autoregressive decomposition, Rev. Geophys. 13, 183-200.

Van den Bos, A., 1971. Alternative interpretation of maximum entropy spectral analysis, IEEE Trans. IT-17, 493-494.

Verosub, K., 1977. Depositional and postdepositional processes in the magnetization of sediments, Rev. Geophys. 15, 129-143.

Wollin, G., W.B.F. Ryan, and D.B. Ericson, 1978. Climatic changes, magnetic intensity variations and fluctuations of the eccentricity of the earth's orbit during the past 2,000,000 years and a mechanism which may be responsible for the relationship, E. Pl. Sci. Lett. 41, 395-397.